Charles University in Prague
Faculty of Mathematics and Physics

Earthquake of Athens, 1999: Study of Aftershocks

Master Thesis

Otakar Smrž

Advisor: Doc. RNDr. Jiří Zahradník, DrSc.

Department of Geophysics
Prague, 2001

I hereby declare that I have elaborated this master thesis on my own and that the references include all sources of information I have exploited. I agree with lending of this master thesis.

Prague, April 20, 2001 Otakar Smrž

Contents

General Introduction

On September 7, 1999 at 11:56:50 GMT a disastrous earthquake of $M_w = 5.9$ struck Athens, the capital of Greece. The mainshock was followed by a series of aftershocks, the study of which shall be the topic of this work.

Seismic data and their source

We process data available to us from temporary 31-station network deployed by the Seismological Laboratory of the University of Patras not long after the mainshock.

Along with velocigrams of some of the aftershocks, we obtained detailed lists of onset readings (time, polarity). Station identification parameters and local tectonic model were provided as well. HYPO location results (including magnitude etc.) facilitated data organization and enabled mutual comparison later on.

Motivation and aims of the work

We started our studies of the earthquake of Athens in October 1999. There was an urgent need to find out more about spatial setting of the aftershocks, hoping that there might be some interesting connection to local geological structure. In addition, aftershock distribution could assure us of the right orientation of the focal mechanism of the mainshock, or rather appoint the fault plane.

Such a research does not require seismic waveform data, which was more than fortunate then (we must be aware of delays in data availability in real life). Onset readings and station co-ordinates provide enough information. Fixed model parameters are also necessary so that we calculate seismic rays,

but, as the problem is over-determined, model properties can be varied and grid-searched in our computations.

In the first part of the thesis, our tasks are following:

1. With respect to the grid search method, design the most convenient interest area and propose local seismic model.

2. Determine the best velocity parameters of the model. Locate the aftershocks along with finding time corrections for individual stations.

3. Try to identify aftershock hypocentres with a hypothetic fault plane.

Thorough testing of the ASPO method is carried out in the second part of the study. The amount of available waveform data is extraordinary—focal mechanism inversions using more than five stations, say, have not been performed by ASPO until now. We suggest improvement to some computational formulae and effects upon the behaviour of the method are discussed.

Mathematical notation

Within this work, we introduce a special notation. We distinguish several types of sets of indices, trying to make computational implementation evident. Symbols of sets are rendered in calligraphic uppercase, whereas set elements use italic lowercase and occur in superscripts of relevant quantities.

For we deal with many categories of indices to address array variables in our programs, we introduce these main set types

$\mathcal{E}$	...	events, i.e. somehow distinguished aftershocks
$\mathcal{S}$	...	stations involved in the problem
$\mathcal{P}$	...	waveform phases
$\mathcal{C}$	...	components of the seismic record
$\mathcal{F}$	...	discrete frequency values for ASPO inversion

and simplify the hyper-correct notation

$$\sum_{i \in \mathcal{I}} \mathrm{e}\,(x_a^i, \ldots, x_z^i) \equiv \sum_{\mathcal{I}} \mathrm{e}\,(x_a^i, \ldots, x_z^i).$$

It is to stress that not always are the referenced values x_j^i defined. Then, of course, the whole expression $\mathrm{e}\,(x_a^i, \ldots, x_z^i)$ is skipped in the summation. In

some cases, providing a new function

$$\mathrm{def}\,(x_j^i) = \begin{cases} 1 & \text{if the argument is defined} \\ 0 & \text{otherwise} \end{cases}$$

shows useful.

To give a succinct example of our notation conventions,

$$n_{onset}^{e} = \sum_{\mathcal{S}} \sum_{\mathcal{P}} \mathrm{def}\,(t_{obs}^{e,\,s,\,p})$$

means that n_{onset}^{e} is a number of onset readings $t_{obs}^{e,\,s,\,p}$ of a given event e, considering each existing phase $p \in \mathcal{P}$ of the waveform recorded at station $s \in \mathcal{S}$.

Part I

Location of Aftershocks and Fault Plane Search

Chapter 1

Term Definitions and Grid Search Method

1.1 Derivation of time corrections

From now on, we will handle these time variables:

t_{obs}	...	observed arrival time
t_{syn}	...	synthetic arrival time
t_{prop}	...	propagation time
t_{orig}	...	origin time of the event
t_{corr}	...	station time correction

As mentioned above, we only have notion of t_{obs} and t_{prop}, while t_{syn} and the other two quantities have to be derived now.

Synthetic arrival time consists by definition of two components,

$$t_{syn}^{e,s,p} = t_{prop}^{e,s,p} + t_{orig}^{e}. \tag{1.1}$$

Origin time of a given event is simply an average over stations of individually presumed origin times

$$t_{orig}^{e} = \frac{1}{n_{onset}^{e}} \sum_{\mathcal{S}} \sum_{\mathcal{P}} \left(t_{obs}^{e,s,p} - t_{prop}^{e,s,p}\right) \tag{1.2}$$

$$n_{onset}^{e} = \sum_{\mathcal{S}} \sum_{\mathcal{P}} \mathrm{def}\left(t_{obs}^{e,s,p}\right),$$

where n_{onset}^{e} is the total number of onsets of the considered event.

Knowledge of t_{obs} and t_{syn} is sufficient for solving seismic location. Once we fix all events in the right positions, time corrections can be calculated for every particular station and phase. The formulae read

$$t_{corr}^{s,p} = \frac{1}{n_{onset}^{s,p}} \sum_{\mathcal{E}} (t_{obs}^{e,s,p} - (t_{prop}^{e,s,p} + t_{orig}^{e})) \tag{1.3}$$

$$n_{onset}^{s,p} = \sum_{\mathcal{E}} \mathrm{def}\,(t_{obs}^{e,s,p}),$$

$n_{onset}^{s,p}$ meaning the number of onsets of the given phase recorded by the station concerned.

Time corrections could be used for iterative relocation, supposing we modified (1.1, 1.2 and 1.4). However, this is not our intention. We are interested in time corrections in order to judge stations' reliability as regards focal mechanism retrieval since large corrections might indicate spectra distortion due to site-effects.

1.2 Grid search method

The principle of the method is as follows. We represent the definition range of a function by a discrete grid of points. Values of the function are then calculated for all of them and handled according to the problem.

Our location algorithm is based on minimizing the sum of squares of residuals

$$R = \sum_{\mathcal{E}} \sum_{\mathcal{S}} \sum_{\mathcal{P}} (t_{obs}^{e,s,p} - t_{syn}^{e,s,p})^2 = \sum_{\mathcal{E}} \sum_{\mathcal{S}} \sum_{\mathcal{P}} (t_{obs}^{e,s,p} - (t_{prop}^{e,s,p} + t_{orig}^{e}))^2. \tag{1.4}$$

The resultant value can also quantify the "adequateness" of model velocities. We expect that velocities closer to reality will yield lower minima of the error function R. The original grid search location implementation is therefore nested in loops over velocity parameters and the global minimum of the output values solves both location and model inversion.

Chapter 2

Aftershock Processing

2.1 Data sets usage

It is to explain that we use two major data sets. First, we processed 36 events (see column I1 in Tabs. 2.1, 2.2, 2.3) put at our disposal at that time. Locations and best velocity parameters were found based on the grid search method. These data showed suitable for fault plane determination, too.

Later, we received an extended set of 183 events (see column I2 in Tabs. 2.1, 2.2, 2.3). Repeating our calculations did not yield any clear results as to the fault plane, however model velocities and time corrections, being derived from a larger statistical sample, overrode the former ones.

2.2 Interest area and model

The interest area is a rectangular sector of space in which all resultant hypocentres are enclosed. Such a sector is covered with a discrete grid to enable grid search of the location problem. If an event locates on the very border of the interest area, we must extend it of course. The grid step equals 250 m in all directions as a compromise between refinement and computational time.

The stations (Tab. 2.4) are not confined within the interest area though, except that in computations they share the same Cartesian system rotated 30° eastward, as apparent from the orientation of the interest area in Figs. 2.3, 2.4. Nevertheless, we shall keep to geographical co-ordinates herein to avoid entering into technical details.

I1	I2	Date	Origin Time
	1	99/09/13	15:00:51.11
	2	99/09/13	15:07:30.38
	3	99/09/13	16:46:38.56
	4	99/09/13	19:30:28.44
	5	99/09/14	01:18:04.08
	6	99/09/14	01:20:19.47
	7	99/09/14	02:35:38.24
	8	99/09/14	18:47:16.13
	9	99/09/14	19:36:35.07
	10	99/09/14	19:39:27.99
	11	99/09/14	21:41:00.85
1	12	99/09/14	21:41:54.60
2	13	99/09/14	21:47:57.74
3	14	99/09/14	22:12:23.85
	15	99/09/14	23:42:26.49
	16	99/09/14	23:51:24.41
	17	99/09/15	00:40:29.46
	18	99/09/15	02:50:12.08
	19	99/09/15	03:06:42.45
	20	99/09/15	04:21:49.16
	21	99/09/15	12:12:14.42
	22	99/09/15	12:14:36.64
	23	99/09/15	13:26:55.31
	24	99/09/15	15:20:15.37
	25	99/09/15	16:12:23.14
4	26	99/09/15	18:06:35.95
5	27	99/09/15	21:31:29.43
6	28	99/09/15	22:16:57.19
7	29	99/09/15	23:32:21.73
	30	99/09/15	23:35:02.12
8	31	99/09/15	23:54:30.56

I1	I2	Date	Origin Time
9	32	99/09/15	23:56:32.13
	33	99/09/16	00:30:04.99
	34	99/09/16	01:54:45.27
10	35	99/09/16	03:31:50.12
11	36	99/09/16	03:48:00.32
	37	99/09/16	05:37:12.93
	38	99/09/16	08:12:09.70
	39	99/09/16	09:15:52.94
12	40	99/09/16	11:44:42.26
	41	99/09/16	12:22:21.76
	42	99/09/16	12:57:05.38
	43	99/09/16	13:17:07.82
13	44	99/09/16	17:00:36.88
	45	99/09/16	19:02:01.09
	46	99/09/16	19:27:22.68
	47	99/09/16	21:35:41.54
14	48	99/09/16	21:46:18.19
15	49	99/09/16	22:51:47.18
	50	99/09/16	22:57:16.20
	51	99/09/16	23:02:37.16
	52	99/09/17	00:00:34.86
	53	99/09/17	00:50:58.75
16	54	99/09/17	01:02:47.08
	55	99/09/17	01:11:37.18
17	56	99/09/17	01:27:45.00
18	57	99/09/17	01:30:08.00
	58	99/09/17	02:00:33.26
19	59	99/09/17	03:41:13.99
	60	99/09/17	04:07:57.57
	61	99/09/17	06:01:48.49
	62	99/09/17	09:47:12.74

Table 2.1: List of processed events, part 1.

I1	I2	Date	Origin Time
20	63	99/09/17	12:56:29.13
	64	99/09/17	14:37:34.26
21		99/09/17	15:08:29.83
22	65	99/09/17	16:37:08.91
23	66	99/09/17	17:37:59.77
24	67	99/09/17	17:42:12.35
25	68	99/09/17	18:10:17.99
	69	99/09/17	18:56:15.56
	70	99/09/17	20:16:19.66
	71	99/09/17	21:05:37.70
	72	99/09/17	21:10:38.36
	73	99/09/17	21:45:52.64
	74	99/09/17	23:40:17.77
	75	99/09/18	01:14:01.37
26	76	99/09/18	02:07:10.42
	77	99/09/18	02:41:17.83
	78	99/09/18	03:10:07.44
27	79	99/09/18	04:37:54.61
	80	99/09/18	04:46:25.75
28	81	99/09/18	05:24:43.37
29	82	99/09/18	06:09:59.71
	83	99/09/18	07:23:56.39
30	84	99/09/18	08:06:00.96
	85	99/09/18	08:21:34.99
	86	99/09/18	09:32:11.24
	87	99/09/18	12:30:54.74
	88	99/09/19	04:15:54.24
	89	99/09/19	04:52:13.08
	90	99/09/19	05:27:25.34
	91	99/09/19	10:50:45.65
	92	99/09/19	13:13:27.88

I1	I2	Date	Origin Time
	93	99/09/19	20:44:19.69
31	94	99/09/20	01:57:26.68
32	95	99/09/20	10:45:59.03
	96	99/09/20	11:01:54.90
	97	99/09/20	12:17:14.24
	98	99/09/20	20:06:59.87
	99	99/09/20	23:12:07.17
	100	99/09/20	23:23:04.22
	101	99/09/21	08:51:35.09
	102	99/09/21	15:17:26.47
	103	99/09/21	17:20:45.74
	104	99/09/21	17:36:31.53
	105	99/09/21	19:21:29.19
	106	99/09/21	19:56:01.01
	107	99/09/21	21:05:44.81
	108	99/09/21	22:01:35.45
	109	99/09/22	01:20:37.07
	110	99/09/22	02:22:15.19
	111	99/09/23	00:42:25.30
	112	99/09/23	02:11:27.95
	113	99/09/23	16:54:02.01
	114	99/09/23	17:25:49.88
	115	99/09/23	18:06:34.14
33	116	99/09/24	00:56:34.16
	117	99/09/24	02:17:22.58
	118	99/09/24	02:41:49.29
	119	99/09/24	02:53:20.46
	120	99/09/24	04:30:46.79
	121	99/09/24	04:57:18.19
	122	99/09/24	05:27:02.25
	123	99/09/24	08:47:27.03

Table 2.2: List of processed events, part 2.

I1	I2	Date	Origin Time
	124	99/09/24	09:57:53.14
	125	99/09/24	10:16:54.82
	126	99/09/24	10:50:29.55
	127	99/09/24	11:55:50.88
	128	99/09/24	13:07:29.36
	129	99/09/24	17:46:41.81
	130	99/09/24	19:43:52.01
	131	99/09/24	20:21:44.35
	132	99/09/24	21:01:26.11
	133	99/09/24	21:27:32.22
34	134	99/09/24	21:43:04.61
	135	99/09/24	23:30:29.48
	136	99/09/24	23:46:13.33
	137	99/09/25	04:10:25.71
35	138	99/09/25	06:37:50.72
36	139	99/09/25	08:47:25.61
	140	99/09/26	00:01:35.61
	141	99/09/26	00:33:24.39
	142	99/09/26	01:20:08.81
	143	99/09/26	07:33:12.27
	144	99/09/26	08:24:52.05
	145	99/09/26	08:33:38.37
	146	99/09/26	09:13:59.52
	147	99/09/26	09:42:28.89
	148	99/09/26	16:50:53.31
	149	99/09/26	18:40:27.36
	150	99/09/26	20:04:36.79
	151	99/09/26	21:24:22.48
	152	99/09/26	22:55:13.72
	153	99/09/26	23:10:24.80

I1	I2	Date	Origin Time
	154	99/09/27	00:00:41.62
	155	99/09/27	02:25:22.69
	156	99/09/27	06:22:30.61
	157	99/09/27	11:40:34.17
	158	99/09/27	21:32:53.26
	159	99/09/28	07:33:42.41
	160	99/09/28	07:41:55.93
	161	99/09/28	23:54:45.92
	162	99/09/29	00:02:02.21
	163	99/09/29	00:04:48.75
	164	99/09/30	04:52:09.53
	165	99/09/30	11:55:13.04
	166	99/09/30	20:30:39.30
	167	99/10/01	00:22:37.84
	168	99/10/01	03:11:15.94
	169	99/10/01	11:21:30.65
	170	99/10/01	15:10:46.60
	171	99/10/02	01:00:39.63
	172	99/10/02	01:00:39.26
	173	99/10/02	04:33:32.77
	174	99/10/02	21:14:30.54
	175	99/10/02	23:40:45.93
	176	99/10/03	01:02:20.50
	177	99/10/03	01:03:07.94
	178	99/10/03	02:03:59.26
	179	99/10/03	03:13:40.25
	180	99/10/03	03:15:30.24
	181	99/10/03	12:51:32.15
	182	99/10/03	23:41:49.01
	183	99/10/03	23:47:26.96

Table 2.3: List of processed events, part 3.

Our model is a homogenous isotropic half-space for which v_p and v_p/v_s are varied. Precise location is not the point—we rather need self-consistent and well-resolved location in all three directions to try to find the fault plane.

2.3 Fault plane determination

Remarkable results were obtained for the 36-event set. Having located the aftershocks, we were interested in their spatial distribution.

We assigned one common fault plane to all hypocentres, but planar regression was too vague. We therefore watched their projections onto the vertical plane, namely XZ, for different azimuths of the reference system. The alignment improved toward the azimuth of 117° of view, where the hypocentres lined up best forming three parallel groups.

The situation is depicted in Fig. 2.1. Events 1, 2, 3, 4, 25, 31, 33 above the fault plane are rendered as violet diamonds, events 15, 23, 36 below the plane are the red squares. Division of the events was necessary, otherwise linear regression did not fit the trend. Dip of the fault plane represented by the blue straight line is 52°.

Intersection of the fault plane with the Earth's surface was identified as Fili Fault by the authors of [4, 5] and the results $\phi = 117°$, $\delta = 52°$ agreed with the mechanism of the mainshock from teleseismic data.

2.4 Best velocity parameters

The above location was carried out using $v_p = 5.75$ km/s and $v_p/v_s = 1.800$, the best parameters found for the 36-event set.

The 183-event set yields the optimal parameters $v_p = 5.80$ km/s and $v_p/v_s = 1.800$. We must stress that all these numbers correspond to the minimum of a very shallow valley in the error function R and therefore the difference between both sets is tolerable. In Fig. 2.2, we plot the error function for the 183-event set. The grid is defined by the tics on axes.

2.5 Time corrections

We present results only for the 183-event set (Tab. 2.5, Figs. 2.3, 2.4). For five stations, no onset readings were available. The original idea was to rec-

Id	Code	North Latitude		East Longitude		Altitude
1	GEO	37° 58.92′	37.982°	23° 42.14′	23.702°	60 m
2	NLI	38° 02.29′	38.038°	23° 42.07′	23.701°	36 m
3	PET	38° 02.76′	38.046°	23° 39.95′	23.666°	312 m
4	LIO	38° 04.60′	38.077°	23° 42.53′	23.709°	182 m
5	FIL	38° 06.24′	38.104°	23° 40.18′	23.670°	437 m
6	MKL	38° 07.82′	38.130°	23° 39.39′	23.657°	484 m
7	MAG	38° 04.37′	38.073°	23° 32.00′	23.533°	35 m
8	FLD	38° 02.45′	38.041°	23° 44.01′	23.733°	25 m
9	KRY	38° 08.45′	38.141°	23° 49.70′	23.828°	559 m
10	TAT	38° 09.40′	38.157°	23° 47.79′	23.797°	523 m
11	BAR	38° 08.08′	38.135°	23° 47.45′	23.791°	435 m
12	THR	38° 08.37′	38.139°	23° 45.63′	23.761°	451 m
13	PAR	38° 09.15′	38.153°	23° 44.20′	23.737°	1109 m
14	INF	38° 18.31′	38.305°	23° 38.67′	23.645°	36 m
15	MEL	38° 03.67′	38.061°	23° 50.87′	23.848°	350 m
16	RAF	38° 01.08′	38.018°	23° 59.69′	23.995°	78 m
17	KIF	38° 05.76′	38.096°	23° 47.97′	23.799°	36 m
18	AHA	38° 04.99′	38.083°	23° 45.91′	23.765°	225 m
19	HAL	38° 01.33′	38.022°	23° 47.87′	23.798°	31 m
20	SPT	37° 57.92′	37.965°	23° 54.73′	23.912°	178 m
21	MAR	38° 09.45′	38.157°	23° 57.44′	23.957°	46 m
22	VAR	38° 13.37′	38.223°	23° 54.97′	23.916°	450 m
23	KAL	38° 15.72′	38.262°	23° 52.39′	23.873°	596 m
24	ORP	38° 18.97′	38.316°	23° 47.32′	23.789°	148 m
25	MEN	38° 05.63′	38.094°	23° 43.43′	23.724°	110 m
26	ASP	38° 03.72′	38.062°	23° 35.33′	23.589°	35 m
27	STE	38° 10.46′	38.174°	23° 32.77′	23.546°	631 m
28	SAL	37° 59.05′	37.984°	23° 28.77′	23.480°	71 m
29	HAI	38° 00.77′	38.013°	23° 38.22′	23.637°	200 m
30	FLP	37° 58.19′	37.970°	23° 43.21′	23.720°	140 m
31	VUL	37° 48.42′	37.807°	23° 47.09′	23.785°	29 m

Table 2.4: List of available stations and their co-ordinates.

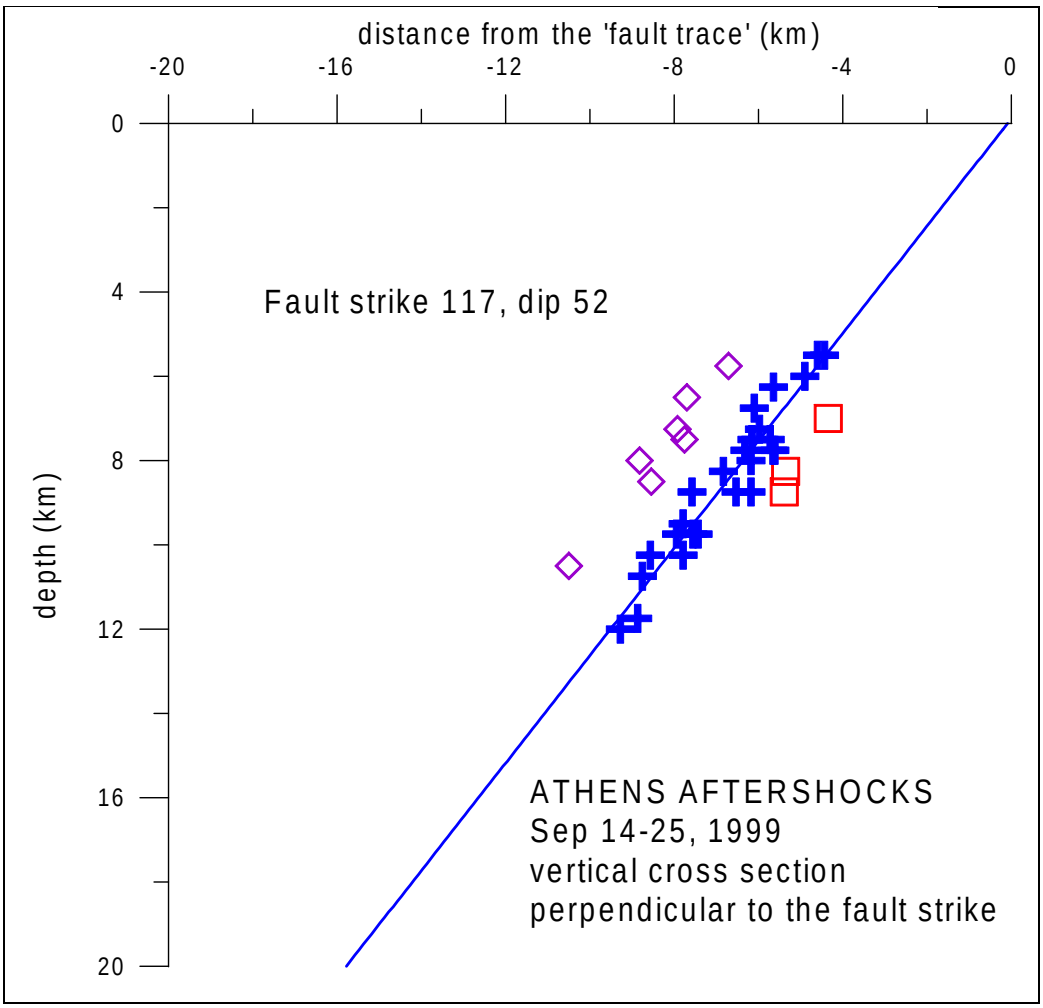

Figure 2.1: Results of the fault plane search for the 36-event set.

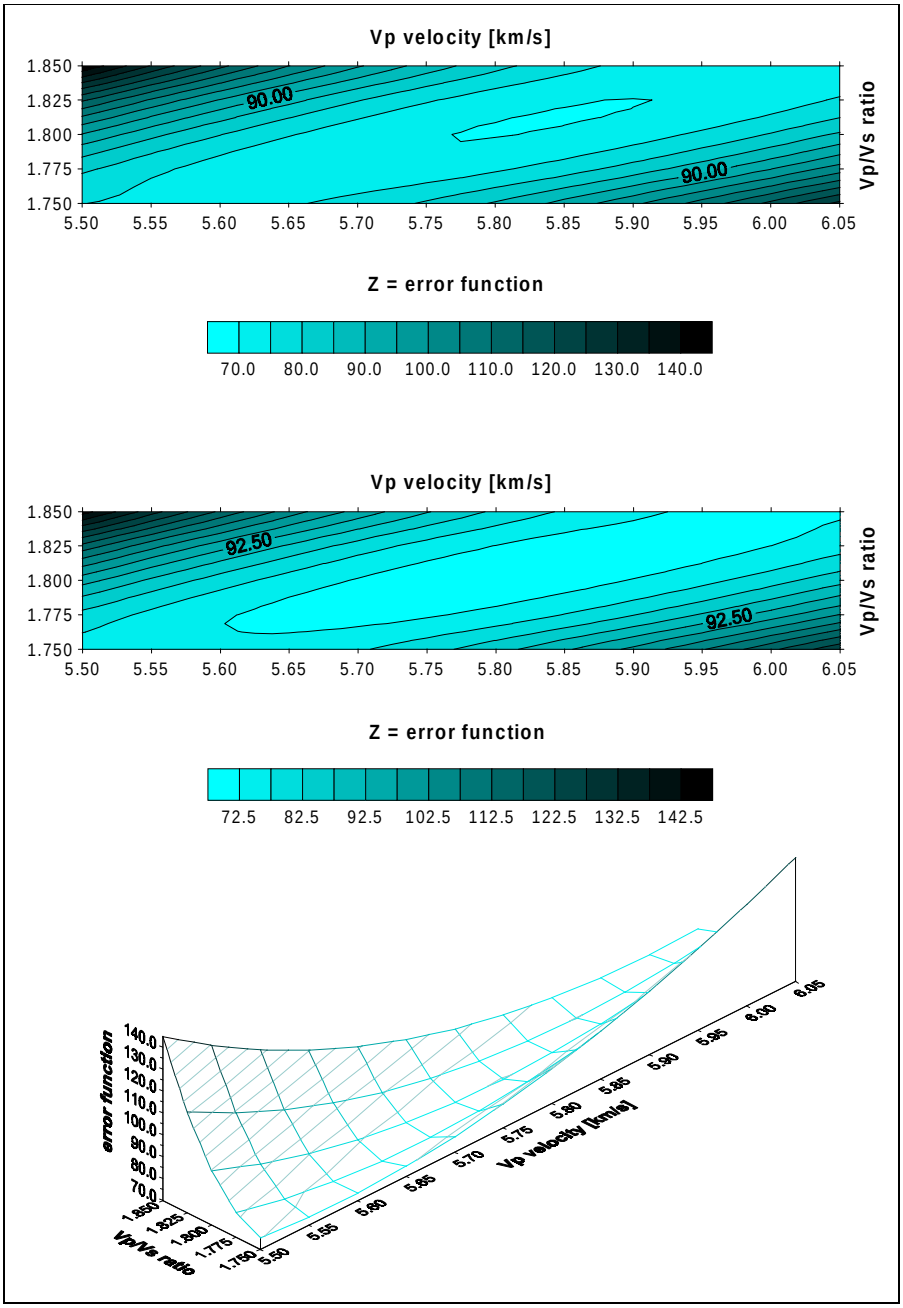

Figure 2.2: Error function R for varying v_p and v_p/v_s using the 183-event set.

Id	Code	t^P_{corr} (s)	t^S_{corr} (s)	Id	Code	t^P_{corr} (s)	t^S_{corr} (s)
2	NLI	0.04	0.11	17	KIF	0.17	0.38
3	PET	-0.05	-0.12	18	AHA	0.08	0.21
4	LIO	0.00	0.01	19	HAL	0.08	0.00
6	MKL	-0.01	-0.05	20	SPT	-0.01	-0.10
7	MAG	-0.03	0.02	21	MAR	0.03	0.14
8	FLD	0.06	0.13	22	VAR	-0.04	-0.07
9	KRY	0.00	0.00	23	KAL	-0.06	-0.09
11	BAR	0.04	0.05	24	ORP	0.11	0.31
12	THR	0.03	0.01	25	MEN	0.02	0.06
13	PAR	-0.16	-0.26	26	ASP	-0.00	0.05
14	INF	0.09	0.22	27	STE	-0.02	0.01
15	MEL	-0.06	-0.14	29	HAI	-0.01	0.05
16	RAF	-0.00	0.03	31	VUL	-0.04	-0.17

Table 2.5: Time corrections in individual stations (there were no onset readings available for the missing stations).

ognize those stations in which time corrections suggest a delay or a boost of the arrival time in order to eliminate them from further focal mechanism inversion (as reasoned on page 8). These tips were not regarded after all, because occurrence of seismic records of good quality did not correlate with them in any sense.

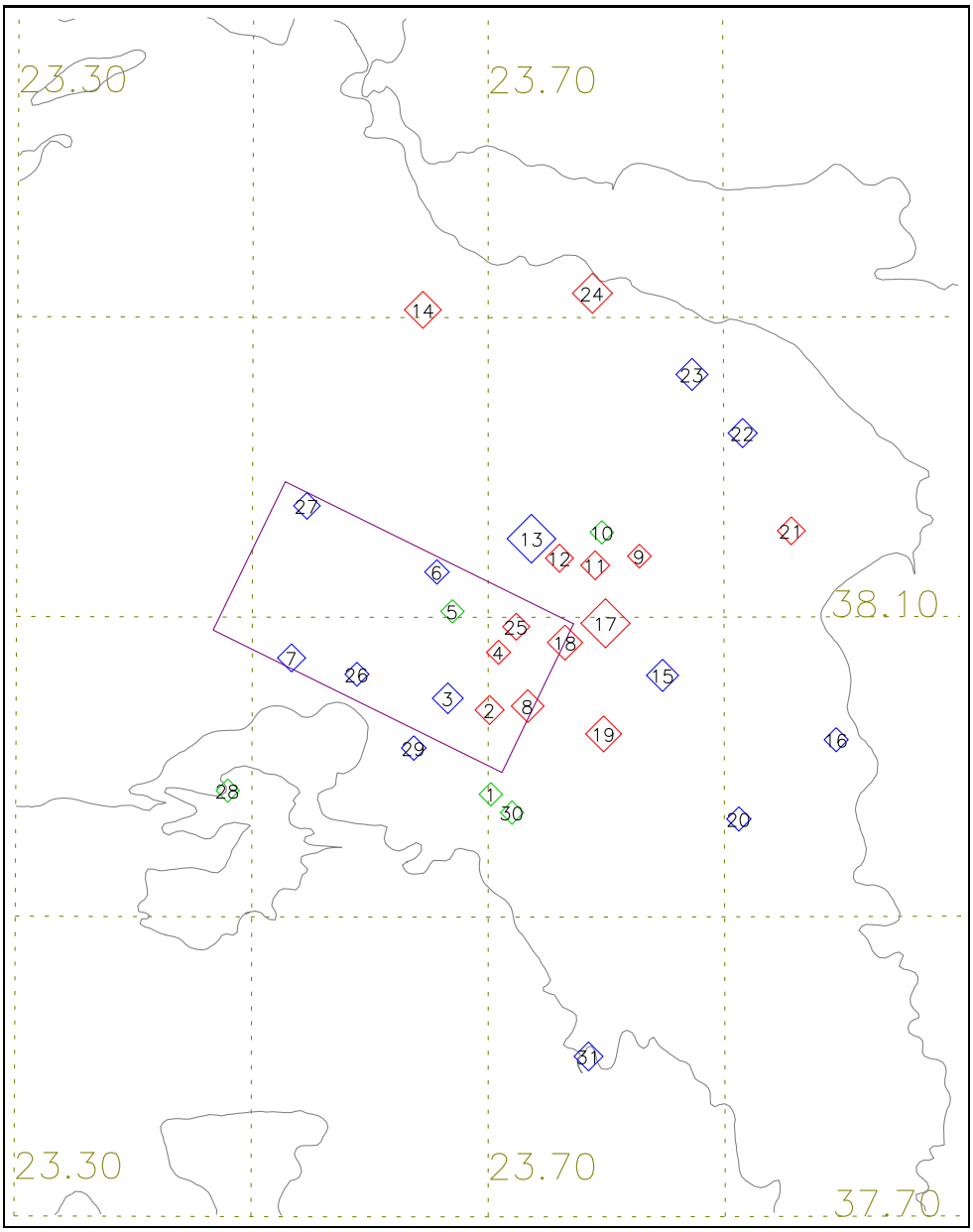

Figure 2.3: Time corrections for P waves in individual stations (red positive, blue negative, green no onset readings). Size of the symbol corresponds to the absolute value, see Tab. 2.5. The interest area (violet) and the coastline (grey) are also rendered.

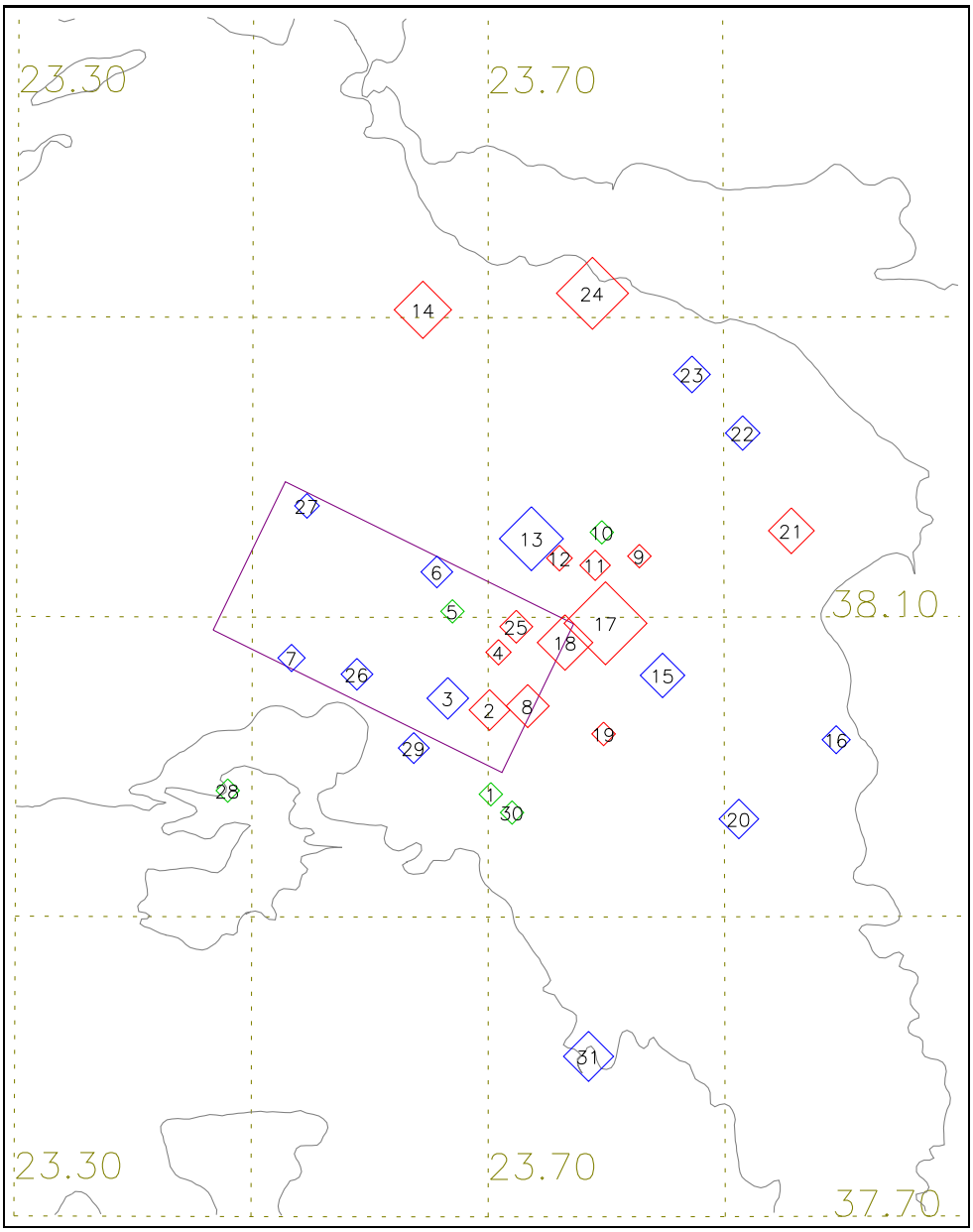

Figure 2.4: Time corrections for S waves in individual stations (red positive, blue negative, green no onset readings). Size of the symbol corresponds to the absolute value, see Tab. 2.5. The interest area (violet) and the coastline (grey) are also rendered.

Part II

Focal Mechanisms Retrieval Using ASPO

Chapter 3

ASPO Method and Its Improvement

For focal mechanism inversions, we used the ASPO method [1, 2, 3], thus pursuing an alternative approach to the problem (see pure polarity solutions in [6, 7, 8]) and validating the method in detail. This has resulted in a change of the computational algorithm, as we show below.

3.1 Former strike, dip, rake retrieval

The name of our method is an acronym of *Amplitude Spectra and POlarities*, which indicates how inversion process is made. Instead of comparing observed waveforms with the synthetic ones to infer the mechanism, similarity of amplitude spectra is taken as the criterion. Not only do we spare computational time (there are not so many Fourier transforms)—we even eliminate the need to fit onset times exactly or to align them artificially, which is in fact much greater advantage. To retrieve strike ϕ, dip δ and rake λ of an event, we use a grid search, whereas seismic moment M_0 is calculated directly based on (3.6, 3.7). Agreement of the first-motion polarities is checked in the final stage.

The method is given observed true ground-motion velocity spectrum $v_{obs}^{s,c,f}$ and generates $v_{syn}^{s,c,f}$, synthetic velocity spectrum computed in the frequency domain as a product of the Green tensor [9, 10, 11] and the unit seismic moment tensor, the latter one dependent on current ϕ, δ, λ of the grid search. These spectra themselves are incomparable because of unequal moments they correspond to and have to be normalized to $\bar{v}_{obs}^{s,c,f}$ and $\bar{v}_{syn}^{s,c,f}$ first, see either

(3.2, 3.3) or (3.4, 3.5) below. Then, an error function

$$E = \frac{1}{n_{scf}} \sum_{\mathcal{S}} \sum_{\mathcal{C}} \sum_{\mathcal{F}} \frac{|\bar{v}_{obs}^{s,c,f} - \bar{v}_{syn}^{s,c,f}|}{\max\left(\bar{v}_{obs}^{s,c,f},\, \bar{v}_{syn}^{s,c,f}\right)} \tag{3.1}$$

$$n_{scf} = \sum_{\mathcal{S}} \sum_{\mathcal{C}} \sum_{\mathcal{F}} \mathrm{def}\left(\bar{v}_{syn}^{s,c,f}\right)$$

is calculated for each moment tensor tested in the grid search.

For the normalization of observed versus synthetic spectrum, we used to apply the formulae

$$\bar{v}_{obs}^{s,c,f} = \frac{v_{obs}^{s,c,f}}{N_{obs}} \qquad \bar{v}_{syn}^{s,c,f} = \frac{v_{syn}^{s,c,f}}{N_{syn}} \tag{3.2}$$

$$N_{obs} = \sum_{\mathcal{S}} \sum_{\mathcal{C}} \sum_{\mathcal{F}} v_{obs}^{s,c,f} \qquad N_{syn} = \sum_{\mathcal{S}} \sum_{\mathcal{C}} \sum_{\mathcal{F}} v_{syn}^{s,c,f} \tag{3.3}$$

believing that *amplitude distribution among all stations* is what determines the physics of the source. Our results have not proven this hypothesis though.

3.2 Improved strike, dip, rake retrieval

The above stated normalization (3.2, 3.3) is extremely dependent on station selections, as well as on local site conditions. Theoretically, uniform *shapes of observed and synthetic spectra* may produce a non-zero error value due to the inadequate global scaling, while we expect a perfect fit at each station. Such a method is liable to giving non-robust solutions, which we cannot admit.

We therefore removed the summation over $\mathcal{S}$ and altered the formulae for computing the normalized spectra to

$$\bar{v}_{obs}^{s,c,f} = \frac{v_{obs}^{s,c,f}}{V_{obs}^{s}} \qquad \bar{v}_{syn}^{s,c,f} = \frac{v_{syn}^{s,c,f}}{V_{syn}^{s}} \tag{3.4}$$

$$V_{obs}^{s} = \sum_{\mathcal{C}} \sum_{\mathcal{F}} v_{obs}^{s,c,f} \qquad V_{syn}^{s} = \sum_{\mathcal{C}} \sum_{\mathcal{F}} v_{syn}^{s,c,f} \tag{3.5}$$

making the scaling strictly related to individual stations. In section 9.2 we provide comments on how normalization affects the results.

3.3 Moment retrieval

Seismic moment retrieval used to be realized by a grid search, too (see [2, 3]), but there had been a substantial improvement shortly before we set to work (see [1]). For the three parameters ϕ_E, δ_E, λ_E minimizing E, a frequency dependent moment reads

$$M^f = \frac{1}{n_{sc}^f} \sum_{\mathcal{S}} \sum_{\mathcal{C}} \frac{v_{obs}^{s,c,f}}{v_{syn}^{s,c,f}} \tag{3.6}$$

$$n_{sc}^f = \sum_{\mathcal{S}} \sum_{\mathcal{C}} \mathrm{def}\,(v_{syn}^{s,c,f}).$$

Scalar seismic moment is simply an average of M^f over the entire inversion frequency domain

$$M_0 = \frac{1}{n_f} \sum_{\mathcal{F}} M^f \tag{3.7}$$

$$n_f = \sum_{\mathcal{F}} \mathrm{def}\,(M^f)$$

and can transform to moment magnitude using $M_w = 0.67 * \log_{10} M_0 - 6.03$.

3.4 Common steps in ASPO computation

Usage of the method is not straightforward for two reasons. Firstly, complexity of both the input and the output data requires human judgement. Secondly, stress has been laid on getting the results so far, not on clear implementation and automated data interchange.

No matter how costly the current state of things seems, there are some principal steps to be taken during the retrieval:

1. Fix a located event to invert.
2. Select several acceptable velocigrams so that the stations they originate from encircle the event and spread evenly (if applicable, of course).
3. Transform all geographical co-ordinates into a local Cartesian reference system. The origin is at an arbitrary surface point, X pointing northward, Y eastward and Z upward.
4. Calculate azimuth and epicentral distance of each station.

5. Describe your seismic model. Since depth determination is a surplus of the whole computational procedure, the 1-D layered model may differ from the one you located in (see [2] for details).

6. Decide whether to invert in NEZ (north, east, vertical) or RTZ (radial, transversal, vertical) systems. Take each waveform and compute its spectrum. Performance of standard pre-processing operations (trend--line or baseline correction, window tapering etc.) is assumed.

7. Calculate the spectrum of the Green tensor. Run the program for a couple of "copies" of hypocentres differing in depth. Note that hypocentres and model interface may not concur (with respect to ray-methods used in item 10).

8. For each relevant station $s \in \mathcal{S}$ and spectral component $c \in \mathcal{C}$ define the inversion frequency domain $\mathcal{F}$ of your interest. Set grid search ranges and increments of ϕ, δ, λ globally for $\mathcal{S}$.

9. Run the main program which calculates synthetic spectra and implements the grid search using (3.1, 3.5, 3.4 and 3.6). You will obtain the complete error function E. Individual contribution of each station to the outermost sum of (3.1) is also saved.

10. Polarity agreement can be checked for an arbitrary set of stations (regardless of $\mathcal{S}$). Select those which have clear first-arrival onsets. Mark the observed polarities and state stations' azimuths. In accordance with your model, calculate the take-off angle of the first ray reaching the particular station, considering either direct P wave or MOHO Pn head wave. Head waves from intracrustal discontinuities should be ignored (as discussed in [2]).

11. Run the polarity check program. It verifies the agreement of all observed and synthetic polarities for each ϕ, δ, λ. Let us denote the satisfactory triplet with the least E by ϕ_P, δ_P, λ_P. Preserving the relevant information output by the main program, the polarity check returns a list of solutions for which the two conditions are met:

    (a) all observed and synthetic polarities agree

    (b) $E(\phi, \delta, \lambda) < q * E(\phi_P, \delta_P, \lambda_P)$, $q > 1$ being a reasonable constant

For such ϕ, δ, λ, let us define $P(\phi, \delta, \lambda) = E(\phi, \delta, \lambda)$ as a restriction of the overall error function (in other words, the definition range of P equals the set of solution triplets). Note that $P(\phi_P, \delta_P, \lambda_P)$ is the minimum of P.

12. Render, tabulate and discuss the results. See the graph of $P(\phi_P, \delta_P, \lambda_P)$ versus hypocentre depth to appoint the most appropriate vertical position of the source.

Chapter 4

Fixed Inversion Parameters

In the chapters to come, we will focus on the four aftershocks specified in Tabs. 4.1, 4.2. The first three digits of the code mean the rank of the day within the year, the rest is the starting time of the record. The information comes from HYPO output files, M_0 is calculated from M_L just for reference. Location depth will be discussed later based on our own results.

Code	Lat N (deg)	Lon E (deg)	Depth (km)
2601730	38.070	23.674	10.36
2671010	38.074	23.579	13.43
2761700	38.096	23.759	8.04
2780500	38.092	23.753	8.35

Table 4.1: Aftershocks being inverted. See Tab. 4.2.

Code	Date	Origin Time	M_L	M_0 (Nm)
2601730	99/09/17	17:37:59.77	2.43	$4.2*10^{12}$
2671010	99/09/24	10:16:54.82	3.04	$3.4*10^{13}$
2761700	99/10/03	17:03:33.99	3.22	$6.4*10^{13}$
2780500	99/10/05	05:04:02.98	1.96	$8.4*10^{11}$

Table 4.2: Continuation of Tab. 4.1.

Before getting to individual aftershock inversions, we shall specify the data which do not vary. Our structural model (Tab. 4.3) consists of four

Depth (km)	v_p (km/s)	v_s (km/s)	ρ (g/cm^3)	Q_p	Q_s
0.0	3.00	1.69	2.300	200.0	100.0
0.9	5.50	3.09	2.800	300.0	150.0
6.0	6.00	3.37	2.900	300.0	150.0
15.0	6.50	3.65	3.000	300.0	150.0
25.0	8.20	4.61	3.340	1000.0	500.0

Table 4.3: Inversion model layers (delimited by the depth of their top).

parallel layers atop a half-space, all being homogenous and isotropic media. It is identical to the one in which HYPO location was performed.

Our goal is to fix as many inversion parameters as possible in order to facilitate mutual comparison of the results. We will work in RTZ system with no preference of any component at any station, i.e.

$$\mathcal{C} = \{\mathrm{R}, \mathrm{T}, \mathrm{Z}\}.$$

Further, frequency range can be made independent of stations and components. Having scanned a number of aftershock spectra, we set the inversion frequency domain to

$$\mathcal{F} = \langle f_{min}, f_{max} \rangle \cap \{k * \Delta f;\ k = 1, 2, \ldots\}$$

$$f_{min} = 1.0 \text{ Hz} \qquad f_{max} = 2.0 \text{ Hz} \qquad \Delta f = 50/4096 \text{ Hz},$$

keeping well below any corner frequency f_c.

Grid search over the three focal parameters is performed in the following manner:

$$\phi \in \Phi = \langle \phi_{min}, \phi_{max} \rangle \cap \{\phi_{min} + k * \Delta\phi;\ k = 0, 1, \ldots\}$$

$$\delta \in \Delta = \langle \delta_{min}, \delta_{max} \rangle \cap \{\delta_{min} + k * \Delta\delta;\ k = 0, 1, \ldots\}$$

$$\lambda \in \Lambda = \langle \lambda_{min}, \lambda_{max} \rangle \cap \{\lambda_{min} + k * \Delta\lambda;\ k = 0, 1, \ldots\}$$

$$\begin{array}{lllllllll} \phi_{min} & = & 0^\circ & \phi_{max} & = & 360^\circ & \Delta\phi & = & 10^\circ \\ \delta_{min} & = & 0^\circ & \delta_{max} & = & 90^\circ & \Delta\delta & = & 10^\circ \\ \lambda_{min} & = & 0^\circ & \lambda_{max} & = & 180^\circ & \Delta\lambda & = & 10^\circ \end{array}$$

Note that amplitude spectra for λ and $\lambda - 180^\circ$ are equivalent, E need not be computed for the other angle of the pair. The implied ambiguity is resolved

by the polarity check. If all synthetic polarities are adverse for λ, then they all match for $\lambda - 180°$, and vice versa, otherwise no solution is found for either of these rakes.

Once the grid search ranges are set, each triplet of ϕ, δ, λ is assigned a trial number T according to its order in the computation sequence. The transformation formula reads

$$T = \frac{\phi - \phi_{min}}{\Delta\phi} * |\Delta| * |\Lambda| + \frac{\delta - \delta_{min}}{\Delta\delta} * |\Lambda| + \frac{\lambda - \lambda_{min}}{\Delta\lambda} + 1,$$

$|\Delta|$ and $|\Lambda|$ respectively standing for the number of elements in Δ and Λ.

For the determination of the definition range of P (item 11 on page 24), we fix $q = 1.05$.

There are still many parameters to experiment with. We will carry out a variety of computations for each event, altering station sets and reducing polarity check-points. In order to substantiate our improvement of the inversion algorithm, parallel results for both types of normalization (3.4, 3.5 versus 3.2, 3.3) will be presented.

Chapter 5

Aftershock 2671010

Ten stations with the most acceptable velocigrams were used for the inversion, although the resulting coverage of azimuth was questionable (Tab. 5.1, Fig. 5.1). With respect to multiple splitting of the computation, we denote each display by the code of the aftershock and the symbol of the branch taken, i.e. 2671010 AX here indicates that the same station set relates both to computation A (improved normalization) and to computation X (former normalization).

First-arrival polarities were available from 20 stations (Tab. 5.2). Running the polarity check for all of them yields in fact a pure polarity solution because the constraint allows only a narrow strip of nodal lines on the focal sphere. Based on the amplitude spectra conformity criterion, the method is able to find the mechanism even if polarity information is limited. To verify this, we discard polarities from stations not engaged in the inversion of spectra, receiving a subset of 6 check-points (upper part of Tab. 5.2). Results involving the whole set are referred to as rich-polarity solutions, whereas the subset gives poor-polarity solutions.

5.0.1 Computation A/6

Figure 5.2 is of cardinal importance for it depicts all essential results and demonstrates the behaviour of the method. Error functions as well as poor--polarity beach balls are rendered for individual depths. The black line shows the values of $E(T)$ (clipped by the upper limit of the axis). Poor-polarity $P(T)$ is marked by the red smaller diamonds, while rich-polarity $P(T)$ appears in green colour and bigger size.

Id	Code	Lat N (deg)	Lon E (deg)	Azimuth (deg)	Distance (km)
2	NLI	38.038	23.701	110.52	11.40
5	FIL	38.104	23.670	67.26	8.62
9	KRY	38.141	23.828	71.05	23.00
11	BAR	38.135	23.791	69.86	19.73
13	PAR	38.153	23.737	57.52	16.36
16	RAF	38.018	23.995	99.58	36.92
22	VAR	38.223	23.916	60.55	33.78
23	KAL	38.262	23.873	50.79	33.10
26	ASP	38.062	23.589	146.83	1.60
31	VUL	37.807	23.785	148.62	34.72

Table 5.1: Stations engaged in the inversion (2671010 AX).

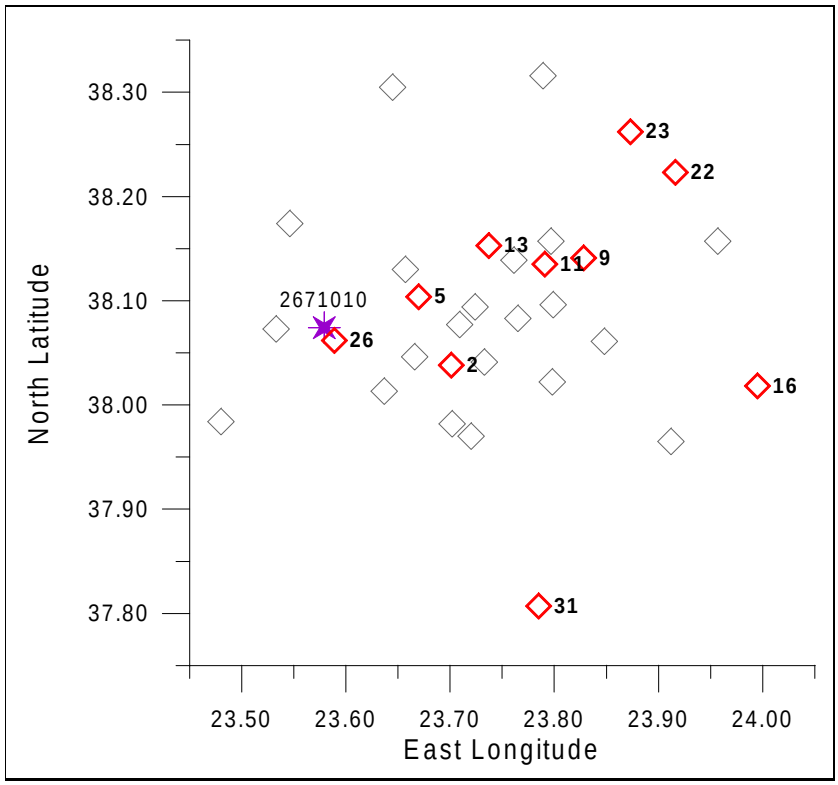

Figure 5.1: Aftershock epicentre & deployment of the stations (2671010 AX).

Code	Azim (deg)	Take-off Angles (deg)								Sign
KRY	71	99	106	112	117	113	120	124	128	U
PAR	57	106	115	121	127	126	131	135	139	U
RAF	99	94	98	102	106	97	104	109	113	D
VAR	60	95	100	104	108	99	107	112	116	U
KAL	50	95	100	104	108	100	107	112	116	U
VUL	148	95	99	103	107	98	106	111	115	U
LIO	88	117	126	133	138	139	143	146	149	D
MAG	268	149	155	159	162	163	165	167	168	D
FLD	105	111	120	126	132	132	137	140	144	D
INF	12	97	104	109	113	108	115	120	124	U
MEL	93	99	106	111	116	113	119	123	127	D
KIF	82	102	110	117	122	120	125	130	134	U
AHA	86	107	115	122	127	126	131	136	139	D
HAL	106	102	110	116	121	119	124	129	133	D
SPT	112	95	101	105	109	102	109	114	118	D
MAR	74	95	99	104	107	99	106	111	115	U
ORP	34	95	100	105	109	100	108	113	117	U
MEN	80	113	122	129	134	135	139	143	146	D
STE	345	117	126	132	138	138	143	146	149	U
HAI	143	127	135	142	146	147	151	154	156	D

Table 5.2: Stations providing polarity data & take-off angles of the first--arrival rays (depth increasing to the right, see depth plots) (2671010 AX).

The error graph shall not be interpreted without noticing the depth plot of $P(\phi_P, \delta_P, \lambda_P)$ for both polarity sets (Fig. 5.3, rich-polarity is on the left). The solid lines signalize the extreme values. The dashed line marks the minimal upper limit for P, thus distinguishing the lowest achievable band of solutions. The different character of the two functions correlates with alternate strictness of the nodal lines confinement apparent on the beach balls. If no rich-polarity solution can be found at the prescribed depth (as at 22.0 km in our case), the items in the graph are void.

The desired single solution of the problem should comply with as many following requirements as possible:

1. Rich-polarity solution intersects with poor-polarity solution.

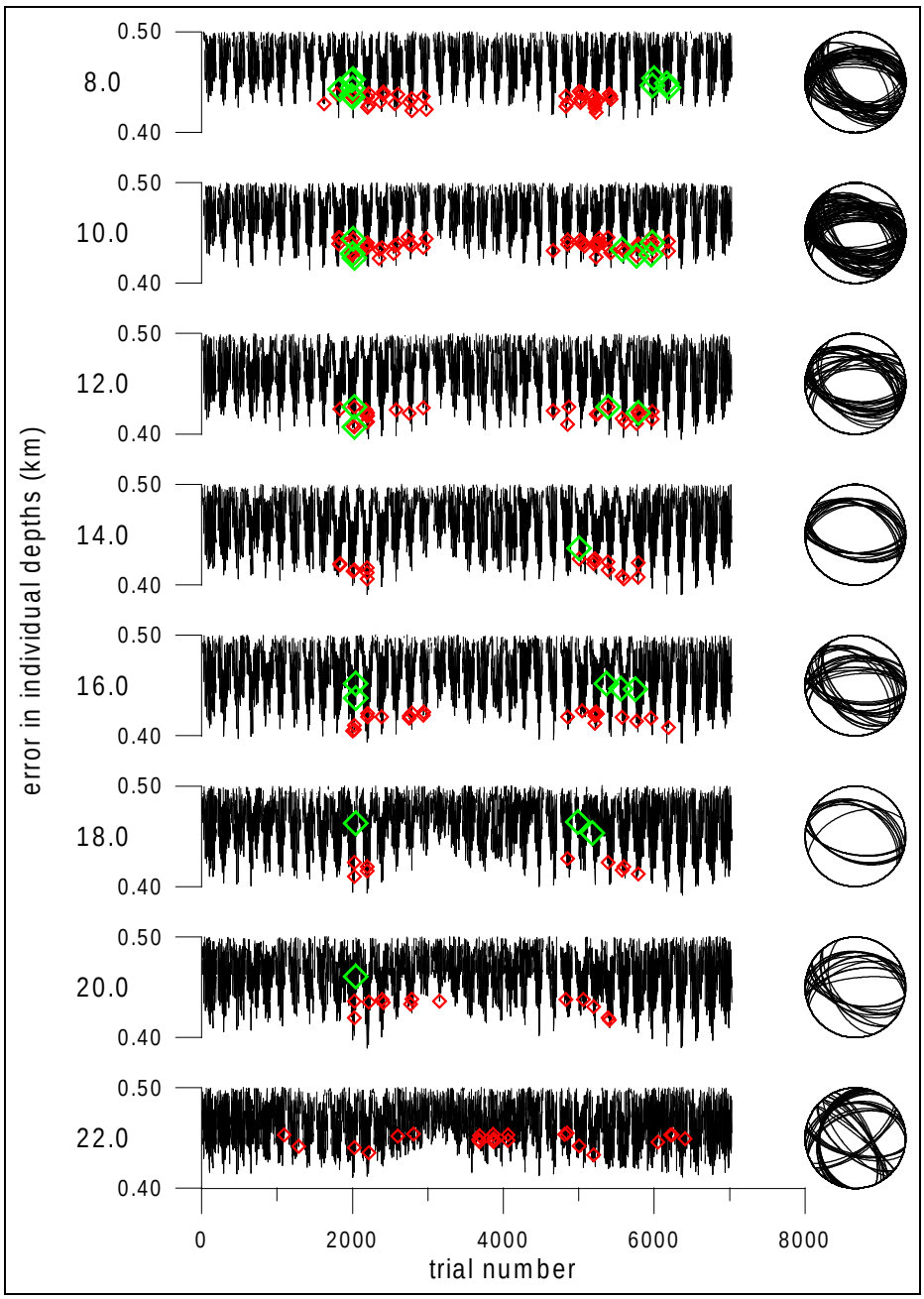

Figure 5.2: Depth plot of E (black), poor-polarity P (red) and rich-polarity P (green), along with poor-polarity beach balls (2671010 A/6).

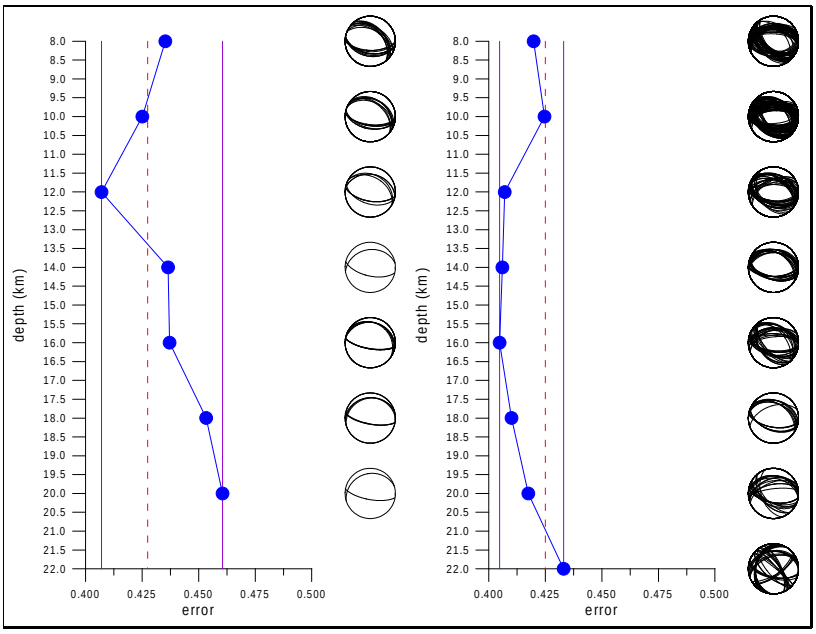

Figure 5.3: Depth plot of $P(\phi_P, \delta_P, \lambda_P)$ & beach balls (2671010 A/20, A/6).

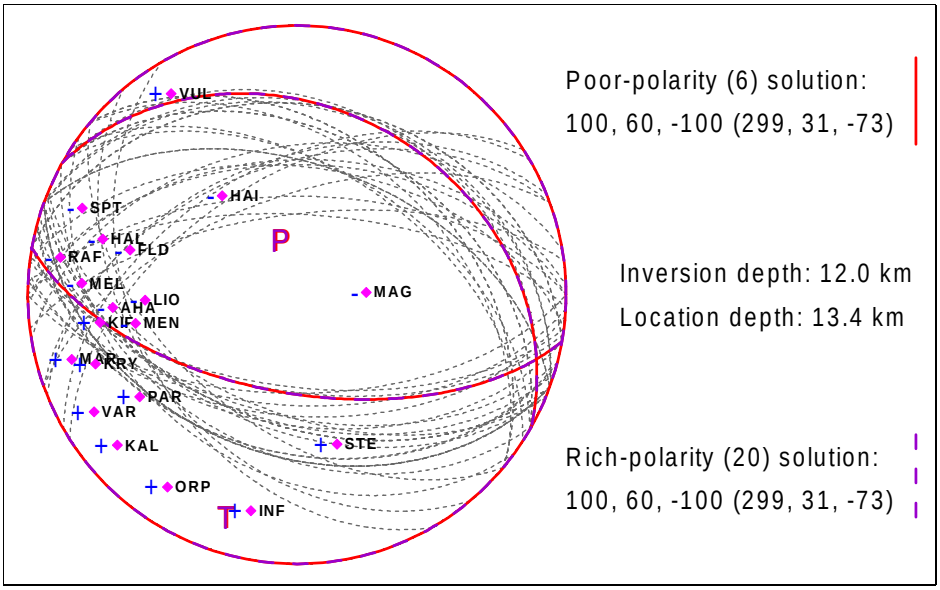

Figure 5.4: Nodal lines of solution at 12.0 km depth (2671010 A/6).

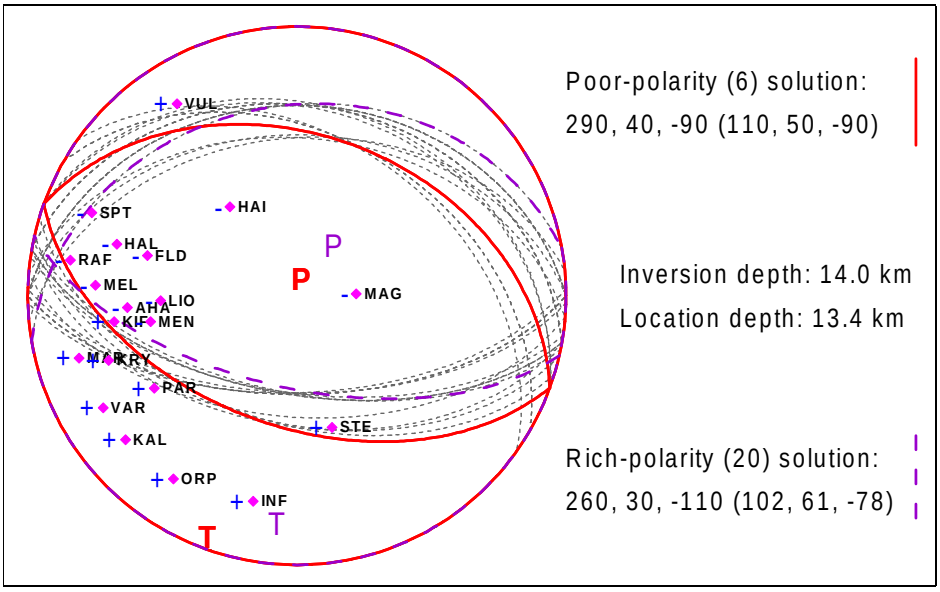

Figure 5.5: Nodal lines of solution at 14.0 km depth (2671010 A/6).

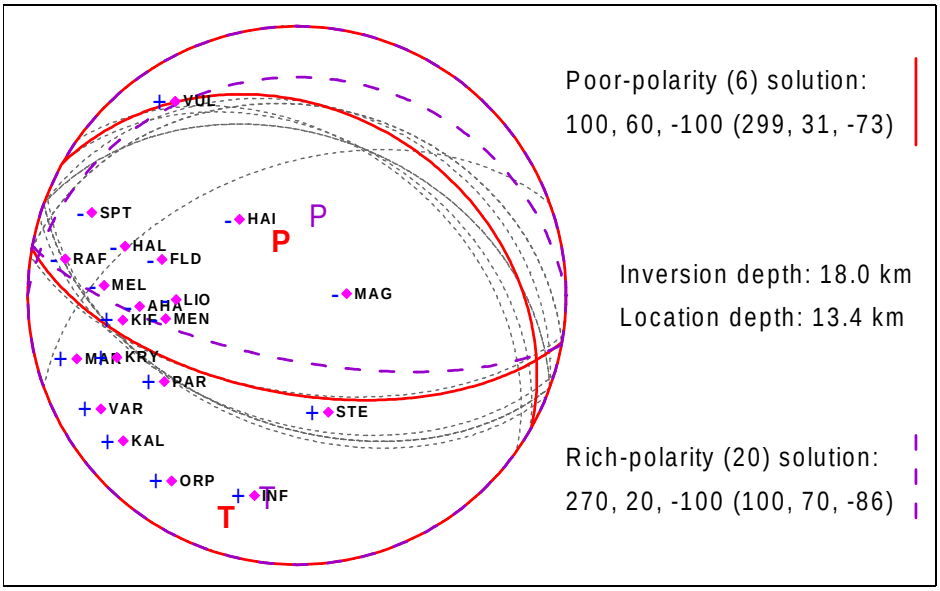

Figure 5.6: Nodal lines of solutions at 18.0 km depth (2671010 A/6).

2. Error function E has distinct minima and the solution occupies them.
3. Symbols of P cluster in groups rather than scatter over T.
4. Nodal lines do not deviate significantly one from another.
5. Hypocentre depth of the solution candidate is consistent with the minima of the depth plot of $P(\phi_P, \delta_P, \lambda_P)$.

As a necessary condition, poor-polarity solution must not be suggested if rich-polarity solution does not exist at the same depth.

Going over the graphs again, we see that 12.0 km depth is well resolved and the solution satisfies four of the above items. Nodal lines are trimmer at depths of 14.0 km and 18.0 km, but the ranges of P are disjunct there.

Nevertheless, we present beach balls of all these solutions (Figs. 5.4, 5.5, 5.6). Ordinary poor-polarity nodal lines are displayed as grey dashed curves, poor-polarity solution is marked by the red solid line, rich-polarity solution uses the violet dashed line. In addition, rich-polarity check-points project onto the focal sphere (labeled and signed purple diamonds). The solution triplet ϕ_P, δ_P, λ_P and its geometrical complement (in parentheses) are published numerically for each polarity set. Inversion and location depths, tension and pressure axes are depicted, too.

Seismic moment M_0 for ϕ_E, δ_E, λ_E at the respective depths of 12.0 km, 14.0 km and 18.0 km is $2.8 * 10^{11}$ Nm, $2.4 * 10^{11}$ Nm and $2.6 * 10^{11}$ Nm.

5.0.2 Computation X/6

This computation was run using the former normalization. The resulting graphs (Figs. 5.7, 5.8) lack any consistency between rich-polarity and poor--polarity solutions and the depth plot of $P(\phi_P, \delta_P, \lambda_P)$ has a yet unseen monotonous character.

In general, drawing serious conclusions from such results is more than doubtful. If we were to present a single solution anyway, we would point out the one at 14.0 km depth (Fig. 5.9). Moment is $M_0 = 4.7 * 10^{11}$ Nm.

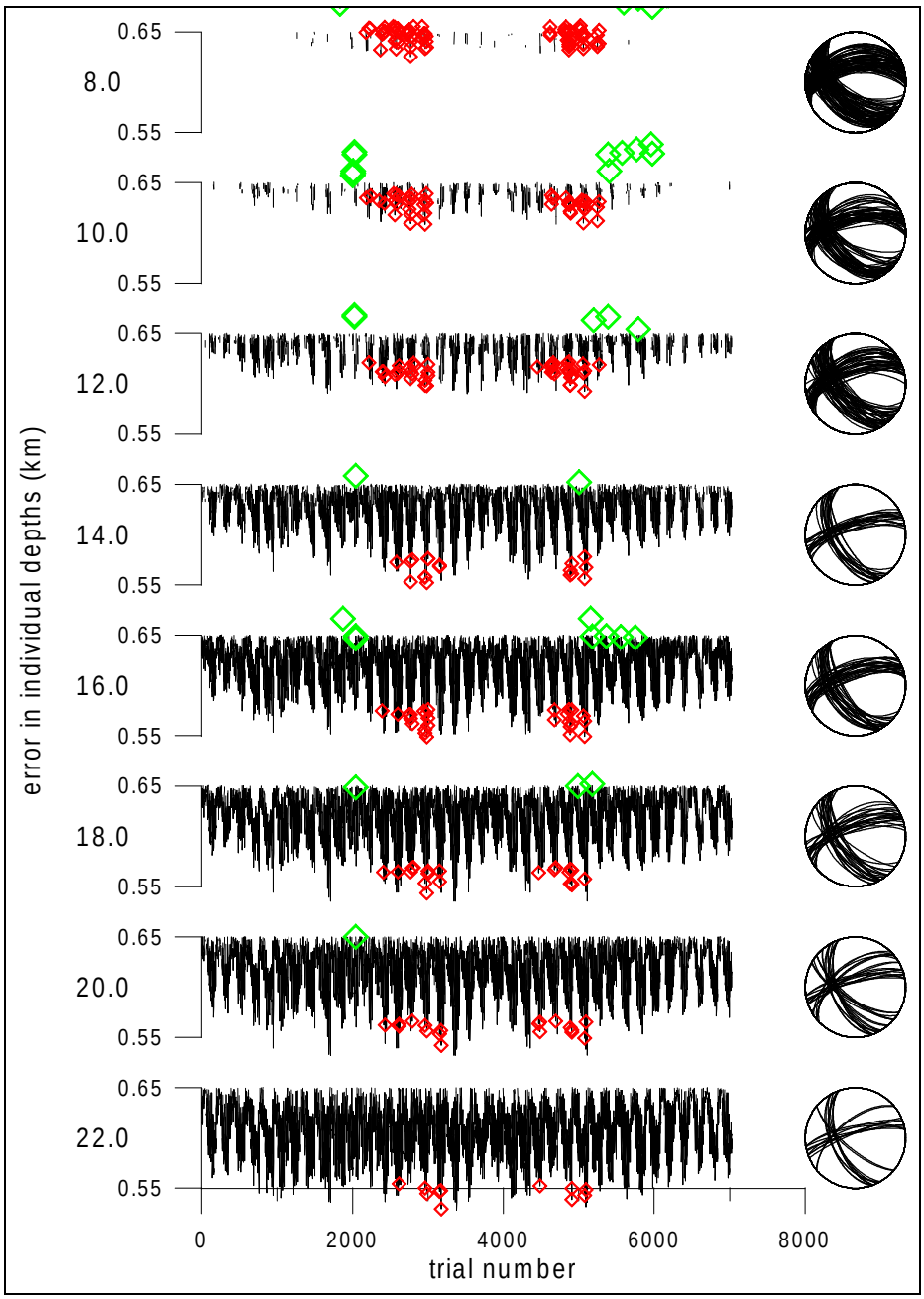

Figure 5.7: Depth plot of E (black), poor-polarity P (red) and rich-polarity P (green), along with poor-polarity beach balls (2671010 X/6).

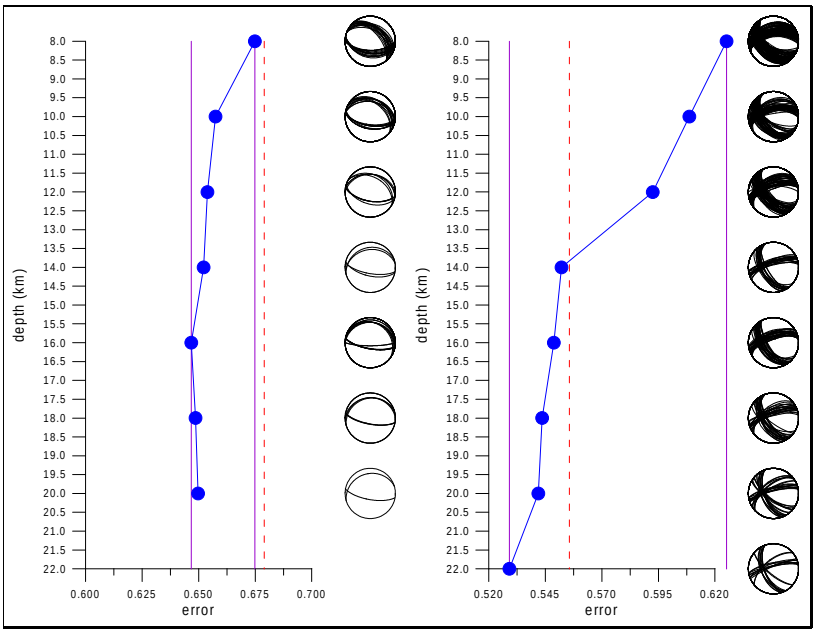

Figure 5.8: Depth plot of $P(\phi_P, \delta_P, \lambda_P)$ & beach balls (2671010 X/20, X/6).

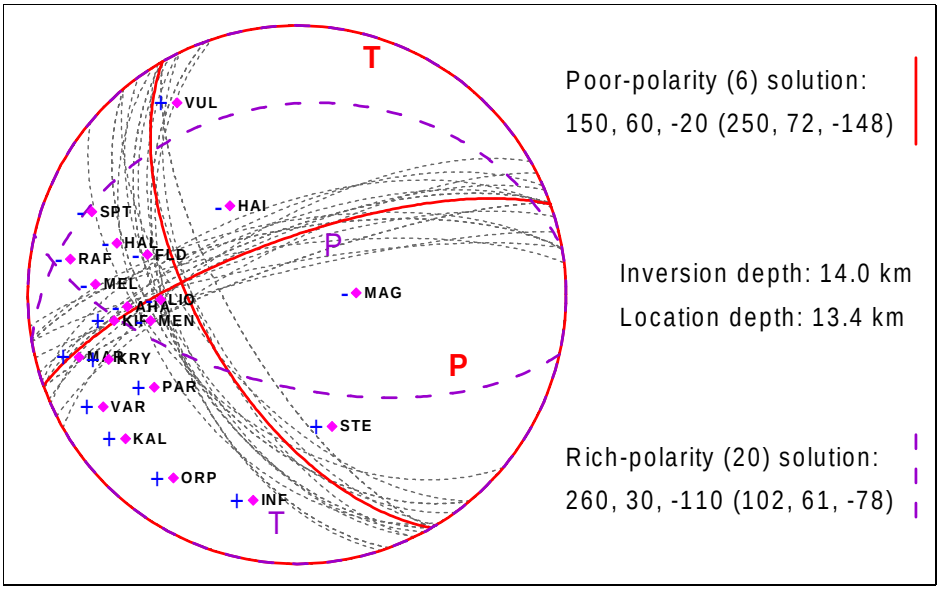

Figure 5.9: Nodal lines of solution at 14.0 km depth (2671010 X/6).

Chapter 6

Aftershock 2761700

Inversion of this aftershock forks enormously. Many records were found acceptable, and since it is interesting to study any effects of choice, two disjunct station sets were designed and the discrepant results discussed.

In the course of the retrieval, experimentation with check-points will be performed. We shall therefore recall the notation of displays consisting of the code of the aftershock, the computation branch (reflecting station sets and normalization) and the number of relevant polarity check-points.

6.1 First station set

We intended to use the station set 2671010 AX also for this inversion, yet only seven original stations were kept (Tab. 6.1, Fig. 6.1). The epicentre is situated well within the covered area.

First-arrival polarities were observed in 22 stations. By intersection with the inversion station set, we received a subset of 8 check-points. For the reasons stated below, we tested the method once more on the subset of 20 check-points. See Tab. 6.2 and mind the division lines. Inversion results are organized into separate subsections so that the terms rich-polarity and poor--polarity allow no misunderstanding.

6.1.1 Computation A/8

The error graph and the depth plot of $P(\phi_P, \delta_P, \lambda_P)$ (Figs. 6.2, 6.3, mind different error ranges) are not satisfactory when applying all available check-

Id	Code	Lat N (deg)	Lon E (deg)	Azimuth (deg)	Distance (km)
5	FIL	38.104	23.670	276.52	7.83
11	BAR	38.135	23.791	32.84	5.15
13	PAR	38.153	23.737	343.10	6.62
15	MEL	38.061	23.848	116.54	8.70
20	SPT	37.965	23.912	137.35	19.78
22	VAR	38.223	23.916	44.14	19.67
23	KAL	38.262	23.873	28.33	20.96
26	ASP	38.062	23.589	255.79	15.34
27	STE	38.174	23.546	295.02	20.53
31	VUL	37.807	23.785	175.94	32.19

Table 6.1: Stations engaged in the inversion (2761700 AX).

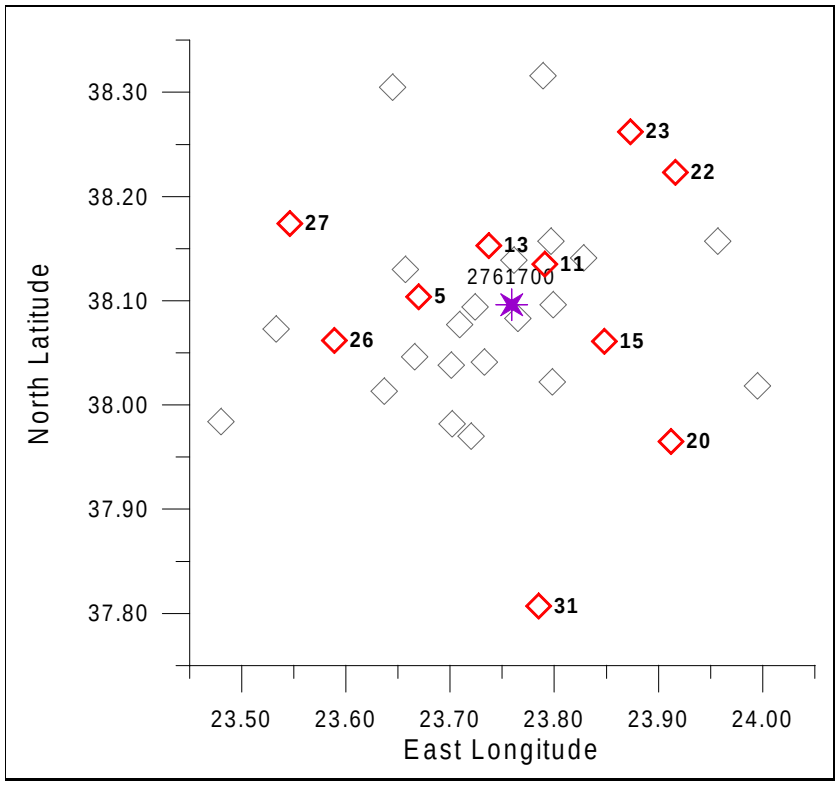

Figure 6.1: Aftershock epicentre & deployment of the stations (2761700 AX).

Code	Azim (deg)	Take-off Angles (deg)								Sign
BAR	32	133	135	140	145	148	151	153	155	U
PAR	343	126	126	132	137	141	144	147	150	D
MEL	116	119	116	123	128	133	136	139	142	D
SPT	137	103	93	99	104	108	112	115	117	D
VAR	44	103	93	100	104	108	112	115	118	U
KAL	28	102	93	98	103	107	110	113	116	U
STE	295	102	93	99	103	107	111	114	116	D
VUL	175	98	91	94	96	99	101	104	106	U
GEO	201	109	100	109	114	118	122	125	128	U
LIO	244	135	137	142	146	150	152	155	157	U
MKL	292	116	112	120	125	129	133	136	139	D
FLD	200	127	127	133	138	141	145	147	150	U
KRY	50	121	120	127	132	136	139	142	145	U
THR	2	136	137	143	147	150	153	155	157	D
RAF	112	101	92	97	102	105	109	111	114	D
AHA	160	163	164	166	168	169	170	171	172	U
HAL	157	118	115	122	128	132	135	139	141	U
MAR	68	104	94	101	106	110	113	116	119	U
ORP	6	100	92	96	100	103	106	109	112	U
HAI	229	108	99	108	113	117	121	124	127	U
KIF	90	145	147	151	155	157	159	161	163	U
MEN	265	148	150	154	157	160	162	163	165	D

Table 6.2: Stations providing polarity data & take-off angles of the first--arrival rays (depth increasing to the right, see depth plots) (2761700 AX).

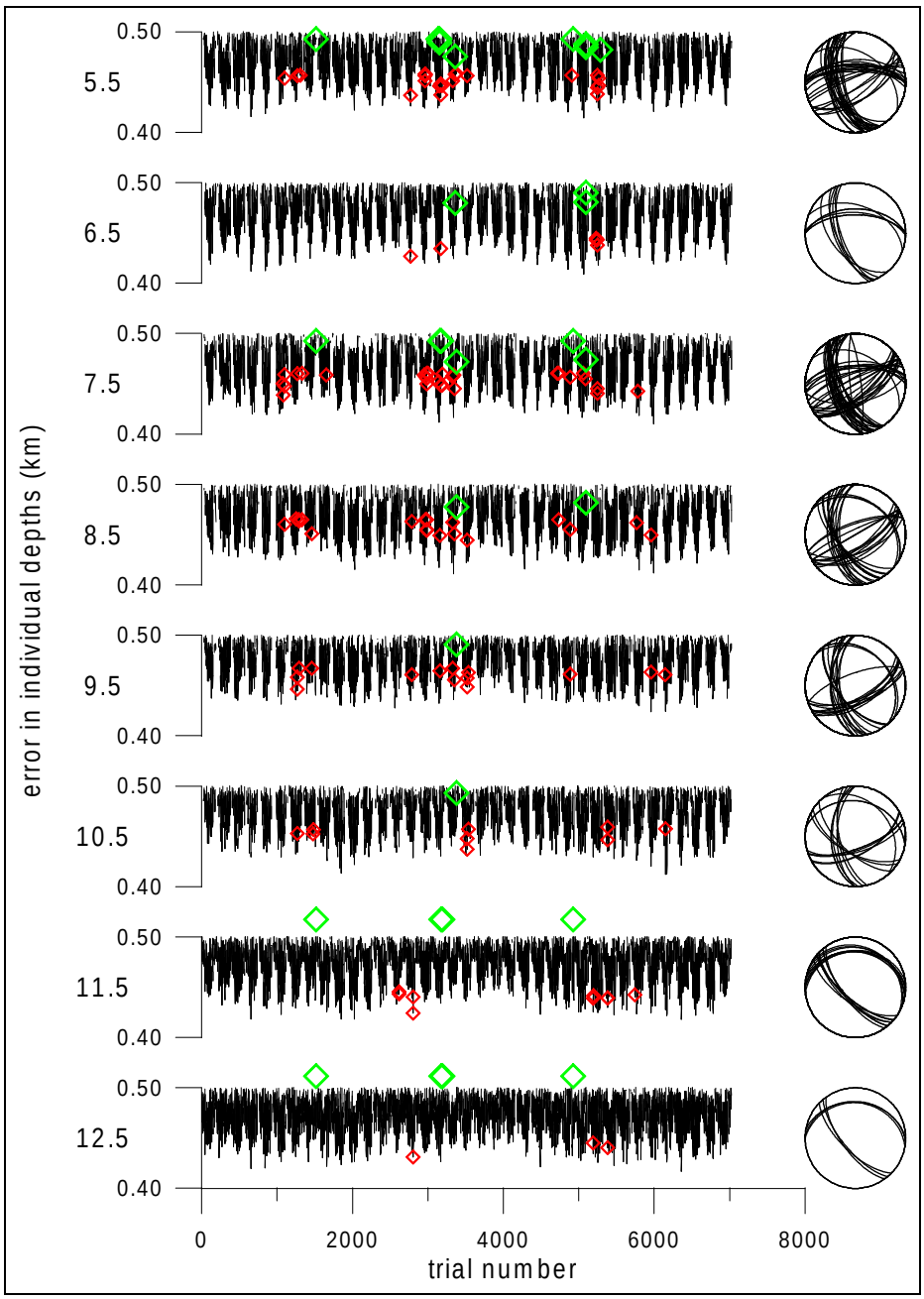

Figure 6.2: Depth plot of E (black), poor-polarity P (red) and rich-polarity P (green), along with poor-polarity beach balls (2761700 A/8).

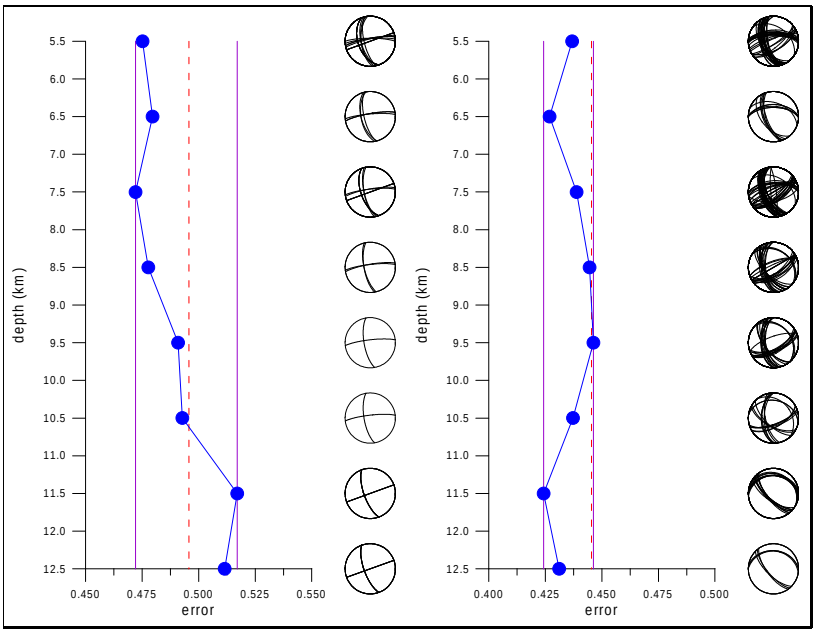

Figure 6.3: Depth plot of $P(\phi_P, \delta_P, \lambda_P)$ & beach balls (2761700 A/22, A/8).

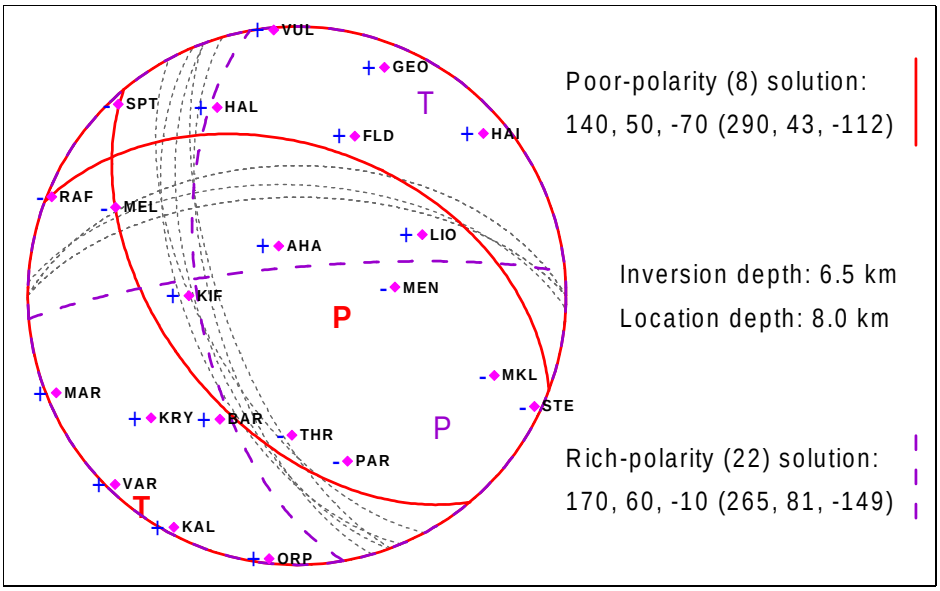

Figure 6.4: Nodal lines of solution at 6.5 km depth (2761700 A/8).

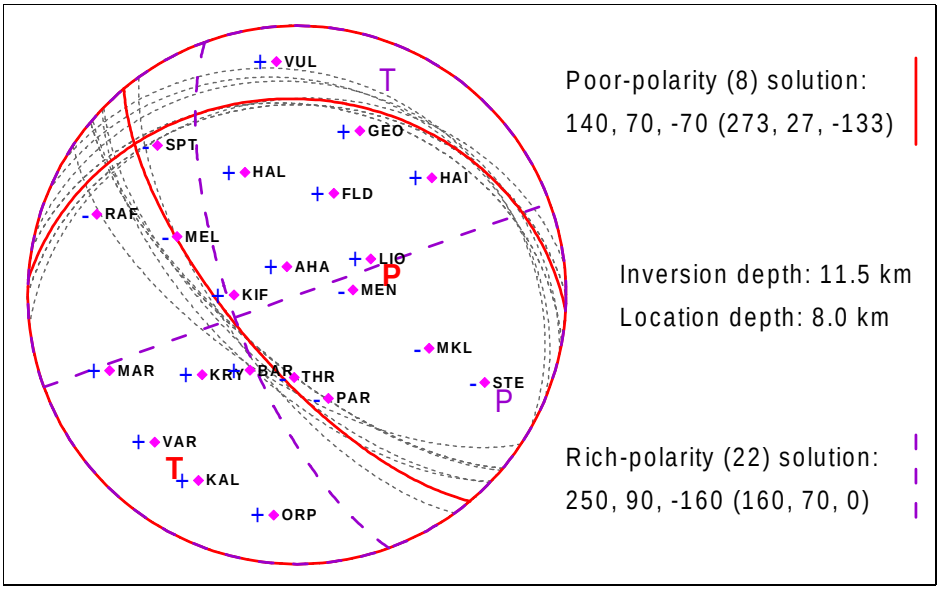

Figure 6.5: Nodal lines of solution at 11.5 km depth (2761700 A/8).

-points. The rich-polarity P does not get down to the minima of E, but at least the poor-polarity P does. Hypocentre depth is not resolved well (note that almost all minima of P lie within the lowest achievable band of solutions) unless nodal lines trimness is required. Solutions at 6.5 km and 11.5 km depth are shown (Figs. 6.4, 6.5), the seismic moment M_0 being $1.2 * 10^{12}$ Nm and $2.1 * 10^{12}$ Nm respectively.

6.1.2 Computation A/20

The discrepancy between previous rich-polarity and poor-polarity solutions is striking. We were interested in whether removal of some check-points would enable closer concord. We ignored the check-points KIF and MEN, hoping to support strike-slip solutions in intermediate depths. As we see in Figs. 6.6 and 6.7, such intervention was not sufficient. Some freedom for nodal lines determination was gained, however no poor-polarity solution appears below the best rich-polarity one, except for 5.5 km and 10.5 km depths where the shift is negligible. This failure deserves more discussion, see chapter 9.

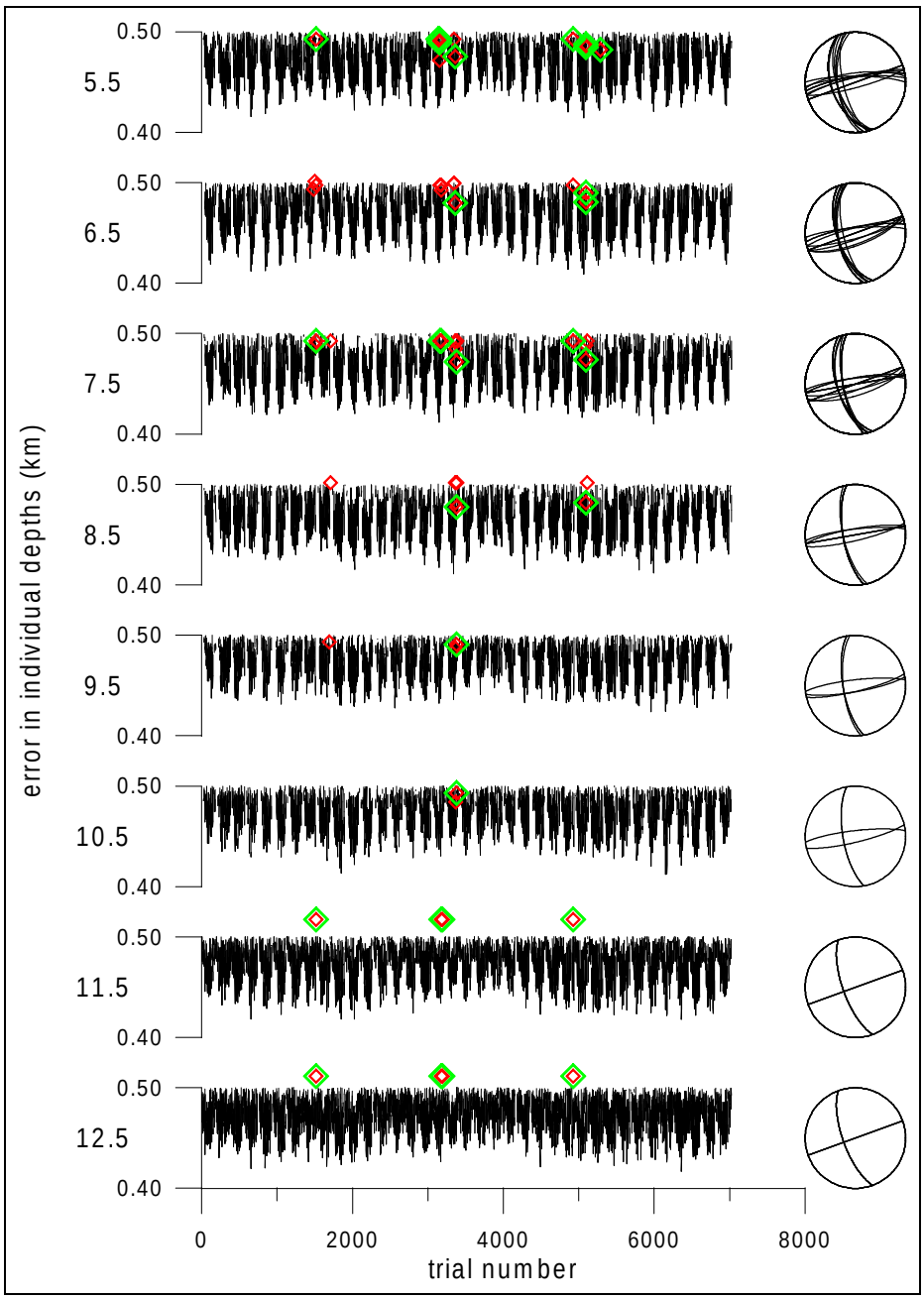

Figure 6.6: Depth plot of E (black), poor-polarity P (red) and rich-polarity P (green), along with poor-polarity beach balls (2761700 A/20).

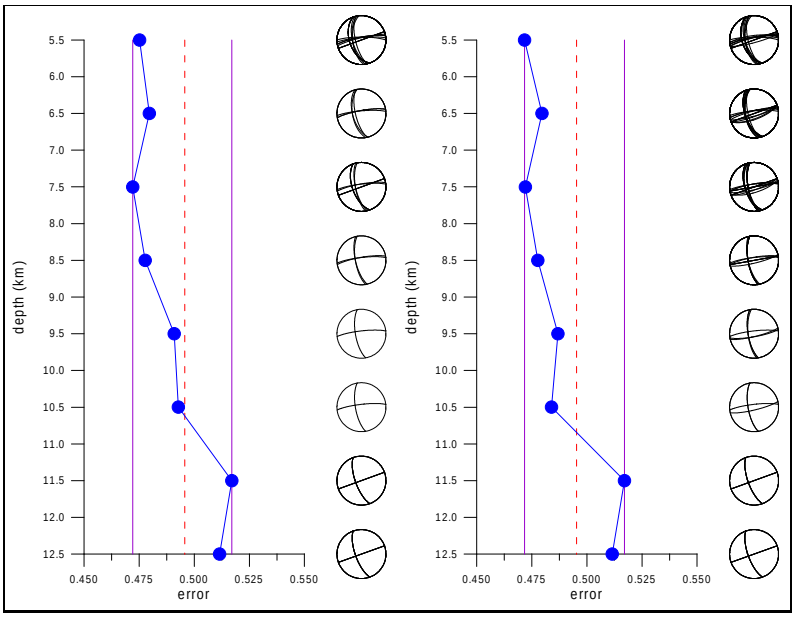

Figure 6.7: Depth plot of $P(\phi_P, \delta_P, \lambda_P)$ & beach balls (2761700 A/22, A/20).

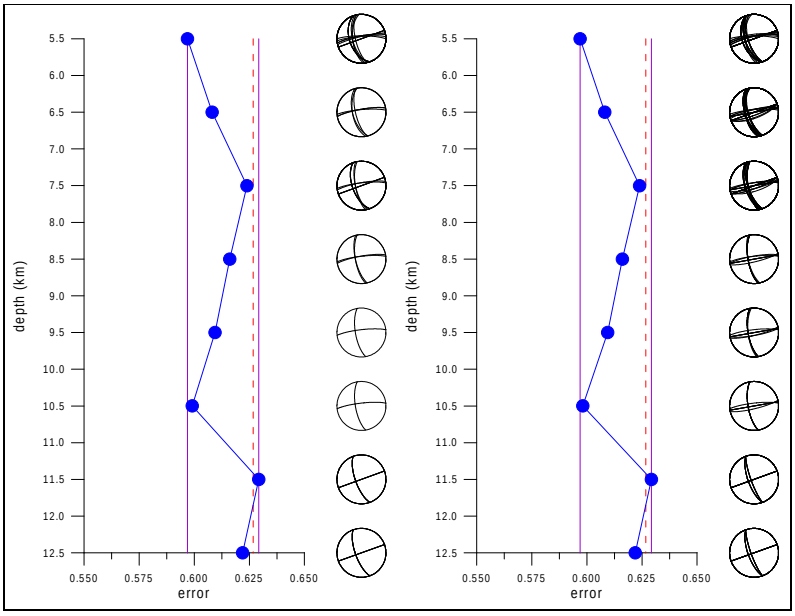

Figure 6.8: Depth plot of $P(\phi_P, \delta_P, \lambda_P)$ & beach balls (2761700 X/22, X/20).

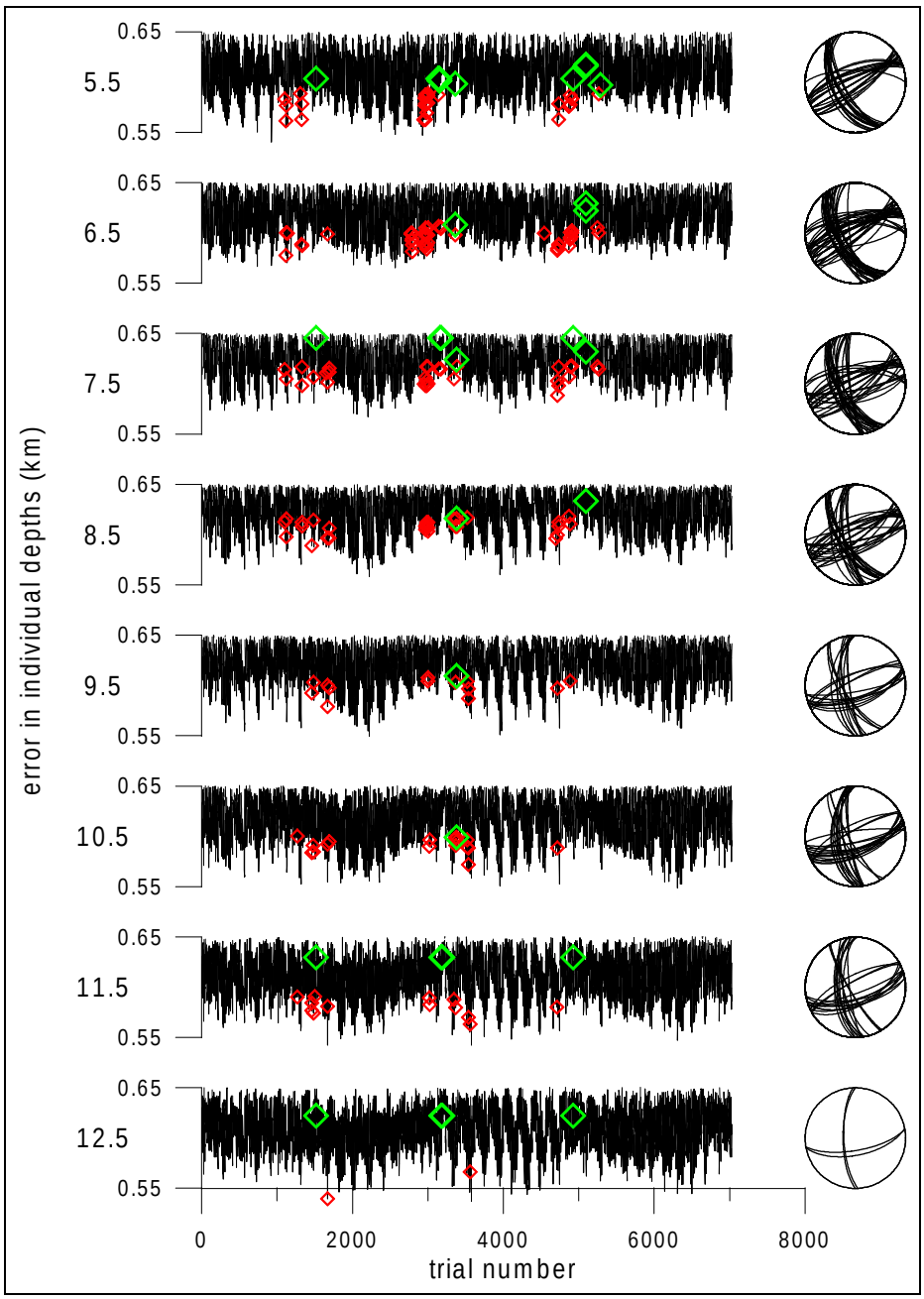

Figure 6.9: Depth plot of E (black), poor-polarity P (red) and rich-polarity P (green), along with poor-polarity beach balls (2761700 X/8).

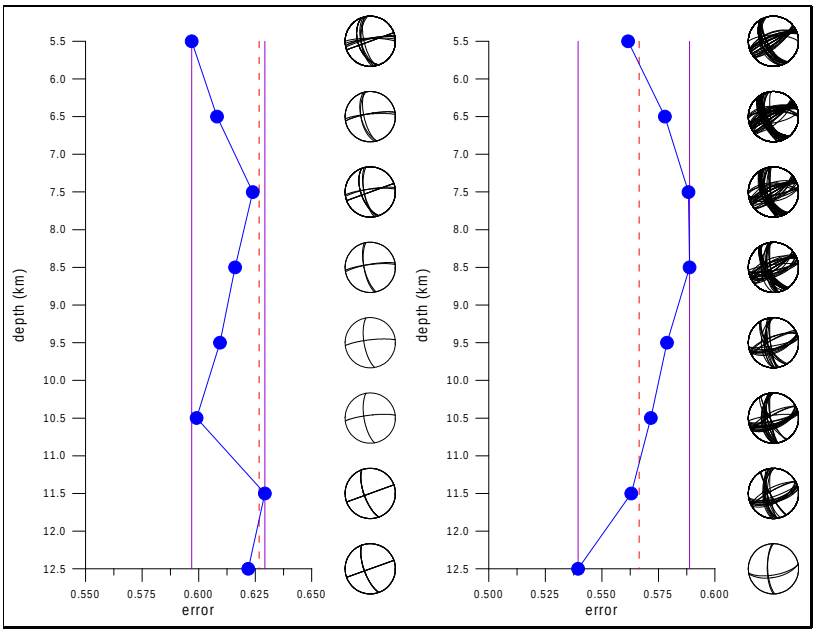

Figure 6.10: Depth plot of $P(\phi_P, \delta_P, \lambda_P)$ & beach balls (2761700 X/22, X/8).

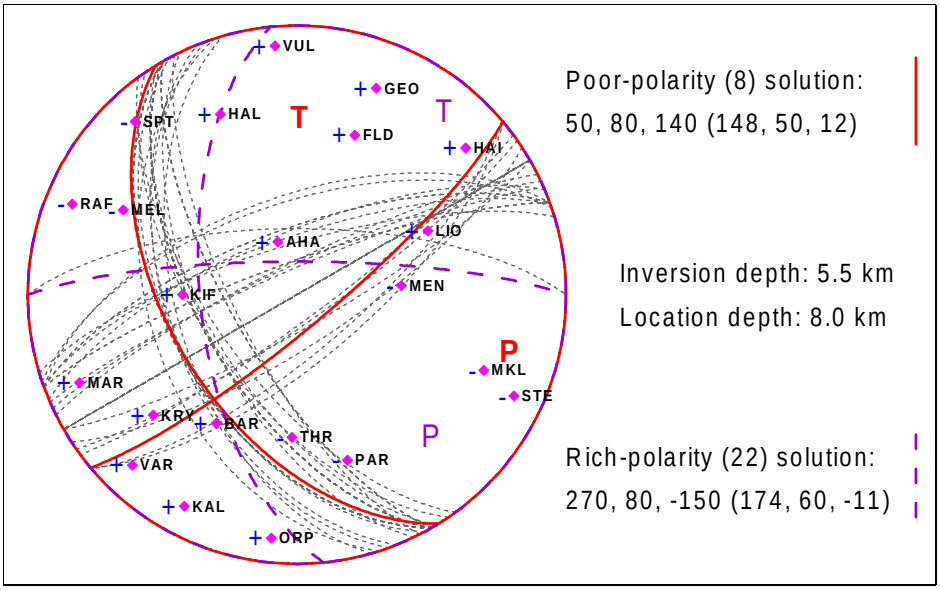

Figure 6.11: Nodal lines of solution at 5.5 km depth (2761700 X/8).

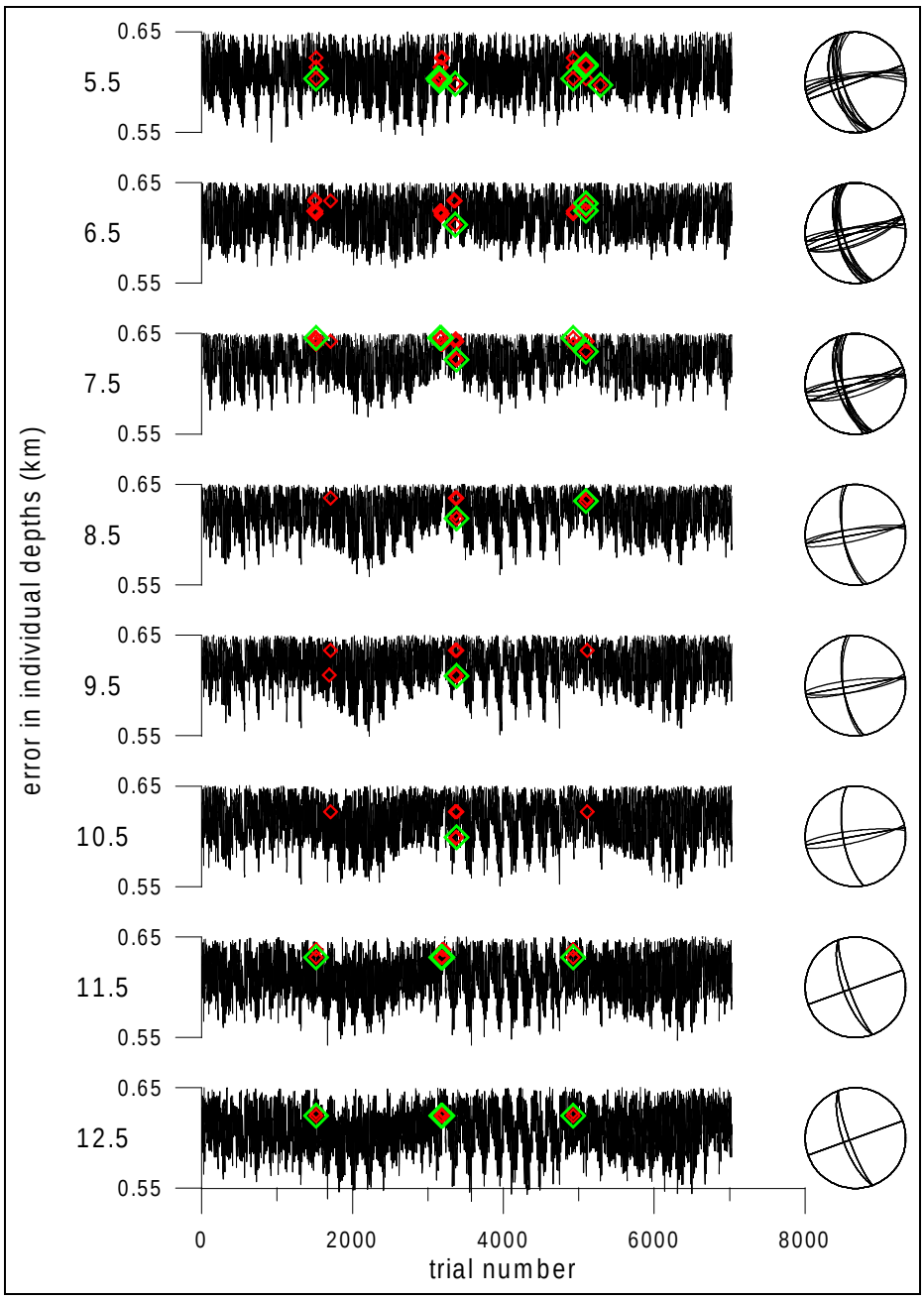

Figure 6.12: Depth plot of E (black), poor-polarity P (red) and rich-polarity P (green), along with poor-polarity beach balls (2761700 X/20).

6.1.3 Computation X/8

As regards joint minima of the error functions, the former way of normalization fails (Fig. 6.9). Dip-slip solutions are suppressed (compare with Figs. 6.4, 6.5), which was also the case in computation 2671010 X. Concavity of the depth plot of $P(\phi_P, \delta_P, \lambda_P)$ is very unfavourable. Solution at 5.5 km depth is presented (Fig. 6.11), $M_0 = 1.2 * 10^{12}$ Nm.

6.1.4 Computation X/20

This computation is analogous to 2761700 A/20, similar comments on the results (Fig. 6.12 and Fig. 6.8 on page 45) can be made.

6.2 Second station set

As there were ten more acceptable velocigrams left, we repeated the whole inversion for the set of remaining stations (Tab. 6.3, Fig. 6.13). The epicentre is encircled well, but compared to Fig. 6.1, stations are not so distant.

The set of 22 check-points stays unchanged, its intersection with the inversion station set yields 8 check-points. For testing purposes, 6 check-points out of these were specified. See Tab. 6.4 and mind the division lines.

6.2.1 Computation B/8

In contrast with the disputable error graph (Fig. 6.14), clarity of solution at 9.5 km depth is surprising (Fig. 6.16). Nodal lines of the solution seem to be nailed at check-points LIO and MEN, which maybe prevents any settlement of the poor-polarity P into the minima of E.

Depth resolution for 22 check-points resembles the one for the first station set (Figs. 6.15, 6.3 respectively). Seismic moment at the solution depth is $M_0 = 8.0 * 10^{11}$ Nm.

6.2.2 Computation B/6

If we apply the reduced subset of check-points, significantly different solutions appear (Figs. 6.17, 6.18). Though being the best, solution at 6.5 km depth features too much freedom (Fig. 6.19). Resultant $M_0 = 7.0 * 10^{11}$ Nm.

Id	Code	Lat N (deg)	Lon E (deg)	Azimuth (deg)	Distance (km)
1	GEO	37.982	23.702	201.51	13.62
3	PET	38.046	23.666	235.69	9.85
4	LIO	38.077	23.709	244.23	4.86
6	MKL	38.130	23.657	292.97	9.68
7	MAG	38.073	23.533	262.70	19.93
9	KRY	38.141	23.828	50.33	7.83
12	THR	38.139	23.761	2.08	4.78
16	RAF	38.018	23.995	112.70	22.39
17	KIF	38.096	23.799	90.03	3.50
25	MEN	38.094	23.724	265.82	3.07

Table 6.3: Stations engaged in the inversion (2761700 BY).

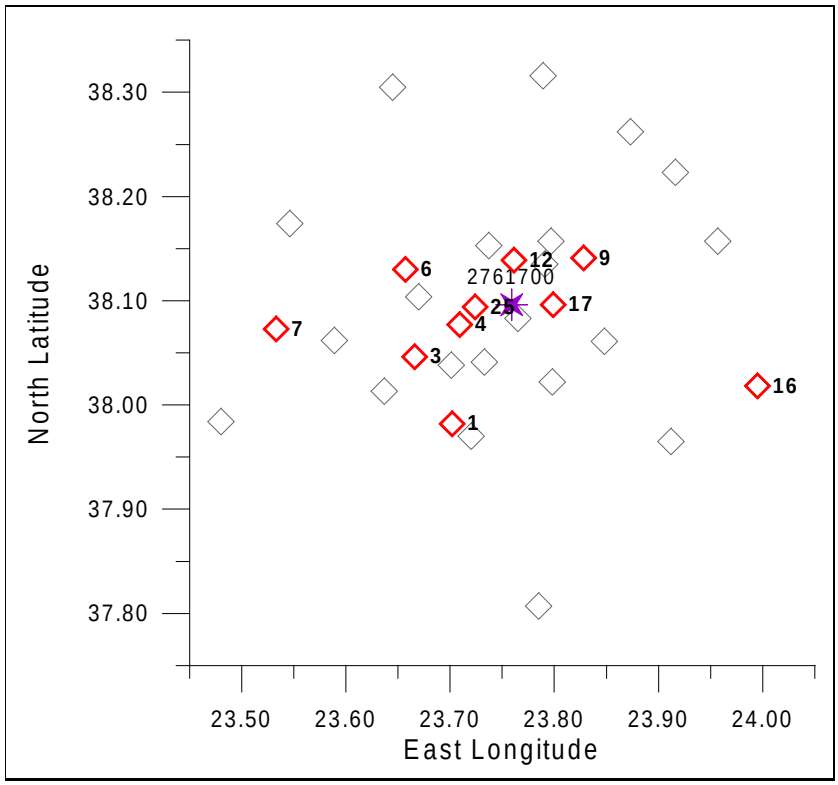

Figure 6.13: Aftershock epicentre & deployment of the stations (2761700 BY).

Code	Azim (deg)	Take-off Angles (deg)								Sign
GEO	201	109	100	109	114	118	122	125	128	U
MKL	292	116	112	120	125	129	133	136	139	D
KRY	50	121	120	127	132	136	139	142	145	U
THR	2	136	137	143	147	150	153	155	157	D
RAF	112	101	92	97	102	105	109	111	114	D
KIF	90	145	147	151	155	157	159	161	163	U
LIO	244	135	137	142	146	150	152	155	157	U
MEN	265	148	150	154	157	160	162	163	165	D
FLD	200	127	127	133	138	141	145	147	150	U
BAR	32	133	135	140	145	148	151	153	155	U
PAR	343	126	126	132	137	141	144	147	150	D
MEL	116	119	116	123	128	133	136	139	142	D
AHA	160	163	164	166	168	169	170	171	172	U
HAL	157	118	115	122	128	132	135	139	141	U
SPT	137	103	93	99	104	108	112	115	117	D
MAR	68	104	94	101	106	110	113	116	119	U
VAR	44	103	93	100	104	108	112	115	118	U
KAL	28	102	93	98	103	107	110	113	116	U
ORP	6	100	92	96	100	103	106	109	112	U
STE	295	102	93	99	103	107	111	114	116	D
HAI	229	108	99	108	113	117	121	124	127	U
VUL	175	98	91	94	96	99	101	104	106	U

Table 6.4: Stations providing polarity data & take-off angles of the first--arrival rays (depth increasing to the right, see depth plots) (2761700 BY).

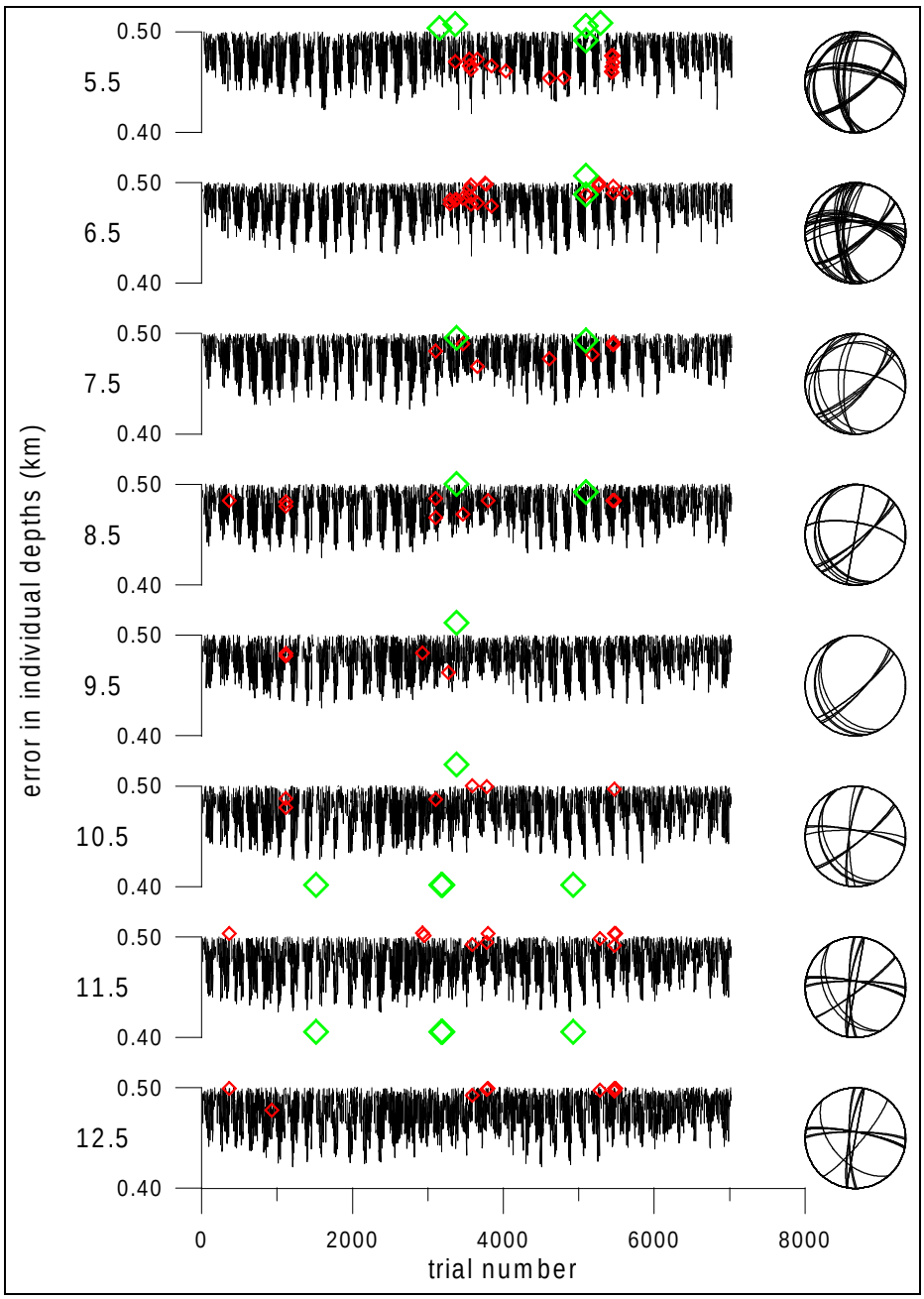

Figure 6.14: Depth plot of E (black), poor-polarity P (red) and rich-polarity P (green), along with poor-polarity beach balls (2761700 B/8).

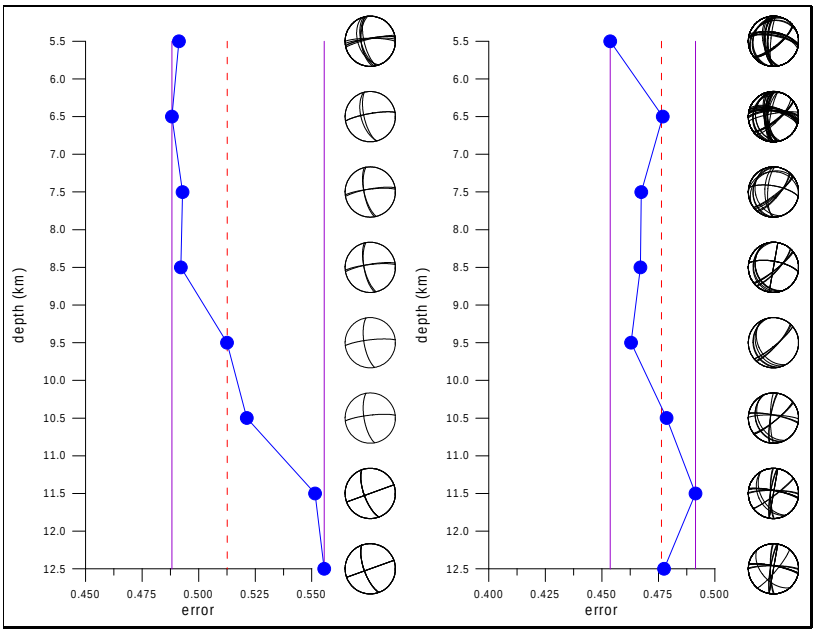

Figure 6.15: Depth plot of $P(\phi_P, \delta_P, \lambda_P)$ & beach balls (2761700 B/22, B/8).

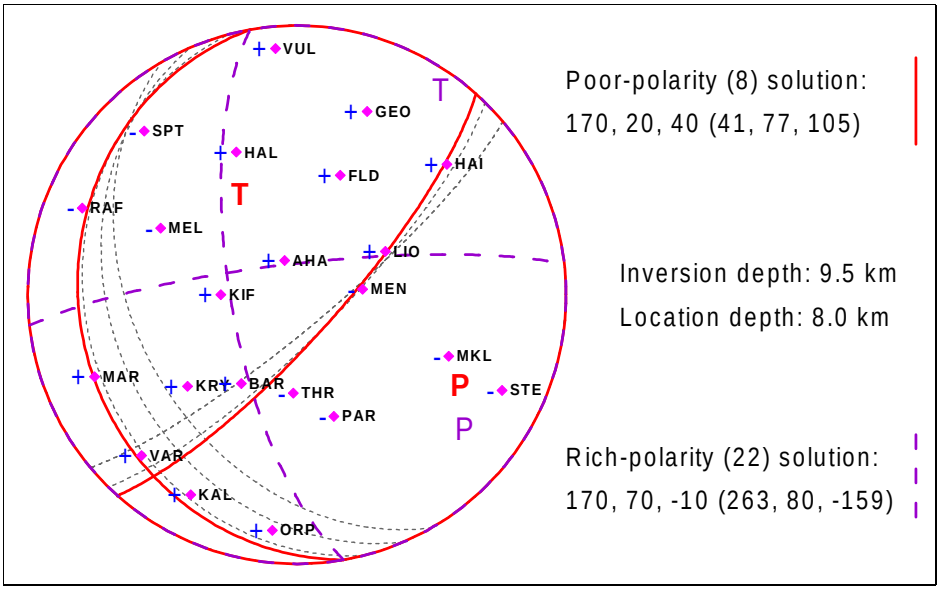

Figure 6.16: Nodal lines of solution at 9.5 km depth (2761700 B/8).

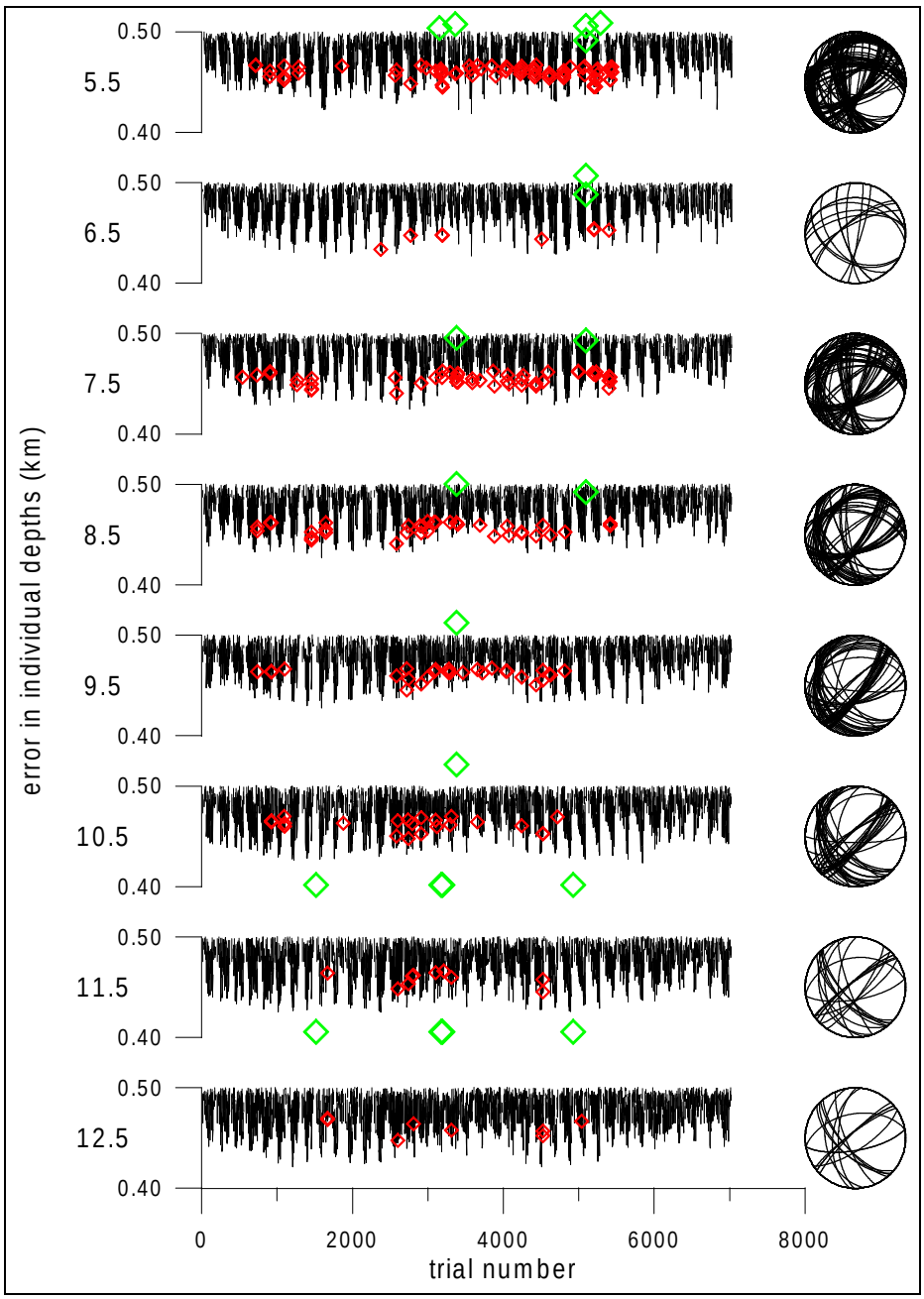

Figure 6.17: Depth plot of E (black), poor-polarity P (red) and rich-polarity P (green), along with poor-polarity beach balls (2761700 B/6).

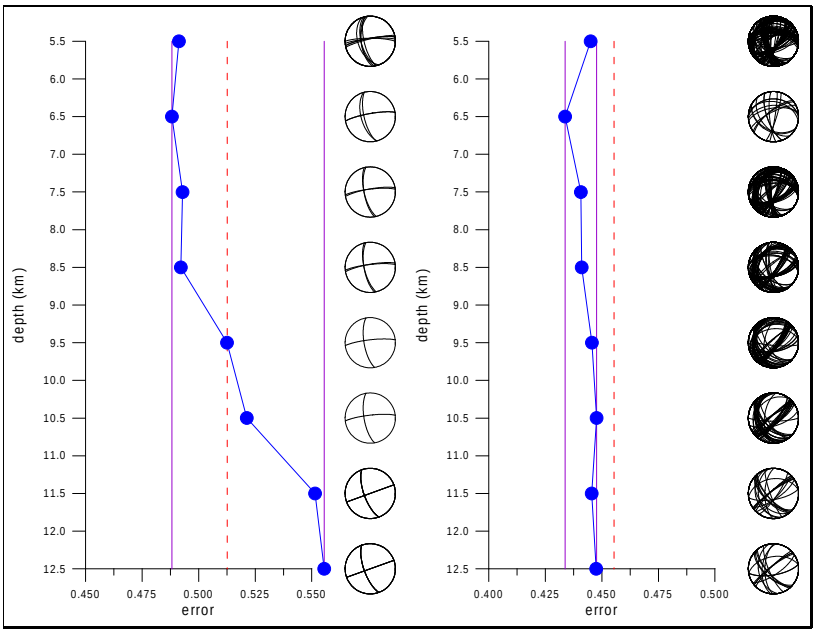

Figure 6.18: Depth plot of $P(\phi_P, \delta_P, \lambda_P)$ & beach balls (2761700 B/22, B/6).

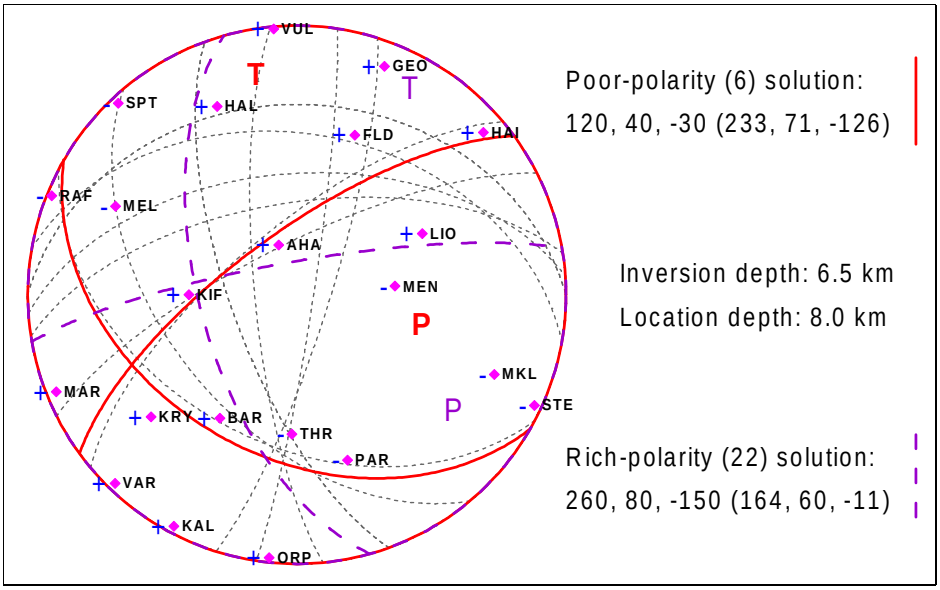

Figure 6.19: Nodal lines of solution at 6.5 km depth (2761700 B/6).

6.2.3 Computation Y/8

This computation employs the amplitude-distribution normalization. Consistency of rich-polarity and poor-polarity solutions is not achieved, still poor--polarity P gets quite low at 8.5 km depth (Figs. 6.20, 6.21). Solution is similar as in computation 2761700 B/8 (Fig. 6.22), $M_0 = 7.9 * 10^{11}$ Nm.

6.2.4 Computation Y/6

The same reasons for polarity testing as in 2761700 B/6 hold here. Nevertheless, we receive almost identical solution to the one in 2761700 Y/8 (Fig. 6.25). The depth plot of $P(\phi_P, \delta_P, \lambda_P)$ is flatter since more inversion triplets are satisfactory (Figs. 6.24, 6.23).

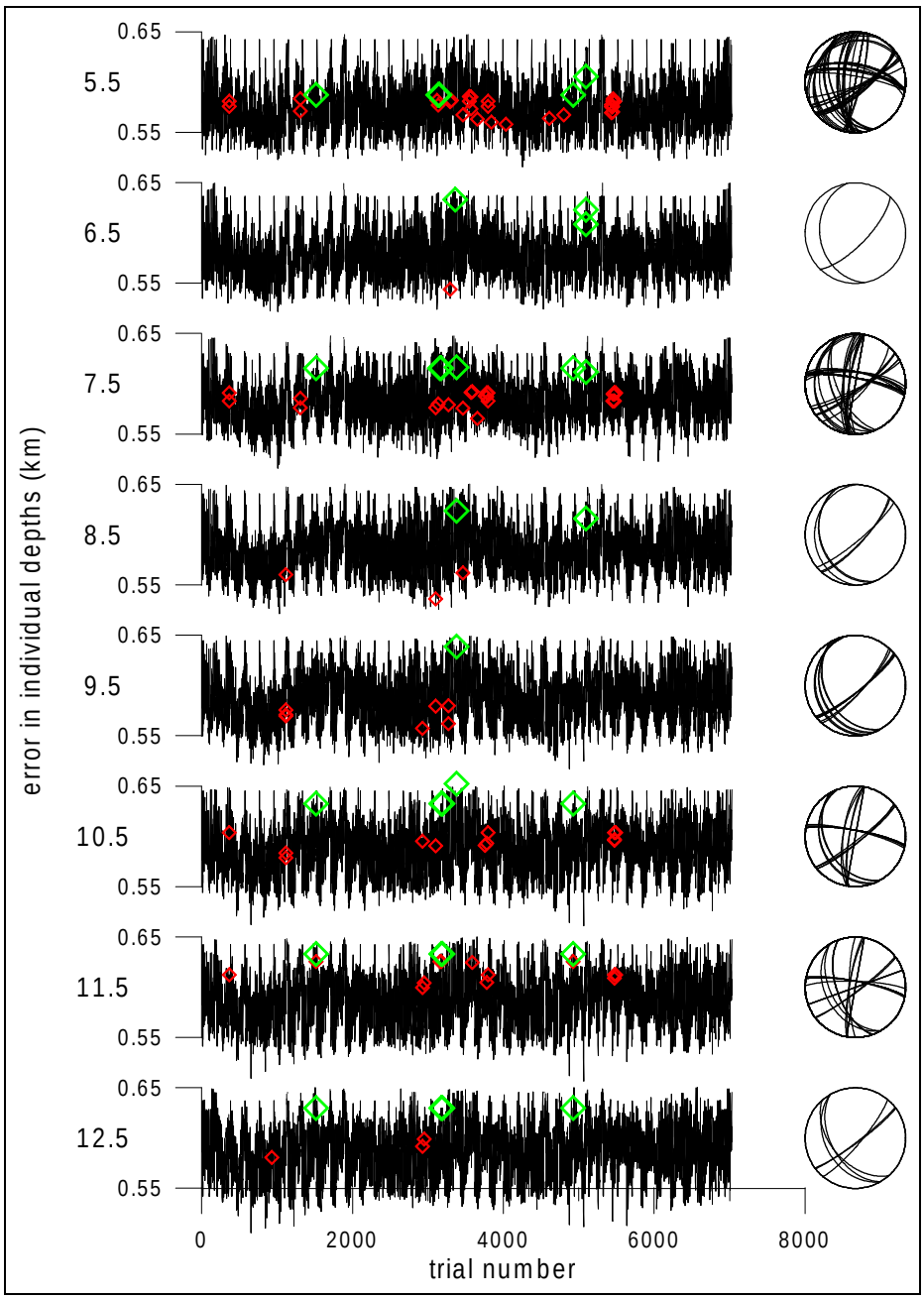

Figure 6.20: Depth plot of E (black), poor-polarity P (red) and rich-polarity P (green), along with poor-polarity beach balls (2761700 Y/8).

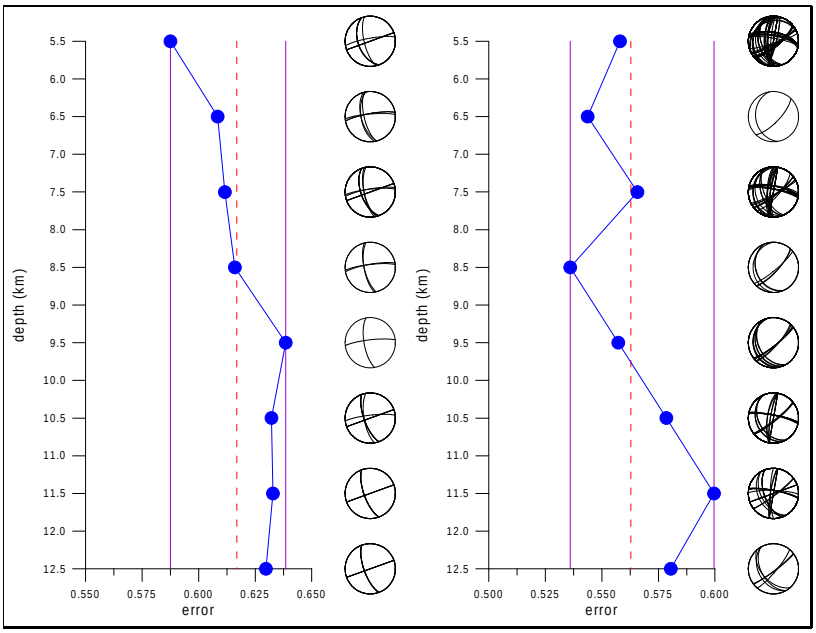

Figure 6.21: Depth plot of $P(\phi_P, \delta_P, \lambda_P)$ & beach balls (2761700 Y/22, Y/8).

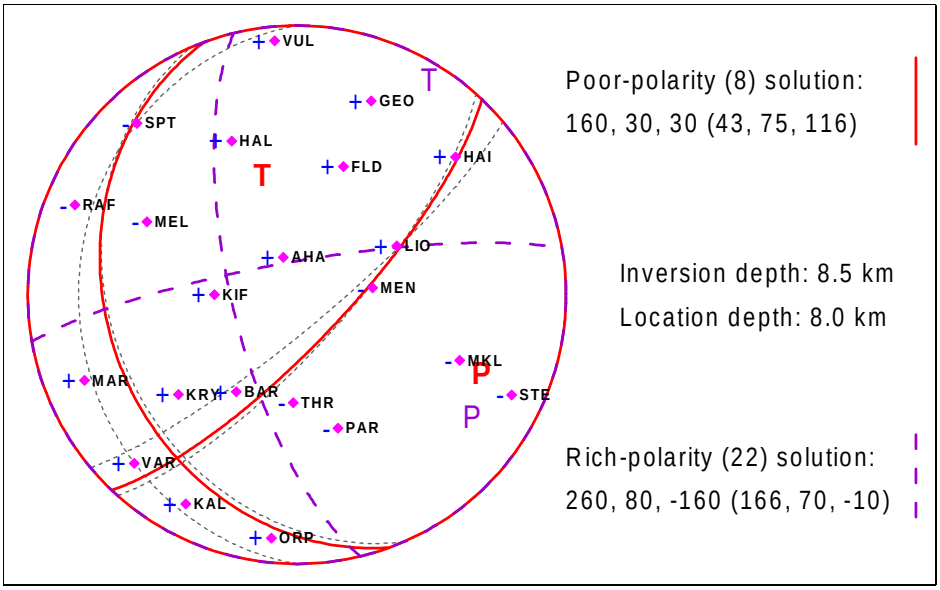

Figure 6.22: Nodal lines of solution at 8.5 km depth (2761700 Y/8).

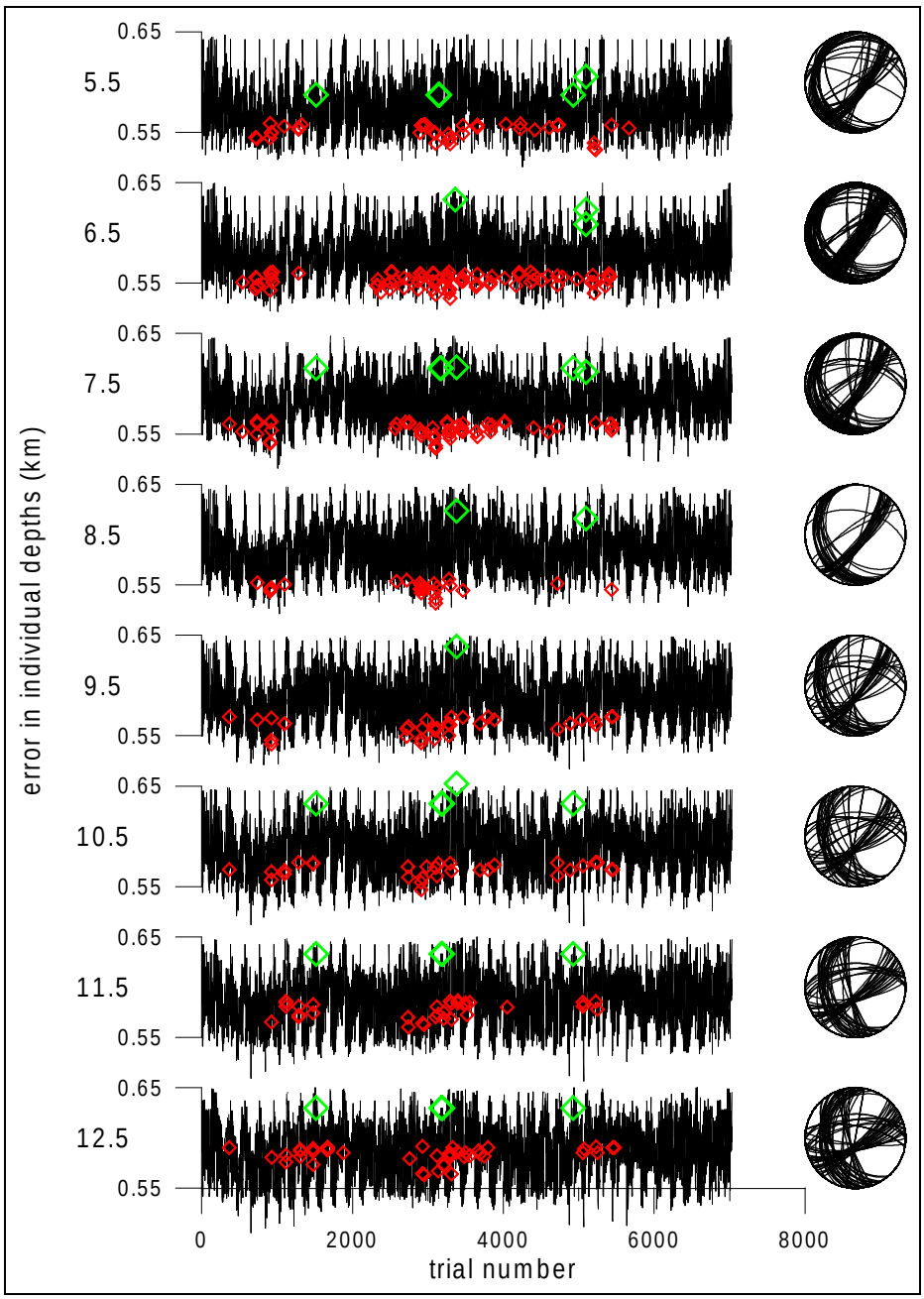

Figure 6.23: Depth plot of E (black), poor-polarity P (red) and rich-polarity P (green), along with poor-polarity beach balls (2761700 Y/6).

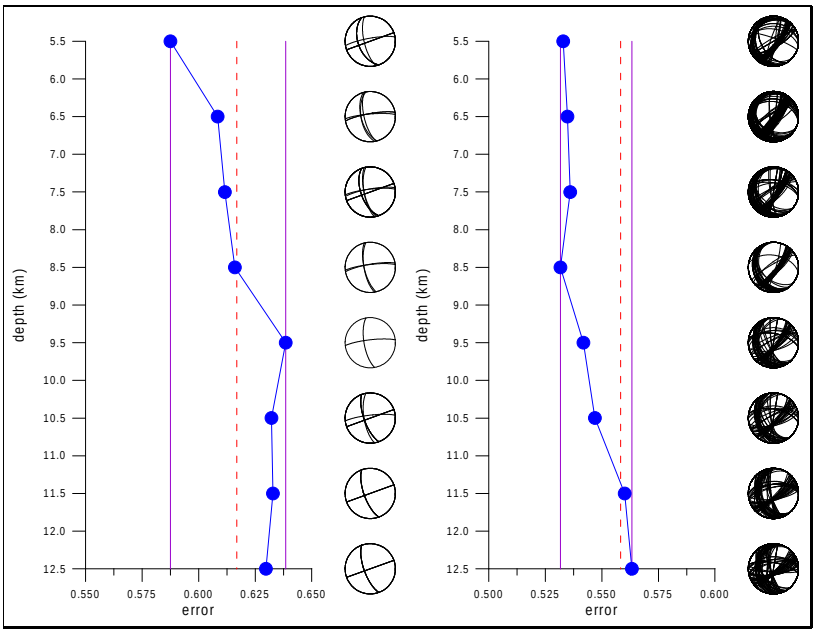

Figure 6.24: Depth plot of $P(\phi_P, \delta_P, \lambda_P)$ & beach balls (2761700 Y/22, Y/6).

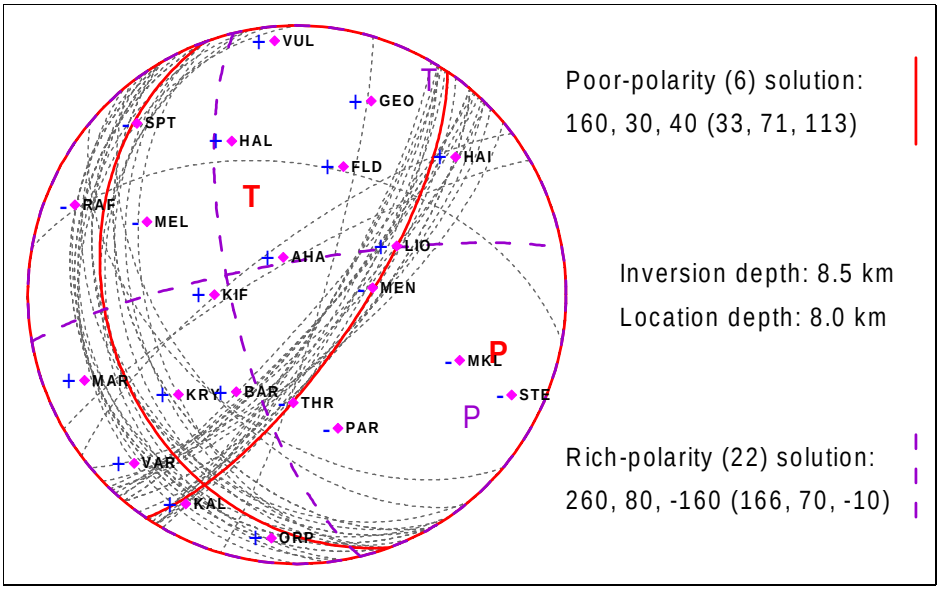

Figure 6.25: Nodal lines of solution at 8.5 km depth (2761700 Y/6).

Chapter 7

Aftershock 2780500

The hypocentre was located in a close vicinity of aftershock 2761700 dealt recently. We shall note that stations from both previous sets combine fairly, which is a favourable incidence (Tab. 7.1, Fig. 7.1). Stations 7, 12, 16, 17, 25 have been used in 2761700 BY, stations 11, 13, 20, 23 in 2761700 AX, station 30 is new. Poor-polarity subset was obtained by intersection of all available check-points with the inversion station set (Tab. 7.2).

7.0.5 Computation A/6

Both the error graph and the depth plot of $P(\phi_P, \delta_P, \lambda_P)$ (Figs. 7.2, 7.3) agree on solution at 7.5 km depth (Fig. 7.4) where poor-polarity P occurs in the marked minimum of E. Moment is $M_0 = 4.3 * 10^9$ Nm.

The depth plot 2780500 A/6 still features another minimum at 11.5 km depth. Respecting the condition of rich-polarity solution existence, this candidate cannot be accepted. The functions E and P are not satisfactory anyway. In spite of all this, we show the trim beach ball as a warning (Fig. 7.5), $M_0 = 4.5 * 10^9$ Nm. Note that check-points KRY and STE are also matched.

7.0.6 Computation X/6

Results for the former normalization are remarkable for the fact that rich--polarity and poor-polarity solutions do intersect in some depths (Fig. 7.6), unlike computation A/6. That is the point why we prefer solution at 5.5 km depth (Fig. 7.8) to solution at 6.5 km suggested by the poor-polarity depth plot of $P(\phi_P, \delta_P, \lambda_P)$ (Fig. 7.7). At 5.5 km depth, $M_0 = 3.3 * 10^9$ Nm.

Id	Code	Lat N (deg)	Lon E (deg)	Azimuth (deg)	Distance (km)
7	MAG	38.073	23.533	263.80	19.36
11	BAR	38.135	23.791	34.80	5.82
12	THR	38.139	23.761	7.61	5.27
13	PAR	38.153	23.737	348.33	6.92
16	RAF	38.018	23.995	111.16	22.71
17	KIF	38.096	23.799	83.71	4.04
20	SPT	37.965	23.912	135.36	19.82
23	KAL	38.262	23.873	28.99	21.60
25	MEN	38.094	23.724	274.96	2.55
30	FLP	37.970	23.720	192.04	13.86

Table 7.1: Stations engaged in the inversion (2780500 AX).

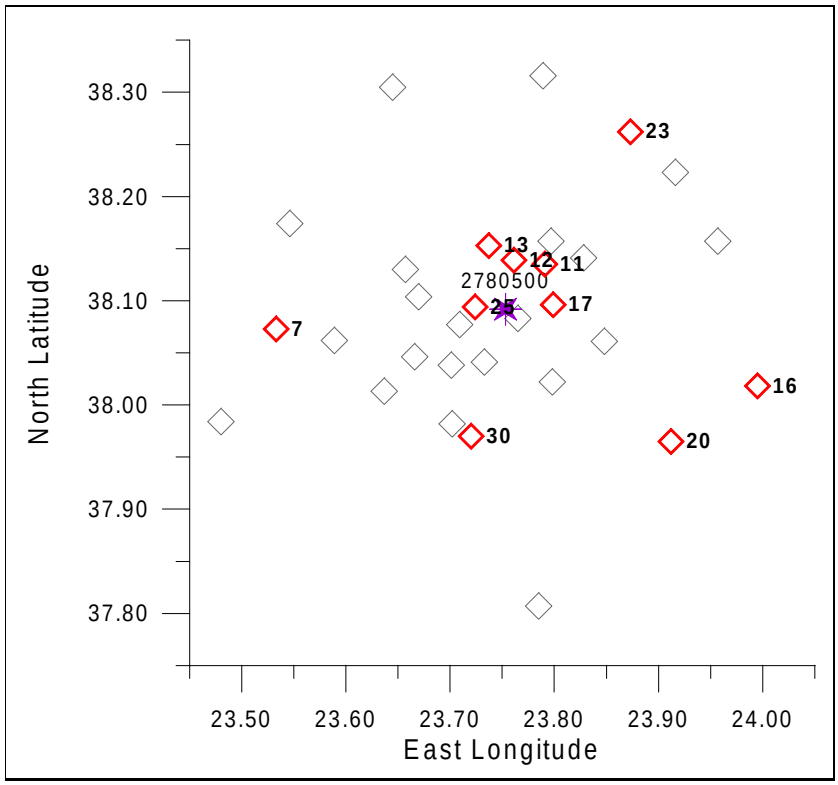

Figure 7.1: Aftershock epicentre & deployment of the stations (2780500 AX).

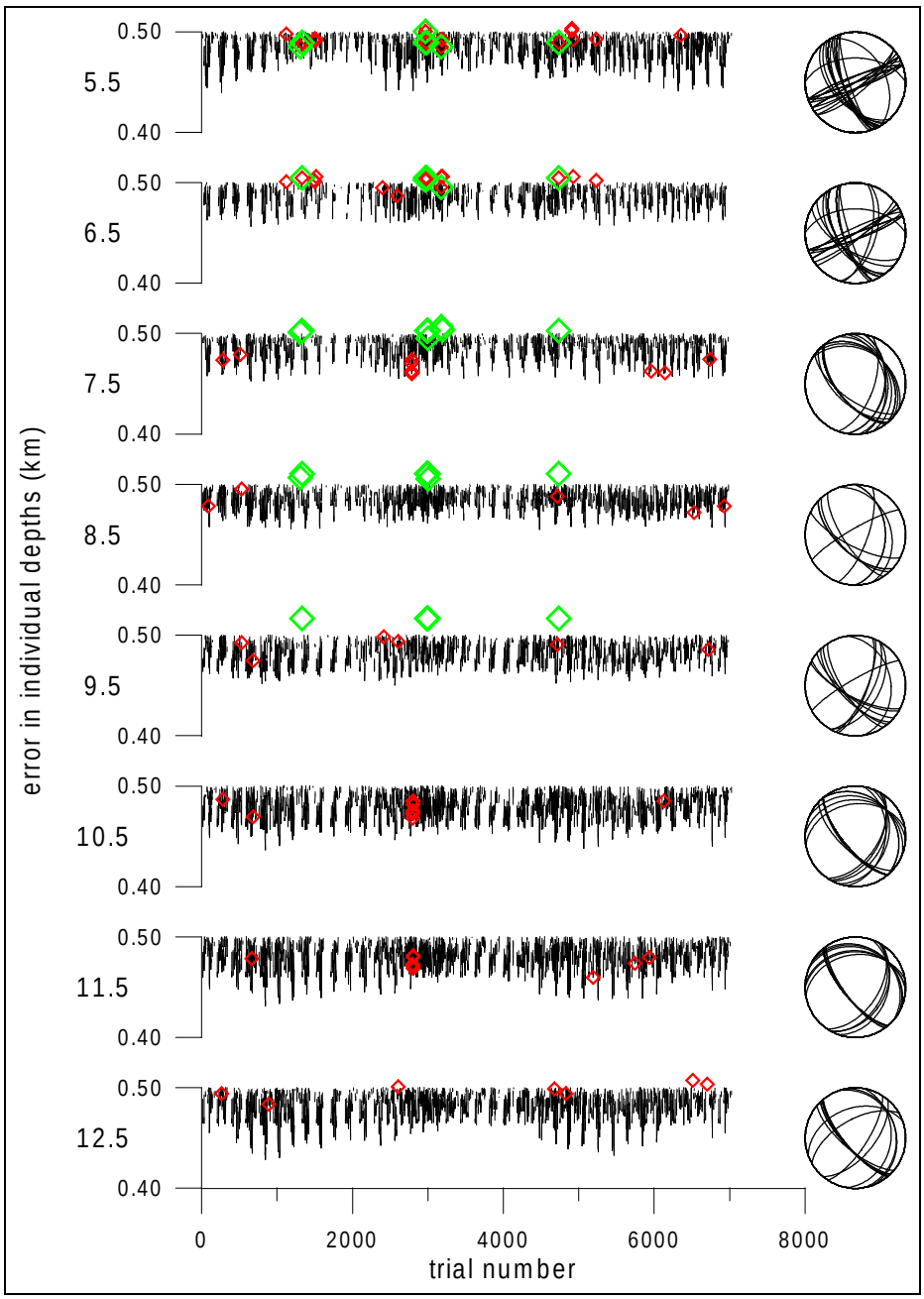

Figure 7.2: Depth plot of E (black), poor-polarity P (red) and rich-polarity P (green), along with poor-polarity beach balls (2780500 A/6).

Code	Azim (deg)	Take-off Angles (deg)								Sign
BAR	34	130	131	136	141	145	148	150	153	U
THR	7	133	134	140	144	148	150	153	155	U
PAR	348	125	124	131	136	140	143	146	148	D
KIF	83	141	142	147	151	154	157	159	160	D
KAL	28	102	93	98	102	106	109	112	115	U
MEN	274	153	155	158	161	163	165	166	167	D
PET	236	117	114	121	127	131	135	138	140	U
KRY	50	119	117	124	129	133	137	140	143	U
MEL	112	118	115	122	127	132	135	138	141	D
AHA	133	164	165	167	169	170	171	172	172	U
MAR	67	103	93	100	105	109	112	115	118	D
STE	296	103	93	99	104	108	111	114	117	D

Table 7.2: Stations providing polarity data & take-off angles of the first--arrival rays (depth increasing to the right, see depth plots) (2780500 AX).

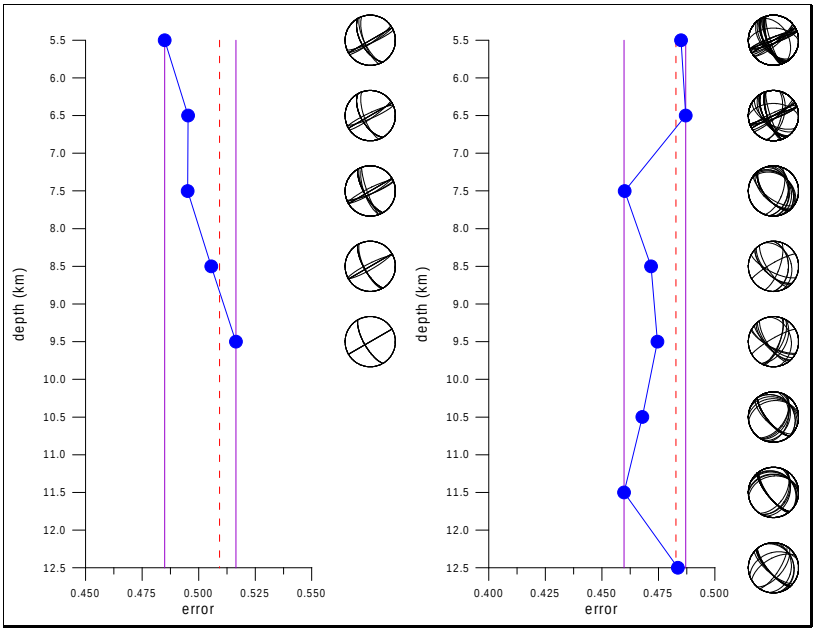

Figure 7.3: Depth plot of $P(\phi_P, \delta_P, \lambda_P)$ & beach balls (2780500 A/12, A/6).

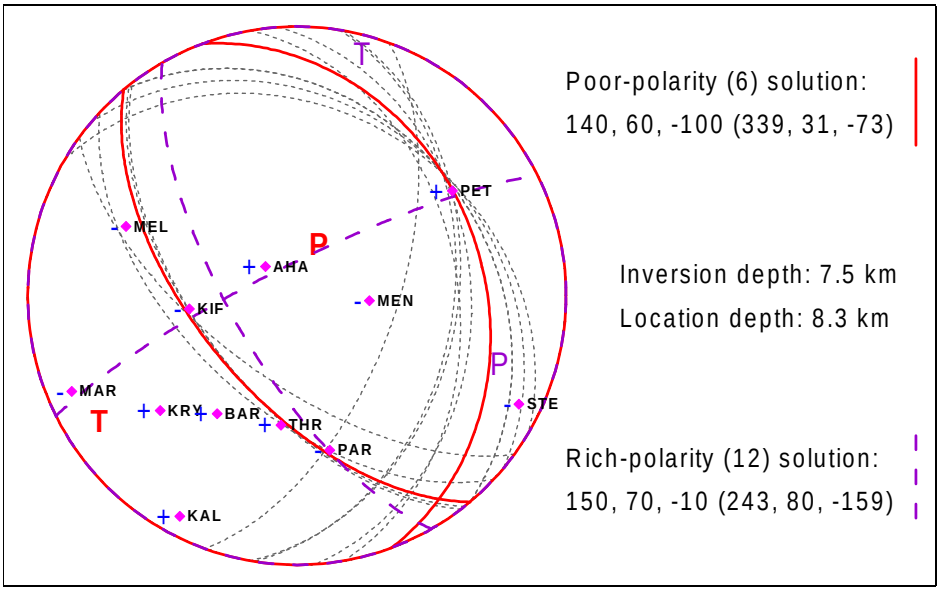

Figure 7.4: Nodal lines of solution at 7.5 km depth (2780500 A/6).

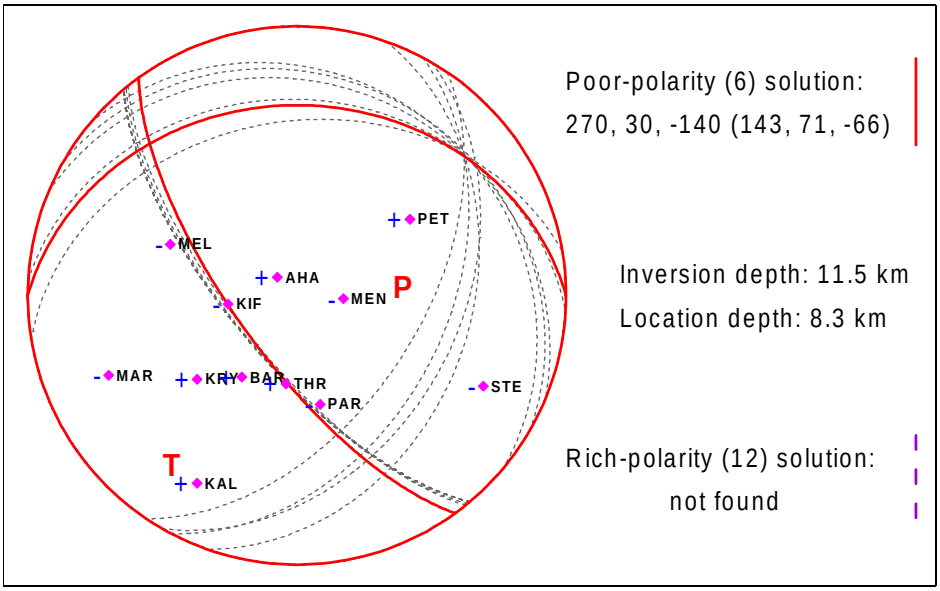

Figure 7.5: Seeming but invalid solution at 11.5 km depth (2780500 A/6).

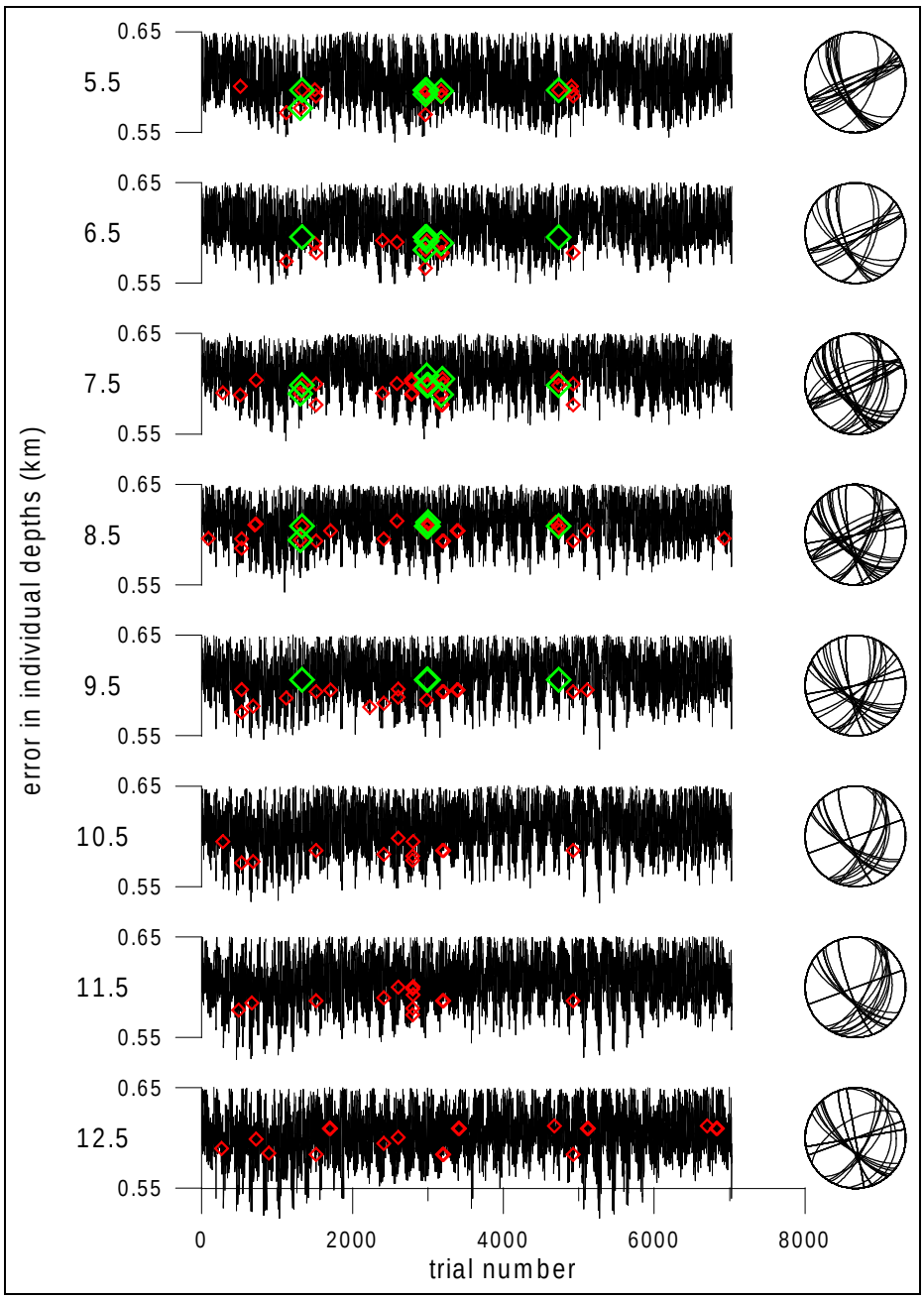

Figure 7.6: Depth plot of E (black), poor-polarity P (red) and rich-polarity P (green), along with poor-polarity beach balls (2780500 X/6).

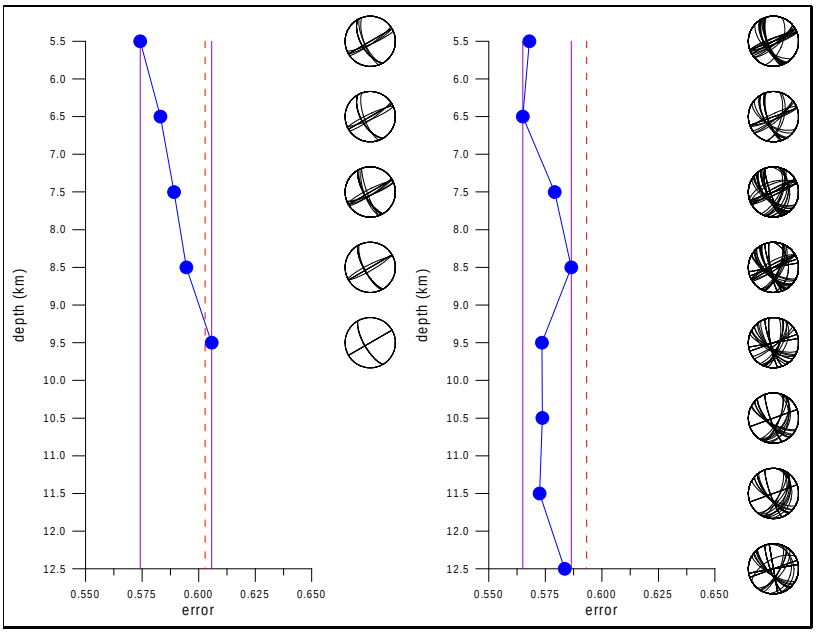

Figure 7.7: Depth plot of $P(\phi_P, \delta_P, \lambda_P)$ & beach balls (2780500 X/12, X/6).

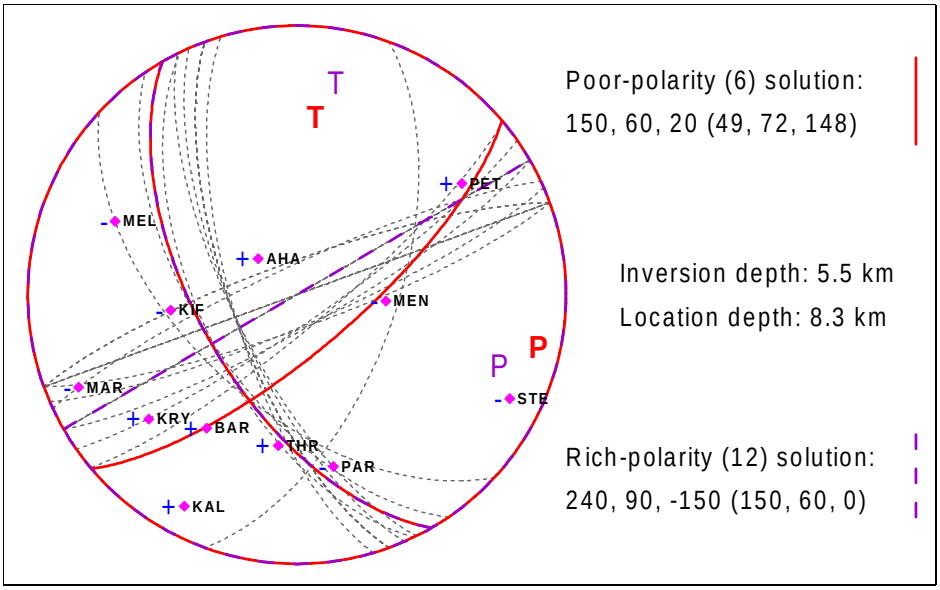

Figure 7.8: Nodal lines of solution at 5.5 km depth (2780500 X/6).

Chapter 8

Aftershock 2601730

This aftershock was inverted from two disjunct station sets, too, however there is no special relation to the sets of aftershock 2761700.

8.1 First station set

Deployment of stations is depicted in Tab. 8.1 and Fig. 8.8. Rich-polarity and poor-polarity sets contain 24 and 9 check-points respectively, the subset being derived by intersection (Tab. 8.2).

8.1.1 Computation A/9

The results (Figs. 8.2, 8.3) satisfy all requirements declared on page 31 and solution at 13.0 km depth is agreed on well (Fig. 8.4). Seismic moment is $M_0 = 6.0 * 10^{11}$ Nm.

8.1.2 Computation X/9

The amplitude-distribution normalization yields such an error function that its minima do not satisfy polarity test (Fig. 8.5). Rich-polarity and poor--polarity solutions overlap. According to Fig. 8.6, solution at 12.0 km depth is displayed (Fig. 8.7), $M_0 = 6.8 * 10^{11}$ Nm.

Id	Code	Lat N (deg)	Lon E (deg)	Azimuth (deg)	Distance (km)
1	GEO	37.982	23.702	165.93	10.08
3	PET	38.046	23.666	194.73	2.76
7	MAG	38.073	23.533	271.58	12.34
9	KRY	38.141	23.828	59.59	15.60
12	THR	38.139	23.761	44.75	10.80
16	RAF	38.018	23.995	101.53	28.67
20	SPT	37.965	23.912	119.18	23.88
22	VAR	38.223	23.916	51.13	27.13
25	MEN	38.094	23.724	58.62	5.12
27	STE	38.174	23.546	315.95	16.08

Table 8.1: Stations engaged in the inversion (2601730 AX).

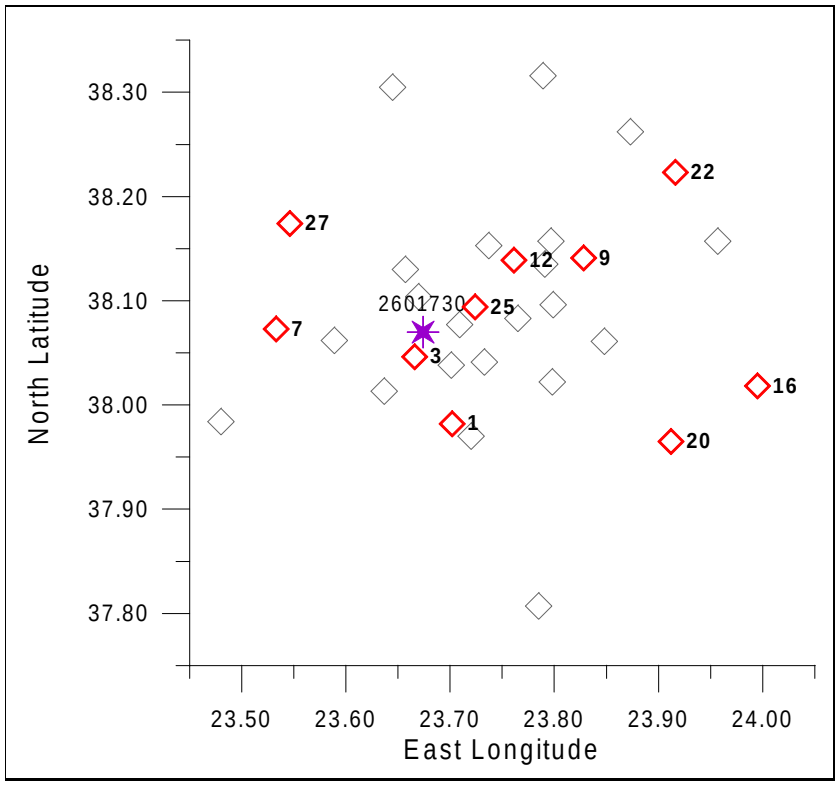

Figure 8.1: Aftershock epicentre & deployment of the stations (2601730 AX).

Code	Azim (deg)	Take-off Angles (deg)								Sign
PET	194	155	158	161	163	164	166	167	168	D
MAG	271	108	115	119	123	127	130	133	135	D
KRY	59	101	108	112	116	120	123	126	128	U
THR	44	113	119	124	128	131	134	137	139	U
RAF	101	93	96	99	102	105	107	109	111	U
SPT	119	94	99	102	106	108	111	114	116	D
VAR	51	93	97	100	103	106	108	111	113	U
MEN	58	138	143	147	150	152	155	156	158	D
STE	315	101	107	112	115	119	122	125	127	D
NLI	146	143	148	151	154	156	158	160	161	D
LIO	75	152	155	158	160	162	164	165	166	D
FLD	121	132	137	142	145	148	150	153	154	D
BAR	54	108	114	119	123	126	130	132	135	U
PAR	30	113	119	124	128	131	134	137	139	U
MEL	93	102	108	113	117	120	124	126	129	U
KIF	75	111	117	122	126	130	133	136	138	U
AHA	79	122	128	133	137	140	143	145	147	U
HAL	116	109	115	120	124	128	131	133	136	D
MAR	68	93	97	100	103	106	109	111	113	U
KAL	39	93	97	100	103	105	108	110	112	U
ORP	20	93	96	99	102	104	107	109	111	U
ASP	263	125	131	135	139	142	145	147	149	D
HAI	207	127	132	137	141	144	146	149	151	D
VUL	161	93	96	98	101	103	106	108	110	U

Table 8.2: Stations providing polarity data & take-off angles of the first--arrival rays (depth increasing to the right, see depth plots) (2601730 AX).

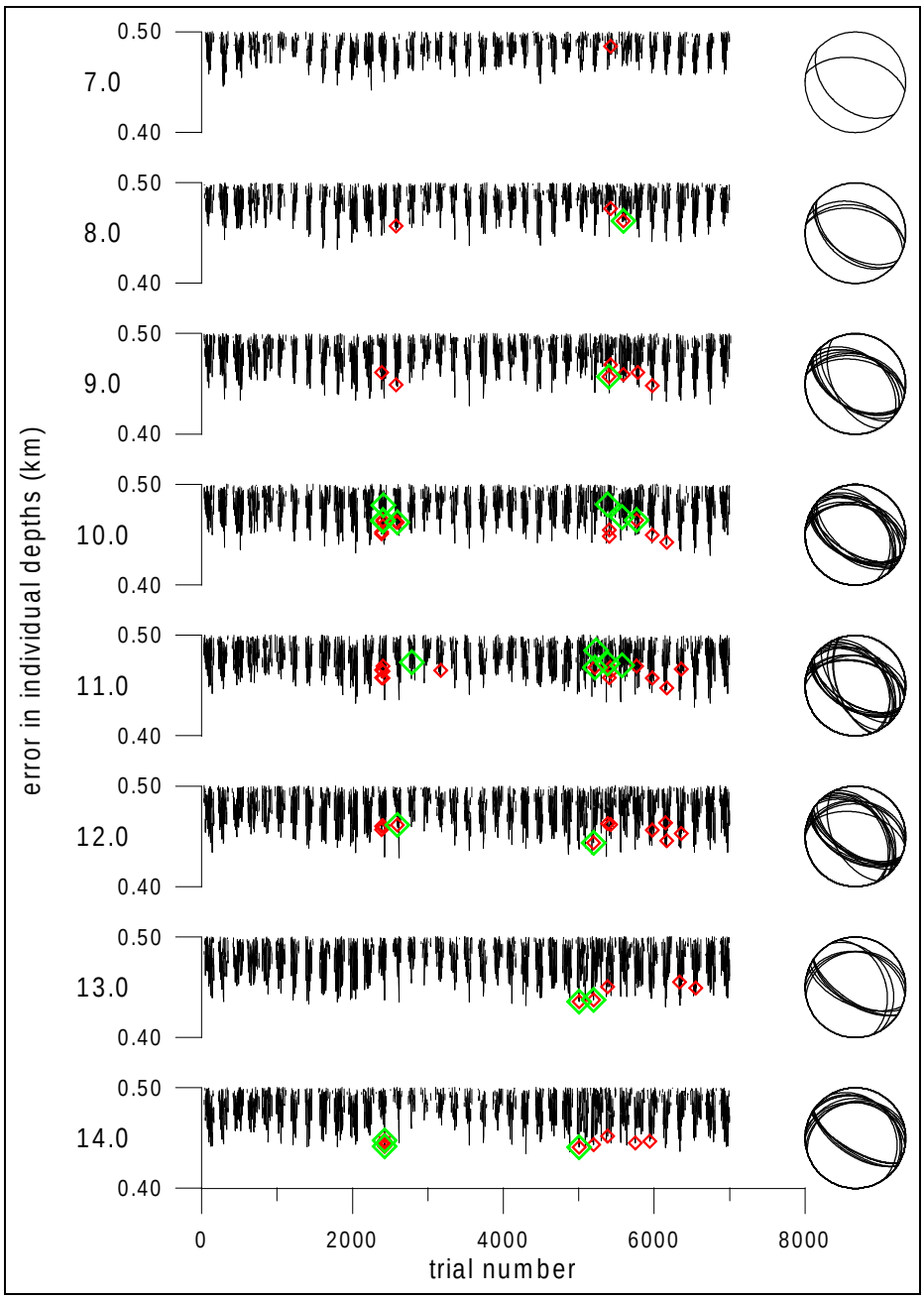

Figure 8.2: Depth plot of E (black), poor-polarity P (red) and rich-polarity P (green), along with poor-polarity beach balls (2601730 A/9).

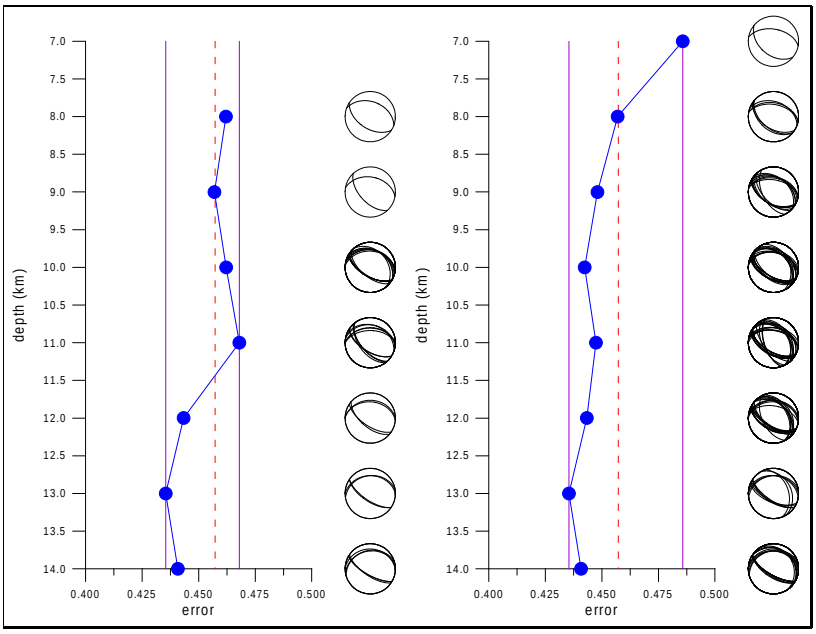

Figure 8.3: Depth plot of $P(\phi_P, \delta_P, \lambda_P)$ & beach balls (2601730 A/24, A/9).

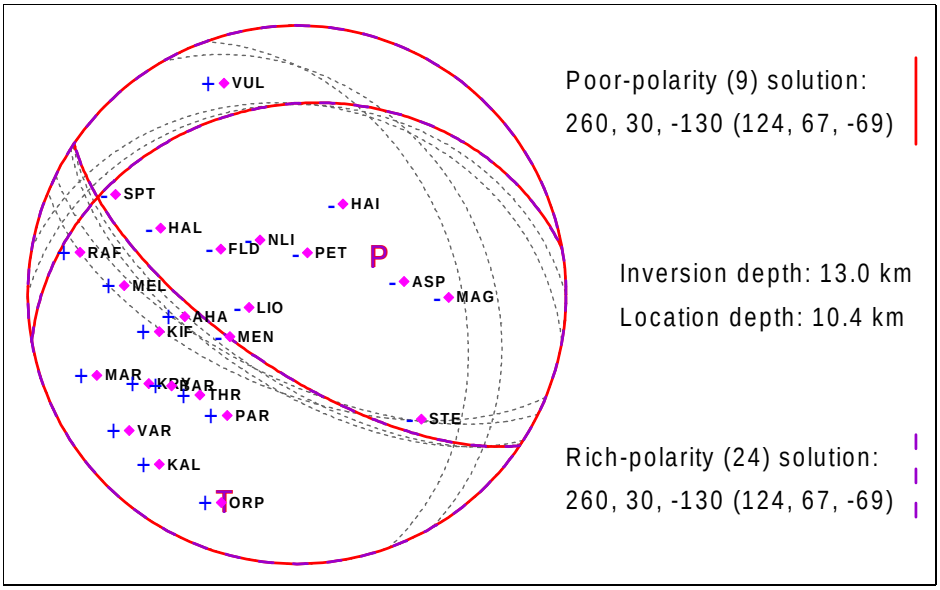

Figure 8.4: Nodal lines of solution at 13.0 km depth (2601730 A/9).

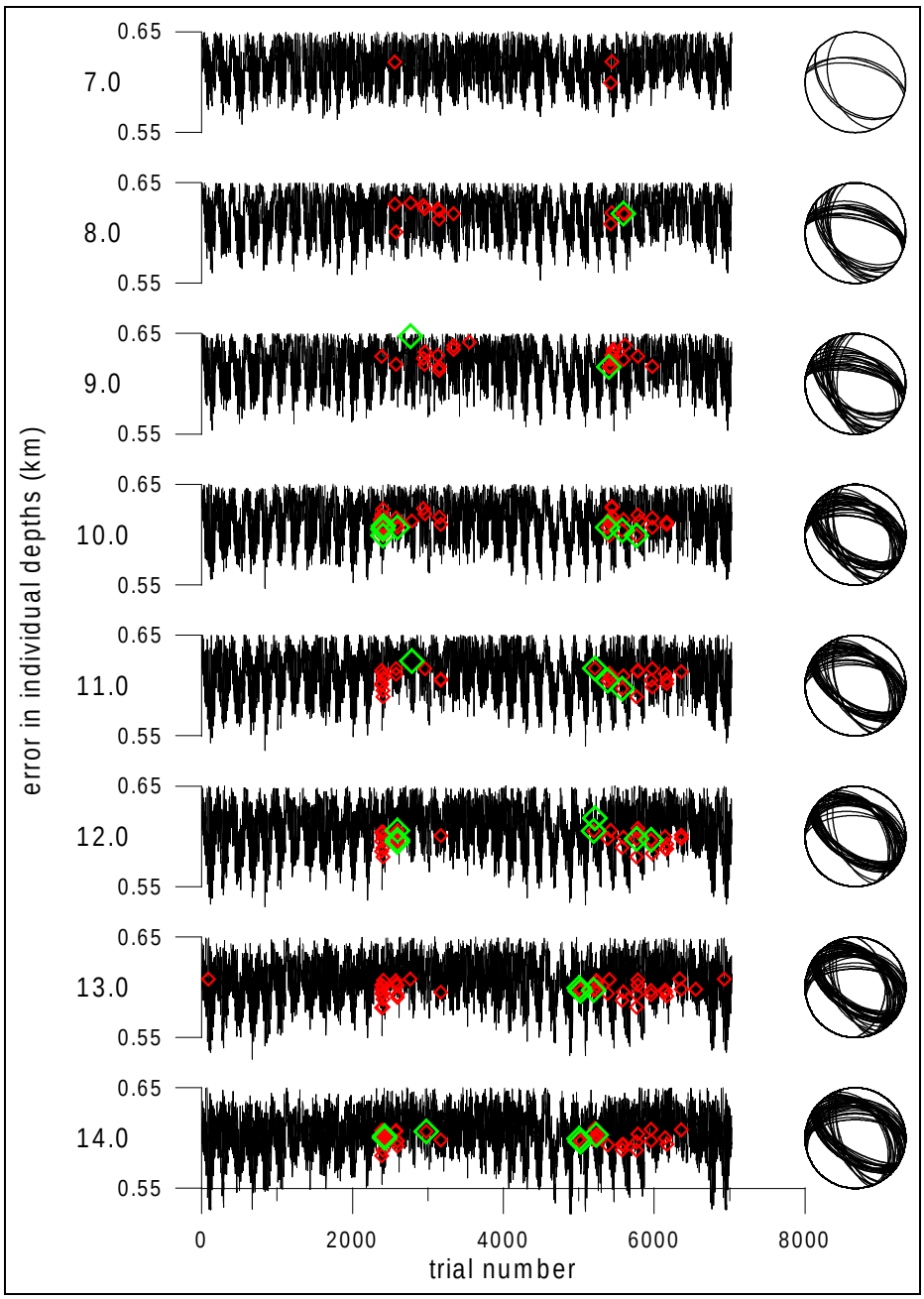

Figure 8.5: Depth plot of E (black), poor-polarity P (red) and rich-polarity P (green), along with poor-polarity beach balls (2601730 X/9).

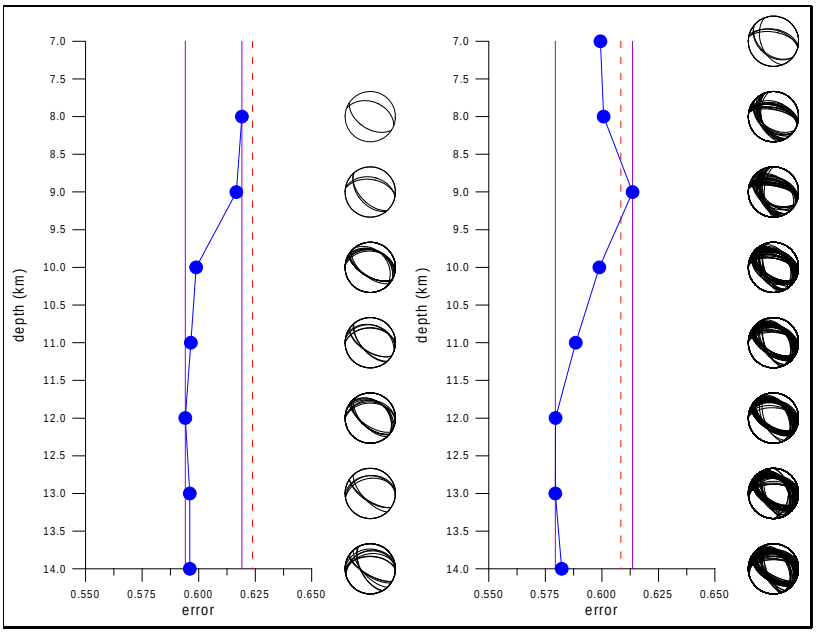

Figure 8.6: Depth plot of $P(\phi_P, \delta_P, \lambda_P)$ & beach balls (2601730 X/24, X/9).

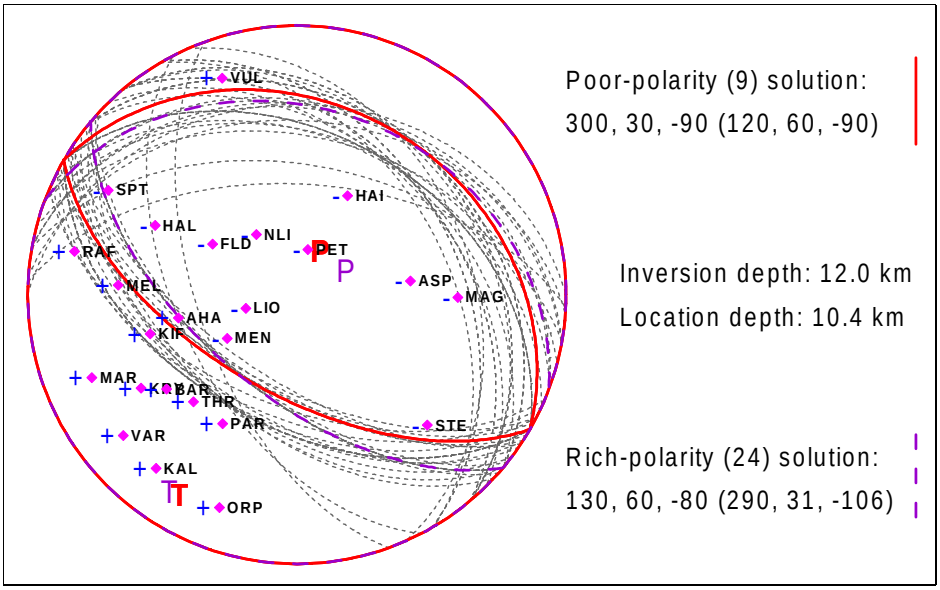

Figure 8.7: Nodal lines of solution at 12.0 km depth (2601730 X/9).

8.2 Second station set

Deployment of stations is depicted in Tab. 8.3 and Fig. 8.8. Rich-polarity and poor-polarity sets contain 24 and 9 check-points respectively, the subset being derived by intersection (Tab. 8.4).

8.2.1 Computation B/9

The error function E is very flat at the suggested depth of 11.0 km (Figs. 8.9, 8.10), resulting in a broad range of solutions. Nearby them, rich-polarity solutions are found (Fig. 8.11), $M_0 = 2.9 * 10^{11}$ Nm.

Solution at 8.0 km depth is refused because the minimum of $P(\phi_P, \delta_P, \lambda_P)$ is not present for both check-point sets.

8.2.2 Computation Y/9

The error function features many unoccupied singular minima (Fig. 8.12) and the depth plot of $P(\phi_P, \delta_P, \lambda_P)$ has the global minimum at the border of the range (Fig. 8.13), which are both unfavourable facts.

If beach ball trimness is preferred to agreement of rich-polarity and poor--polarity solutions, depth of 11.0 km comes into question (Fig. 8.14) implying $M_0 = 4.2 * 10^{11}$ Nm. If taking the same view as in computation B/9, solution at 14.0 km depth is to show (Fig. 8.15), $M_0 = 7.5 * 10^{11}$ Nm.

Id	Code	Lat N (deg)	Lon E (deg)	Azimuth (deg)	Distance (km)
2	NLI	38.038	23.701	146.43	4.27
4	LIO	38.077	23.709	75.77	3.16
8	FLD	38.041	23.733	121.98	6.08
11	BAR	38.135	23.791	54.75	12.52
13	PAR	38.153	23.737	30.83	10.74
17	KIF	38.096	23.799	75.17	11.30
21	MAR	38.157	23.957	68.57	26.56
23	KAL	38.262	23.873	39.12	27.51
26	ASP	38.062	23.589	263.19	7.49
30	FLP	37.970	23.720	160.08	11.82

Table 8.3: Stations engaged in the inversion (2601730 BY).

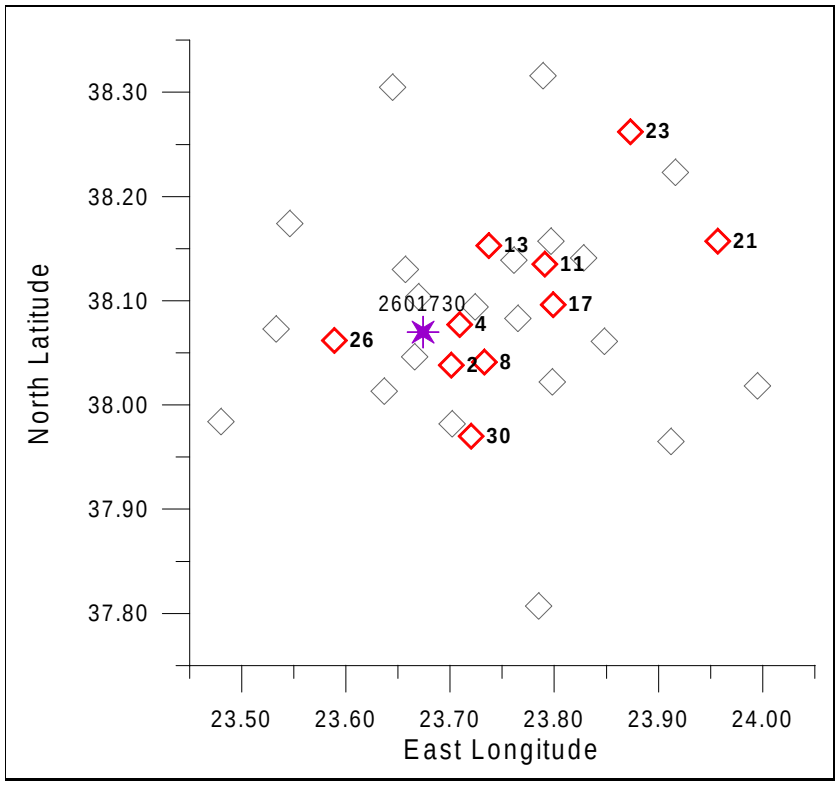

Figure 8.8: Aftershock epicentre & deployment of the stations (2601730 BY).

Code	Azim (deg)	Take-off Angles (deg)								Sign
NLI	146	143	148	151	154	156	158	160	161	D
LIO	75	152	155	158	160	162	164	165	166	D
FLD	121	132	137	142	145	148	150	153	154	D
BAR	54	108	114	119	123	126	130	132	135	U
PAR	30	113	119	124	128	131	134	137	139	U
KIF	75	111	117	122	126	130	133	136	138	U
MAR	68	93	97	100	103	106	109	111	113	U
KAL	39	93	97	100	103	105	108	110	112	U
ASP	263	125	131	135	139	142	145	147	149	D
PET	194	155	158	161	163	164	166	167	168	D
MAG	271	108	115	119	123	127	130	133	135	D
KRY	59	101	108	112	116	120	123	126	128	U
THR	44	113	119	124	128	131	134	137	139	U
MEL	93	102	108	113	117	120	124	126	129	U
RAF	101	93	96	99	102	105	107	109	111	U
AHA	79	122	128	133	137	140	143	145	147	U
HAL	116	109	115	120	124	128	131	133	136	D
SPT	119	94	99	102	106	108	111	114	116	D
VAR	51	93	97	100	103	106	108	111	113	U
ORP	20	93	96	99	102	104	107	109	111	U
MEN	58	138	143	147	150	152	155	156	158	D
STE	315	101	107	112	115	119	122	125	127	D
HAI	207	127	132	137	141	144	146	149	151	D
VUL	161	93	96	98	101	103	106	108	110	U

Table 8.4: Stations providing polarity data & take-off angles of the first--arrival rays (depth increasing to the right, see depth plots) (2601730 BY).

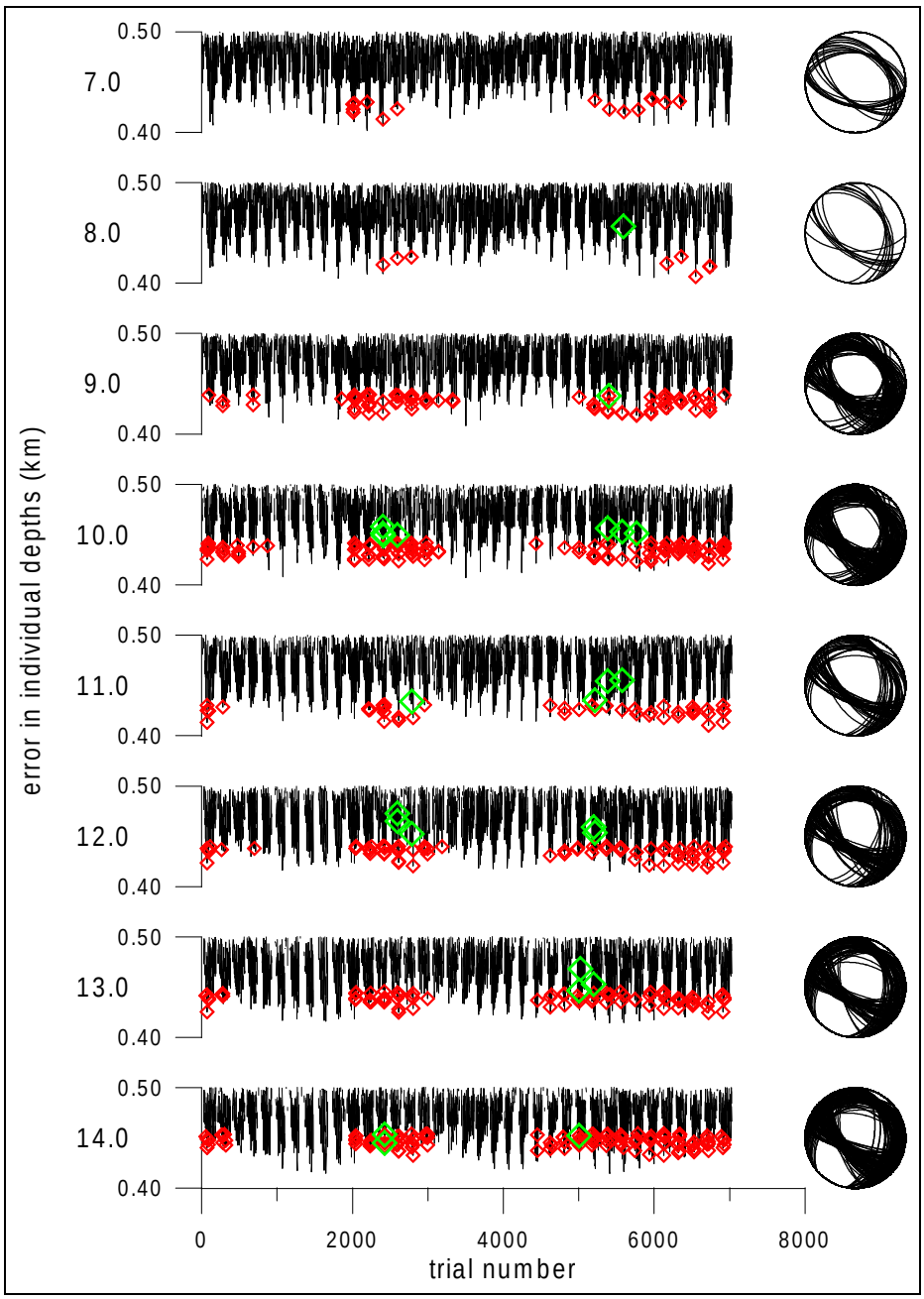

Figure 8.9: Depth plot of E (black), poor-polarity P (red) and rich-polarity P (green), along with poor-polarity beach balls (2601730 B/9).

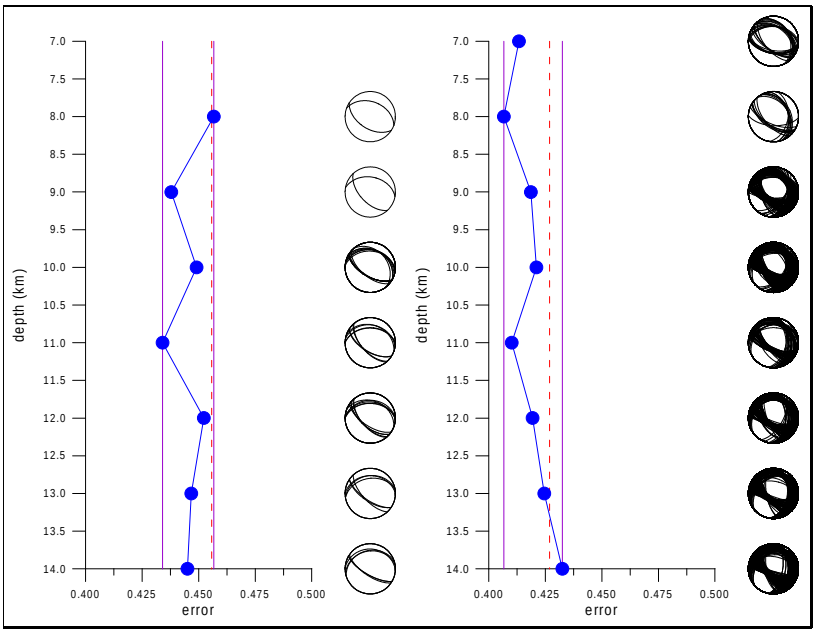

Figure 8.10: Depth plot of $P(\phi_P, \delta_P, \lambda_P)$ & beach balls (2601730 B/24, B/9).

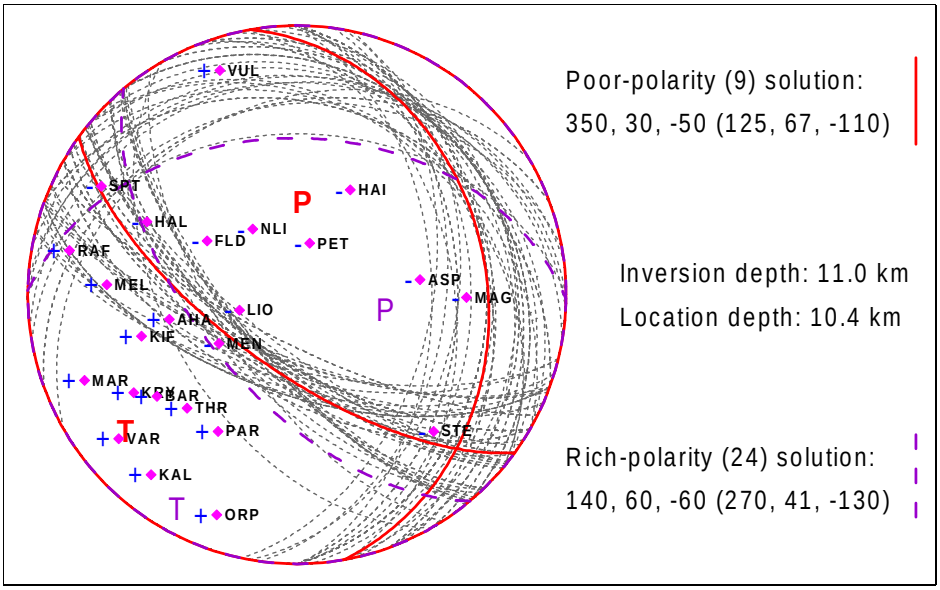

Figure 8.11: Nodal lines of solution at 11.0 km depth (2601730 B/9).

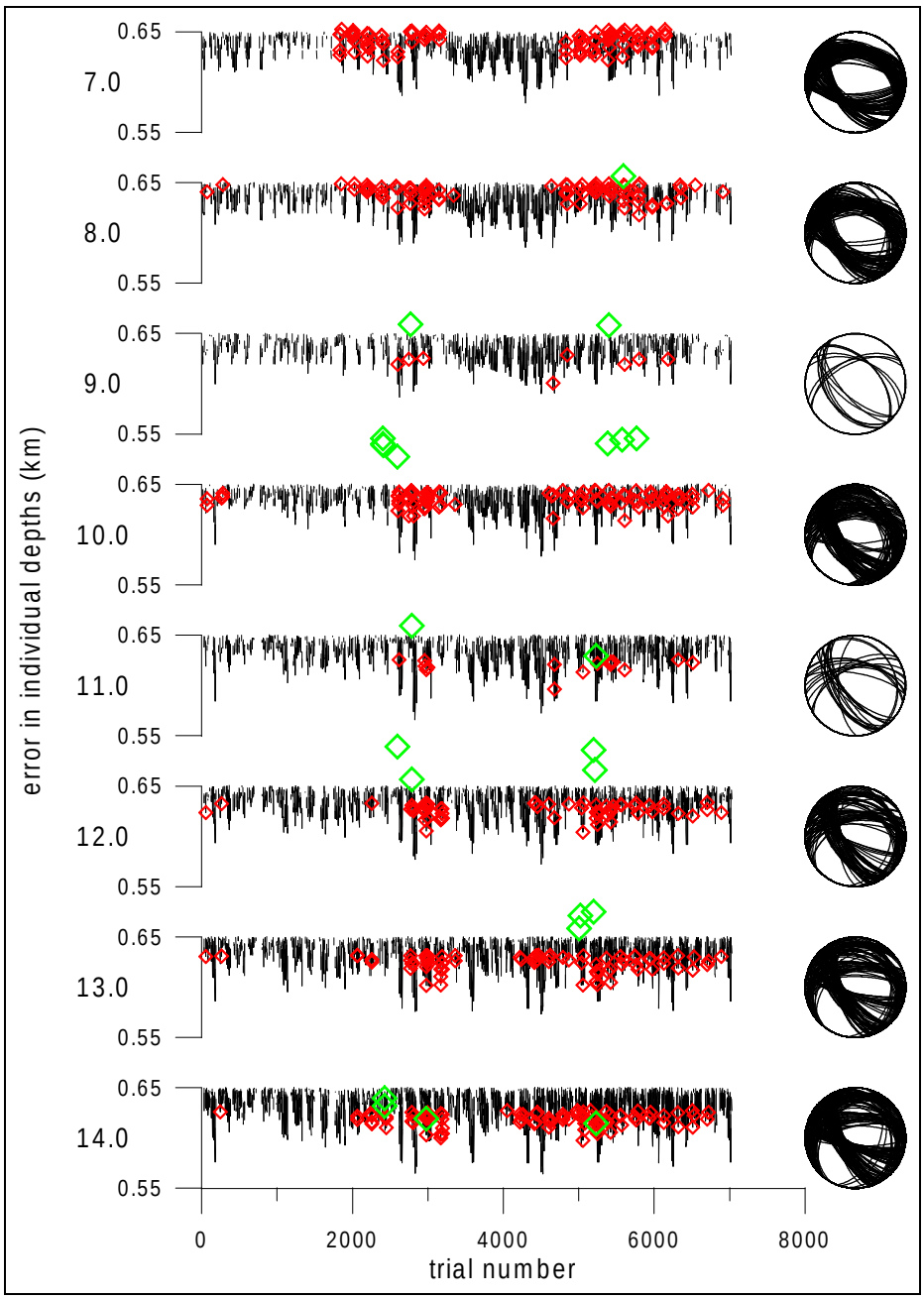

Figure 8.12: Depth plot of E (black), poor-polarity P (red) and rich-polarity P (green), along with poor-polarity beach balls (2601730 Y/9).

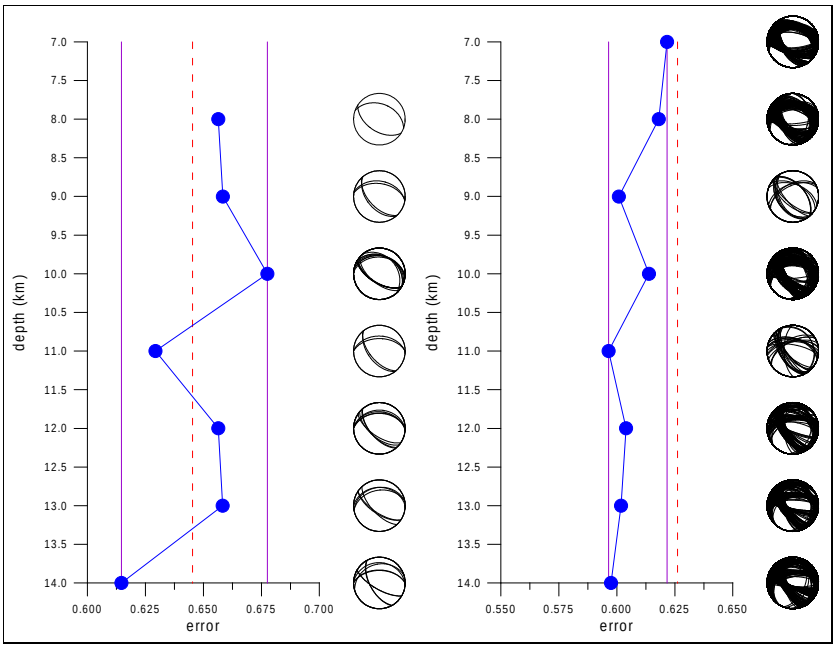

Figure 8.13: Depth plot of $P(\phi_P, \delta_P, \lambda_P)$ & beach balls (2601730 Y/24, Y/9).

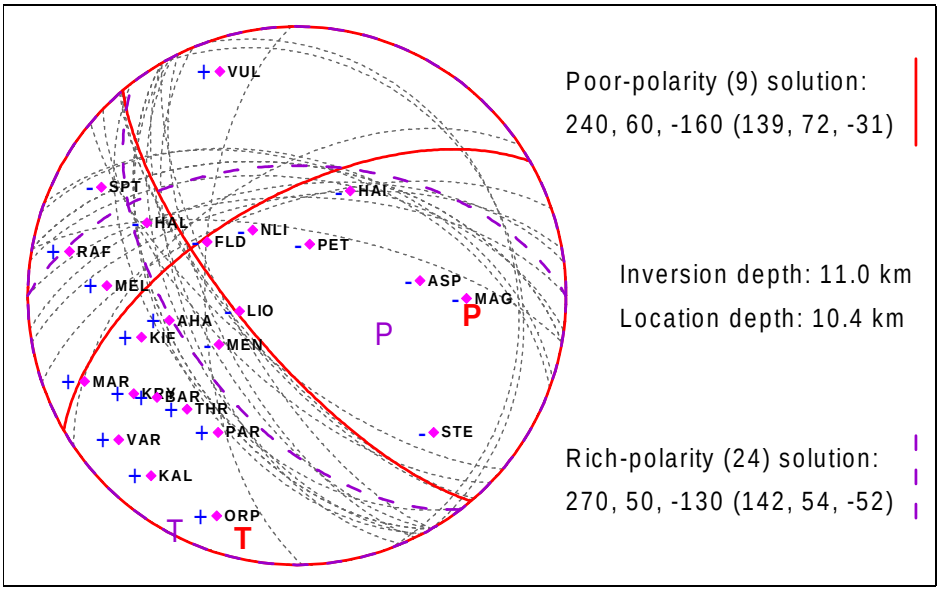

Figure 8.14: Nodal lines of solution at 11.0 km depth (2601730 Y/9).

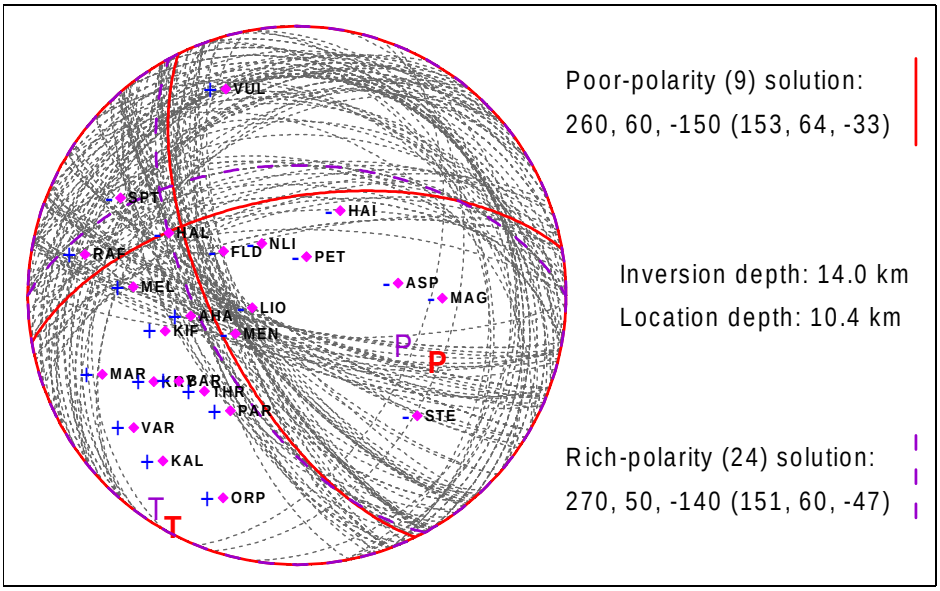

Figure 8.15: Nodal lines of solution at 14.0 km depth (2601730 Y/9).

Chapter 9

Discussion of the Results

According to [6], the inverted aftershocks seem to form two groups of different nature. Aftershocks 2601730 and 2671010 can be distinguished from aftershocks 2761700 and 2780500, considering their temporal and spatial occurrence as well as focal mechanisms based on pure polarity solutions.

These events served well for the purpose of our work and their separation was confirmed. Results for the first group are more satisfactory than for the other one. Perhaps, this is caused by the seismic model which shows insufficient for the depths where the second group of aftershocks is located.

9.1 Inconsistency of solutions

The inconsistency of the presented results, i.e. discrepant amplitude and polarity data, is quite disappointing. Taking the polarity information for granted, we hoped that solutions based on the ASPO method would fit not only the check-points but even the minima of the error function E.

The error function E is ruled by the complete seismic model and normalization. Projection of the check-points onto the focal sphere depends solely on the kinematics of the model. Therefore, credibility of polarity solutions is relatively high, supported also by a very good polarity coverage of the focal sphere. If there is any disagreement with solutions suggested by the minima of E, we conclude that the model should be refined rather than polarity readings are mistaken.

Unfavourable behaviour of some depth plots of $P(\phi_P, \delta_P, \lambda_P)$ follows from such incoherence. The searched range of depths was inspired by the location

depth of each aftershock, still some plots feature a couple of minima or none at all. We hope that splitting the third layer of the model by a new discontinuity and modifying the parameters properly might remove problems with depth determination and enable achievement of better results for the second group of aftershocks.

The error function E also suffers if information about the station is disputed. We drive at possible inaccurate orientation of the seismograph, real transfer function deviating from the one assumed in our computations, or unmodelled site-effects. Due to summation over stations, resolution and sharpness of E decrease (improved normalization) and false minima appear (former normalization). Consequently, solutions violating some of the requirements (see page 31) can only be found.

As regards seismic moment retrieval, resultant estimates are approximately two orders too low. We believe that the problem rests in instrumental parameters provided to us by the producer. The failure is however not critical since the main objectives are fault plane solutions and not absolute values of moment.

9.2 Comments on normalization

The improved normalization yields acceptable solutions more often. Results like 2601730 AX (the first station set) speak for the improved method, yet there is no implication that the former normalization is always worse (see surprising solutions of aftershock 2780500).

The former normalization takes relations among the engaged stations into account, which is after all a deprecated feature. The behaviour of the error function E is hard to tell, contributions of individual stations to it cannot be computed separately.

The improved normalization disregards the distribution of amplitudes, enabling faster re-computation of the whole inversion for station subsets among other things. Selective summation of error contributions may increase resolution of the error function E, offending stations can easily be identified in this process.

The fit of observed and synthetic spectra is always better for the improved normalization, which is a straightforward consequence of the acquired independence of records.

9.3 Conclusion

Results of a very formal approach to the ASPO method were reported in this part of the thesis. Criteria for solution determination were specified and the most satisfactory results presented.

In practice, solutions violating the pre-set requirements are rarely published. Yet, our study aimed to demonstrate the behaviour of the method and to improve it rather than discuss details of individual solutions.

With respect to factors affecting the error function E, inversion carried out from many stations and frequencies becomes overdetermined, which may prevent satisfaction of all requirements at the same time if the data and the model include some errors. In previous applications [1, 2, 3] of the method, such situation never happened thanks to much weaker constraints.

The testing revealed possible insufficiency of the used seismic model, still it was not feasible to alter models within this work.

Improvement of normalization of spectra was proposed and validated.

Acknowledgments

The author is grateful to the University of Patras (Prof. G-A. Tselentis, Director of the Seismological Laboratory) for kindly providing their unpublished data: the seismograms, arrival times, polarity readings and locations. Thanks go also to Anna Serpetsidaki for her focal mechanism solutions and technical help. Paris Paraskevopoulos assisted with format conversions.

Dr. Jaromír Janský of the Department of Geophysics, Charles University, generously provided his code for grid search location and ray computation so that I could extend it with velocity optimization and time corrections.

I express sincere thanks to Doc. Jiří Zahradník for his invaluable advice and encouragement. He kindly put his implementation of the ASPO method at my disposal and was open to discussion.

The work has been performed within the framework of the NATO grant EST.CLG.976035, and several projects in the Czech Republic: MSMT J13/98-113200004, ME354, and GACR 205/00/0902.

Bibliography

[1] Zahradník J. (2001): Focal Mechanism of the Athens 1999 Earthquake by ASPO Method. Tectonophysics (submitted)

[2] Zahradník J., Janský J., Papatsimpa K. (2000): Focal Mechanisms of Weak Earthquakes from Amplitude Spectra and Polarities. Pure and Appl. Geophys. (in press)

[3] Kalianko P. (1999): Matlab Package MTOOL for Earthquake Focal Mechanisms. Master Thesis, Charles University, Prague

[4] Tselentis G-A., Zahradník J. (2000): The Athens Earthquake of 7 September 1999. Bull. Seism. Soc. Am. 90, 1143–1160

[5] Tselentis G-A., Zahradník J. (2000): Aftershock Monitoring of the Athens Earthquake of 7 September 1999. Seism. Res. Lett. 71, 330–337

[6] Sokos E., Martakis N., Tselentis G-A. (2000): Stress Tensor Inversion for Attiki-Central Greece, Using the Athens 7 September 1999 Aftershock Sequence. Annales Geologiques des Pays Helleniques 38, ser. 1, fasc. B, 63–72

[7] Papadopoulos G. A., Drakatos G., Papanastassiou D., Kalogeras I., Stavrakakis G. (2000): Preliminary Results about the Catastrophic Earthquake of 7 September 1999 in Athens, Greece. Seism. Res. Lett. 71, 318––329

[8] Voulgaris N., Kassaras I., Papadimitriou P., Delibasis N. (2000): Preliminary Results of the Athens September 7, 1999 Aftershock Sequence. Annales Geologiques des Pays Helleniques 38, ser. 1, fasc. B, 51–62

[9] Bouchon M. (1981): A Simple Method to Calculate Green's Functions for Elastic Layered Media. Bull. Seism. Soc. Am. 71, 959–971

[10] Coutant O. (1989): Program of Numerical Simulation AXITRA. Res. Report LGIT, Grenoble (in French)

[11] Bouchon M., Aki K. (1977): Discrete Wave-Number Representation of Seismic-Source Wave Fields. Bull. Seism. Soc. Am. 67, 259–277